CORK INSTITUTE OF TECHNOLOGY

COLD ATOM PHYSICS: TRAPPING METHODS AND DETECTION SCHEMES

A THESIS SUBMITTED FOR THE DEGREE OF MASTER OF SCIENCE

Presented by

Thejesh N. Bandi

Supervised by

Dr. Síle Nic Chormaic

SUBMITTED TO CORK INSTITUTE OF TECHNOLOGY, CORK, SEPTEMBER 2008.

Abstract

Thesis title: Cold atom physics: trapping methods and detection schemes.

Author: Thejesh N. Bandi

The work presented in this thesis is concerned with the manipulation of laser-cooled rubidium atoms and the detection of small numbers of cold atoms using very sensitive light detectors. Laser-cooled atoms are atoms that have been slowed to very low velocities, corresponding to temperatures of the order of 100 μK, and they can be trapped in magnetic and/or optical traps. The advantage of using cold atoms for experiments in atomic and quantum physics stems from the fact that these atoms are effectively confined within a region of space and this provides longer interaction and observation times compared to atoms at room temperature. Hence, it is possible to explore and observe a number of effects that would otherwise be extremely challenging. The achievement of laser cooling and trapping of neutral atoms was a major breakthrough in the mid 80's and has resulted in significant advances being made in modern spectroscopy, the realisation of Bose-Einstein condensation, atomic clocks, and quantum information technologies amongst others.

In particular, the work focuses on two theoretical proposals for developing micro-traps for cold rubidium atoms involving (i) ultrathin optical fibres and (ii) wavelength sized apertures in thin films. In addition, a number of experimental techniques are explored with emphasis on the detection of small numbers of atoms near ultrathin optical fibres using both avalanche photodiodes and single photon detectors. A study

on the interactions between atoms and photons is crucial for a full understanding of quantum mechanical processes at the few atom scale and detection schemes sensitive to very low levels of fluorescence from the laser-cooled atoms are vital for attaining this goal. Finally, an experimental study on the design and fabrication of arrays of silica microdisks, that could be used for facilitating interactions between cold atoms and photons, is presented.

To my beloved parents, Girija and Nagabhushan

Mother is my strength;

Father is my motivation.

Contents

List of Tables

List of Figures

Acknowledgements

Firstly, I would like to thank Dr. Síle Nic Chormaic, my supervisor, for many suggestions and constant support during this research, without which this work wouldn't have been a possibility.

I like to thank Prof. Vladimir Minogin, who helped me in the theoretical work involved in trapping of cold atoms, the valuable discussions on trapping cold atoms proved to be very useful with which we could also put up a paper, which is published in Phys. Rev. A and a post deadline paper in CLEO, 2008 held at San Jose, California, U.S. I believe, these are the good starting experiences towards my research career. I like to take this opportunity to thank Prof. Paul Townsend, Head of Photonics centre, and his student Iris Choi for the loan of EG&G perkin elmer single photon detector. I thank Dr. Alan Morrison, University College Cork, for the loan of Tyndall fabricated APD. I like to extend my sincere thanks to Dr. Liam McDonnell, Head of the Department, Dept. of Physics and Instrumentation, Cork Institute of Technology. It was his support and encouragement that made things clear and beautiful during my studies in Ireland.

I like to thank my friends, Jayanta Mukherjee (J) for the help with Matlab, Cleitus Antony (Cleit) for his valuable discussions, which helped me a lot to learn in Physics and also few ideas of life, I also would like to thank David Goulding for the technique of free-space fibre coupling of light into the Single mode fibre.

It is my group-mates' constant support, help and friendly nature that made things easy during my research in Ireland. I thank Michael Morrissey(Mike), Kieran Deasy (DC), Jonathan Ward (Jon), Danny O'Shea (Dan), Yuqiang Wu, and Danny Gleeson, in this regard.

I would like to thank the National Access Programme team of Tyndall National institute for the support and encouragement towards the fabrication of microdisks, which is a good part of my thesis in the last chapter. I thank Vince Lodge for the

Scanning Electron Microscope (SEM) images of these microdisks.

Of course, I am grateful to my parents, my sister, Ash and my uncles, Sadananda, and Siddesh for their patience and *love*. Without them this work would never have come into existence.

Finally, I wish to thank the following: Dr. Arun Kumar, UCC for his friendship, suggestions and support through the thick and thin of my life in Cork. I also would like to thank Mrs. Yamuna Arun (Yamu) for her lovely Indian cuisines, which made me feel homely in Cork. I like to thank Dr. N. J. Harendra (for his friendship); Dr. Jog raj Jaiswal (for his useful suggestions).

List of Publications and Presentations

[1] Thejesh. N. Bandi, Vladimir G. Minogin, and Síle Nic Chormaic, "Atom microtraps based on near-field Fresnel diffraction", Phys. Rev. A, **78**, 013410 (2008) (*see appendix C*).

[2] Thejesh N. Bandi, Vladimir G. Minogin, and Síle Nic Chormaic, "Near-field atom microtraps based on Fresnel diffraction", postdeadline QPDA4 CLEO /QELS 2008, San José, USA, May 2008.

[3] Thejesh N. Bandi, and Síle Nic Chormaic, "Single colour trap using tapered-optical fibres", *under preparation.*

[4] S. Nic Chormaic, T. N. Bandi, V. G. Minogin, "Near-field diffraction optical microtraps for atoms", ICAP 2008, Storrs, CT, USA (July 2008).

[5] T. N. Bandi, V. Minogin and S. Nic Chormaic, "Novel trapping geometries for cold atoms", poster presented at IoP Ireland Spring Weekend, Carrickmacross, March 2008. **3^{rd} prize in student poster competition**.

[6] T. N. Bandi, M. Morrissey, K. Deasy, J. Ward and S. Nic Chormaic, "Numerical observations on atom interaction with the evanescent field of a tapered optical fibre", poster presented at QuAMP, London, UK September 2007.

[7] T. N. Bandi, K. Deasy, M. Morrissey and S. Nic Chormaic, "Single atoms and single photons: probing the quantum world", poster presented at All-Island Conference on Quantum Information Science and Technology, NUI Maynooth April 2007.

[8] T. N. Bandi, K. Deasy, M. Morrissey and S. Nic Chormaic, "Single atoms and single photons: probing the quantum world", poster presented at Institute of Physics Spring Weekend, Birr March 2007. **Commendation for visual impact prize in student poster competition**.

[9] T. N. Bandi , K. Deasy, M. Morrissey, B. Shortt, D. O'Shea, J. Ward and S. Nic Chormaic, "Atom trapping and guiding using fibre taper technology", poster presented at Les Houches Summer School on "Laser Cooling and Bose Einstein Condensation", France September 2006.

Glossary of Acronyms

BEC	Bose-Einstein Condensate
QED	Quantum Electrodynamics
SMF	Single Mode Fibre
APD	Avalanche Photo Diode
WGM	Whispering Gallery Mode
MOT	Magneto-Optical Trap
ZARPT	Zeeman Assisted Radiation Pressure Trap
SPD	Single Photon Detector
OSA	Optical Spectrum Analyser
UHV	Ultra High Vacuum
AOM	Acousto Optical Modulator
NDF	Neutral Density Filter
FWHM	Full-Width Half Maximum
Opamp	Operational Amplifier
PCDM	Photon Counting Detector Module

SPCM	Single Photon Counting Module
LED	Light Emitting Diode
GRIN	Graded Index
NAP	National Access Programme
UH-Q	Ultra-high-Q
OMR	Optical Micro-ring Resonator
HF	Hydro Fluoride
SEM	Scanning Electron Microscope

Introduction

The achievement of laser cooling and trapping of neutral atoms has enabled significant progress in modern spectroscopy, including the realisation of Bose-Einstein condensates (BEC) [1], atom interferometry [2], atomic clocks [3], atom lithography [4] and quantum information technologies [5]. The manipulation of cold, neutral atoms [6] plays an important role in the development of atom optics experiments [7]. Therefore, methods to trap cold atomic ensembles is a significantly important task. Techniques adapted from microtechnology can be used to manipulate cold atomic samples [8]. A microfabricated atomic chip is one example of such an implementation. Cavity quantum electrodynamics (QED) experiments have also become feasible through the use of microfabricated elements and quantum information processing should be possible through the experiments of cavity QED [9]. Hence, the study of interactions between single atoms and single photons has become a reality.

The development of very sensitive detectors [10] is also crucial for the advancement of quantum technologies based on atom plus photon interactions. Solid-state single photon detectors are the backbone for experiments involving the detection of single photons.

The work presented in this thesis is concerned with the manipulation of cold atomic samples. It mainly deals with trapping mechanisms using detuned laser radiation and, also, the detection schemes for low light levels when an atom interacts with the light field.

Chapter 1 consists of an introduction to the history of laser cooling. Cold atoms generally means the range of temperatures one million times colder than that of

room temperature, ~ 100 μK. In this chapter the principle behind laser cooling and magneto-optical trapping of alkali atoms will be briefly described.

Chapter 2 is a theoretical discussion about how to trap cold atoms using a tapered optical fibre. A tapered optical fibre is a modified single mode fibre. When light is coupled into one end of the fibre, there is a significant amount of the field, which propagates outside the fibre boundary at the tapered waist. This field is rapidly decaying and is called the *evanescent field*. Typically, the tapered diameter is in the submicron range. Atom + photon interactions can be studied by placing a tapered optical fibre into a trapped sample of atoms. Any cold atoms close to the surface of the optical fibre will experience a van der Waals force and this is also considered in the theory.

Chapter 3 presents a novel technique for trapping cold atoms by a diffracted light field. The diffracted field considered is formed by near-field Fresnel diffraction at circular apertures. The apertures are of a size exceeding the optical wavelength. The field distribution in the vicinity of an aperture in a thin screen is analysed and the appropriate trapping parameters for rubidium and caesium atoms are discussed.

In Chapter 4 some experimental details are provided. A technique for coupling light into single mode fibres (SMF) is discussed. The chapter also deals with the use of avalanche photo detectors (APD). An APD fabricated in Tyndall National Institute is characterised and analysed for its use. A Geiger mode condition, in which these APDs can act as single photon detectors, is also discussed in brief. Other single photon detectors are also characterised to test their feasibility for the detection of light emissions from cold atoms.

The final chapter in this thesis, Chapter 5, concentrates on techniques for fabricating whispering gallery mode (WGM) microcavities. This chapter is based on work carried out within the Tyndall National Institute's National Access Programme (NAP112). Fabrication process flow for the microcavities is discussed in detail. A comparison between dry- and wet-etching techniques is also presented. A possible experiment to measure the Q-factor of these disks is proposed. Finally, a conclusion

to the work presented within this thesis is provided.

Chapter 1

The Magneto-Optical Trap

1.1 Introduction

It has been more than 20 years since the first magneto-optical trap (MOT), combining laser cooling and magnetic trapping of atoms, was demonstrated. The achievement of laser cooling and trapping enabled significant progresses in modern spectroscopy [11], time and frequency standards [12], the realisation of Bose-Einstein Condensation (BEC) [1].

A brief history of atom manipulation using light forces, which led to the awarding of two Nobel Physics prizes to six individuals in the field of laser cooling and Bose-Einstein condensation, follows. In 1975, the first proposal to cool neutral atoms was presented by Hänsch and Schawlow [13]. In 1976, a demonstration of atom manipulation using light forces was made [14]. Later, in 1985, Phillips *et al.* showed that atoms can be trapped in a magnetic trap [15]. In the same year, Chu *et al.* trapped atoms in a focussed laser beam [16], as proposed by Ashkin [17]. Subsequently, Raab *et al.* [18] developed the magneto-optical trap (MOT) for sodium atoms. In 1988, sub-Doppler cooling was observed by Lett *et al.* [19] and explained by Dalibard and

Cohen-Tannoudji [20]. It took several more years until Bose-Einstein Condensation (BEC) was demonstrated in an alkali gas of rubidium by Anderson *et al.* [1] Davis *et al.* [21] in sodium atoms, and Bradley *et al.* [22] in lithium. In 1997 the Nobel prize in Physics was awarded to S. Chu, W. D. Phillips and C. Cohen-Tannoudji for the development of laser cooling techniques and the 2001 Nobel prize in Physics was awarded to E. Cornell, C. Wieman and W. Ketterle for their use of laser cooling to achieve BEC in dilute atomic gases.

For an introduction to the principles behind laser cooling and trapping the reader is referred to [23]. In this chapter, some of the principles behind the MOT are briefly discussed.

1.2 Laser Cooling

The acceleration undergone by an atom irradiated by a laser can be calculated in the following way. Each time a photon of wavelength λ_L is absorbed by an atom, due to momentum conservation, the atomic velocity changes by the recoil velocity, v_{rec},

$$v_{rec} = \frac{\hbar k_L}{M}, \tag{1.2.1}$$

where $k_L = 2\pi/\lambda_L$ and M is the mass of the atom. Typically, for alkali atoms, v_{rec} varies between 3 and 30 mms^{-1}. The acceleration experienced by an atom irradiated by light is determined from $a = \Gamma v_{rec}$. Since the scattering rate for photons is approximately the inverse of the excited state lifetime, $\Gamma^{-1} \approx 30$ ns, it follows that, typically, for alkali atoms, $a = 10^5$ $\text{ms}^{-2} = 10^4$ g. This force exerted by light on an atom is four orders of magnitude larger than the gravitational force.

In principle, atoms are in continuous motion, and therefore the moving atoms do

not see the laser beam at the same frequency as in the laboratory frame of reference. Doppler cooling was first suggested in 1975 by Hänsch and Schawlow [13]. It is based on the fact that the laser frequency is shifted for a moving atom by $-k.v$, with a negative detuning (i.e., the laser frequency is detuned less than the resonance frequency between the ground and excited states) $\delta = \omega_L - \omega_O < 0$. The radiation pressure is stronger for atoms with a velocity opposite to the laser wave vector i.e., $k.v < 0$, so that the momentum transfer $\hbar k$ is opposite to its velocity $\mathbf{v}$ and slows down the atom. For further details on the processes involved in laser cooling the reader should refer to [23].

The radiation pressure force for a plane wave has the expression

$$\mathbf{F}_{pr} = \frac{\Gamma}{2}\frac{S}{1+S}\hbar\mathbf{k}_L \tag{1.2.2}$$

where Γ is the excited state life-time of the atom, S is the saturation parameter and $\mathbf{k}_L$ is the momentum of the laser-wave. We can define a saturation parameter, S, given by:

$$S = \frac{\Omega^2/2}{\delta^2 + \frac{\Gamma^2}{4}} \tag{1.2.3}$$

where Ω is the Rabi frequency, If the two counter-propogating laser waves incident on an atom have the same intensity and the same frequency, and are slightly detuned to the red of the atomic transition frequency ($\omega_L < \omega_A$), then the two forces on the atom at rest exactly balance each other and the net force is equal to zero. For a moving atom, the apparent frequencies of the two laser waves are Doppler shifted. The counter-propagating wave becomes closer to the atomic resonance, thereby exerting a stronger radiation pressure than the co-propagating wave, which goes farther from the resonance. Fluctuations of the force give rise to a diffusion in momentum space

and to heating. The two processes in competition -*cooling and heating*- leads to a Doppler limit temperature.

It can be shown that the temperature reached by laser cooling for two-level atoms is determined by Γ. The exact value of the minimum temperature which can be reached is given by $k_B T_D \sim \hbar\Gamma/2$ [24], where k_B is the Boltzmann constant, and T_D is called the 'Doppler limit temperature'. T_D is on the order of 140 μK for rubidium (Rb), 125 μK for Caesium (Cs), and 240 μK for sodium (Na). The corresponding velocity can be calculated as, $\bar{v}=\sqrt{k_B T_D/M}= \sqrt{\hbar\Gamma/2M}$. For Rb, it is 12 cms^{-1}. In fact, when the measurements became precise enough, it was seen that the temperature in optical molasses was much lower than predicted. This indicates that other laser cooling mechanisms, more powerful than Doppler cooling, are operating. In fact, there exist cooling mechanisms resulting from an interplay between spin and external degrees of freedom, and between dispersive and dissipative effects, called "Sisyphus cooling" or "polarization gradient cooling" [20].

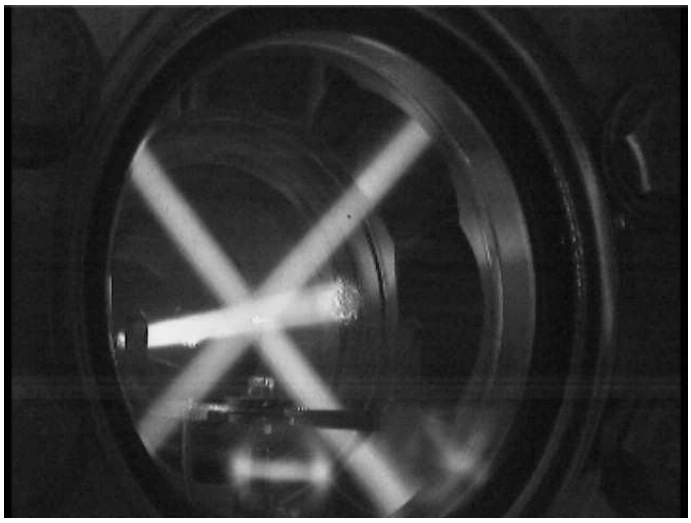

Figure 1.1: Fluorescence of counter-propagating beams. MOT at Quantum Optics Group, Cork.

Optical molasses was first observed by Chu *et al.* [16] The reason why the name *optical molasses* was coined, in the words of Chu himself (as he said in his Nobel lecture): "The name optical molasses takes on a more profound meaning with this new form of cooling. Originally, I conceived of the name thinking of a viscous fluid associated with cold temperatures: 'slow molasses in January'. With this new understanding, we now know that cooling in optical molasses has two parts: at high speeds, the atom feels a viscous drag force, but at lower speeds where the Doppler shift becomes negligible, the optical pumping effect takes over. An atom sees itself walking in a swamp of molasses, with each planted foot sinking down into a lower energy state. The next step requires energy to lift the other foot up and out of the swamp, and with each sinking step, energy is drained from the atom".

Note that cooling the atoms does not restrict them to a region of space, a magnetic field must be applied to provide the trapping potential. The details of this technique are briefly explained in the following section.

1.3 Magneto-Optical Trap (MOT)

Doppler cooling enables a quick cooling of the atoms. However, the atoms are not trapped and may leave the laser beams and be lost. Therefore, in order to trap the atoms in space, a magnetic field is incorporated into the system by the addition of two Helmholtz coils in anti-Helmholtz configuration i.e., the current in the two coils circulate in the opposite directions to each other. This provides a zero magnetic field region where the cooling laser beams intersect each other. In a one dimensional configuration, as first suggested by Aspect et al. [25], the two counter-propagating light waves, which are detuned to red ($\omega_L < \omega_A$) and which have opposite circular

polarizations, are in resonance with the atom at different places. This results in a restoring force towards the point where the magnetic field vanishes. Furthermore, the non zero value of the detuning provides Doppler cooling. In fact, such a scheme can be extended to three dimensions and leads to a robust, large and deep trap called the "magneto-optical trap" [18].

1.4 Conclusion

The 3-D MOT, along with optical molasses, has become an important tool in neutral atom laser cooling. The trap can collect slow atoms from a thermal distribution of a vapour cell [26], and is able to concentrate the atoms so much that collisions and radiation pressure exerted by the atoms' fluorescence are factors limiting the achievable density [27]. In 2-D the MOT has been used as an 'atomic funnel' to concentrate sodium atoms both with near zero longitudinal velocity [28] and in an atomic beam with 50 ms^{-1} longitudinal velocity [29]. Typically, the number of atoms in a cold cloud of alkali atoms is $\sim 10^7$, with cloud dimensions of the order of mm^3.

Chapter 2

Trapping of cold atoms using tapered optical fibres - Theory

2.1 Introduction

The manipulation of cold, neutral atoms plays an important role in the development of atom optics experiments. Current-carrying wires [30] and hollow-core optical fibres [31] are viewed as some of the simplest configurations that can be used for atom trapping and guiding. There are also proposals to trap and guide atoms *outside* an optical fibre. This technique relies on the presence of an evanescent field that extends beyond the surface of an optical fibre and is optimised for subwavelength-diameter fibres [32, 33]. In this chapter, the theoretical aspects of trapping cold atoms around a tapered optical fibre will be discussed.

The majority of experimental research involving laser-cooled atomic samples deals with either caesium or rubidium isotopes, due to the ease with which appropriate lasers for the cooling transitions can be obtained. With the advent of laser cooling techniques [16], it has become possible to routinely produce cold atomic samples

in the research laboratory. The aim of our research is to study the interaction of laser cooled atoms with the evanescent field outside an optical fibre. The following theoretical estimations are based on ^{133}Cs and ^{85}Rb samples.

2.2 Evanescent Field outside a Tapered Fibre

Tapered optical fibres can be produced by heating and pulling single-mode optical fibre to a very fine waist [34], ensuring that the adiabatic criteria for lossless transmission is obeyed [35]. By decreasing the fibre waist diameter, d, to the submicron range, the taper transition transforms the local fundamental mode from a core mode in the non-tapered region to a cladding mode in the tapered region, leading to guided modes with a significant evanescent field outside the tapered area of the fibre [36]. The evanescent field decays exponentially with distance from the fibre. There are many applications of evanescent waves for laser-cooled atoms , including atom mirrors [37–39], traps and guides [40]. Review articles can be found in [41, 42].

The trapping potential shape for an atom is defined by the rigid surfaces *e.g.* prisms or fibres, around which the evanescent field is formed. Guiding of atoms inside the core of hollow optical fibres has previously been demonstrated [43–45]. However, the method of guiding atoms inside a fibre increases the kinetic energy of the atoms by collisions, thereby increasing the temperature of the cold atoms. The proposal to trap cold atoms outside the tapered part of an optical fibre [32, 33] removes this limitation.

The evanescent decay length, Λ, is dependent on the fibre tapering and can be calculated using an approximated formula of the fibre eigen-value equation [46].

$$\Lambda = \left[k^2\eta_f^2 - 2.405/a^2\right]^{-1/2}, \tag{2.2.1}$$

where k is the wave vector given by $k = 2\pi/\lambda$, λ is the wavelength of the input laser light, a is the radius of the fibre taper and η_f is the refractive index of the core of the fibre. An important thing to note here is that, in a tapered fibre, the cladding itself behaves as core and the outer atmosphere(air or vacuum) behaves as the cladding for an evanescent wave. Hence, one take η_f as the refractive index of the cladding. One

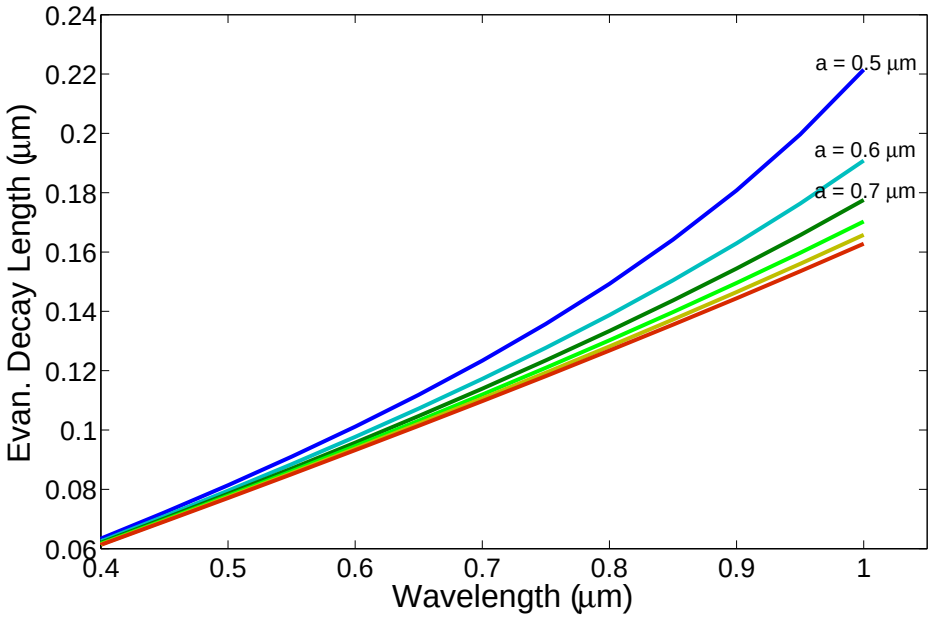

Figure 2.1: Penetration length, Λ, of the evanescent wave against the wavelength, λ, of the light field for various values of the fibre radius, a. The refractive index of silica is $\eta_f = 1.45$ and that of air is $\eta_0 = 1$.

can approximate the decay length of the evanescent wave as [47]

$$\Lambda = \frac{\lambda}{2\pi}. \tag{2.2.2}$$

In Fig. 2.1 the decay length is plotted as a function of wavelength for different tapered radii. If one considers the light propagating through the fibre to be *on resonance* with

the rubidium cooling D2-transition, $5S_{1/2}F = 3 \leftrightarrow 5P_{3/2}F^{'} = 4$, then, $\lambda \simeq 780$ nm. For a taper radius of $a = 0.5$ μm one can see from Fig. 2.1, that the evanescent wave will extend ≈ 0.15 μm beyond the fibre surface.

2.3 Atom in an Optical Field

A fibre-based method for microscopic trapping and guiding of individual atoms has already been proposed [32, 33]. The advantages of the scheme are the following: (i) localization of atoms to a subwavelength region, (ii) high efficiency to detect individual atoms, (iii) high accessibility to the trapped atoms, and (iv) achievement of strong coupling between light and matter. In order to have control over the fibre trap and also to be able to manipulate an atom in the evanescent field one should know the optical response of an atom in a near-resonant field. When an atom interacts with near-resonant light, one must consider both absorption and scattering. The cross-section is an important parameter which determines the amount of interaction between the atom and the light field.

By considering a two-level atom, the cross-section, σ, depends only on the transition frequency between the two levels such that

$$\sigma = \frac{3\lambda_0^2}{2\pi}, \tag{2.3.1}$$

where λ_0 is the wavelength corresponding to the energy separation between the two levels. A strong transverse confinement of the field in a waveguide enables the scattered photons from an atom to couple to the guided modes of the fibre [48]. An experimental investigation into the fluorescence photons from a cloud of cold atoms coupled into the guided modes of a tapered fibre has recently been demonstrated [49]

and a theoretical investigation of the correlations of the photons emitted into the nanofibre by atoms has been done [50]. The strong confinement of the guided modes of the fibre enable the scattered photons from atoms to couple efficiently into the fibre.

An earlier theory [51], neglected the geometric specifications of the waveguide and, thereby, the strong confinement of the guided modes. The thin thickness of a nanofibre and the difference between the refractive indices of the silica core and the vacuum clad can substantially modify the polarisation properties and intensity distribution characteristics of the field [50]. Modification of the spontaneous emission of the atom due to the presence of the waveguide was also not considered. Such a modification could arise due to short-range forces between the atoms and the fibre surface [52]. Furthermore, the multilevel structure of a real atom modifies the absorption and scattering characteristics [53]. All these factors must be included in a systematic treatment for the interaction of an atom with a near-resonant light field in the close vicinity of a nanofibre.

The question to be addressed is, can one measure the photons which are coupled to the guided modes of the fibre? To have a reasonable estimate of the cycle-averaged Poynting vector of the light propagation is considered, which is given by

$$\mathbf{S} = \frac{1}{2} Re(\mathbf{E} \times \mathbf{H}), \tag{2.3.2}$$

where $\mathbf{E}$ is the electric field and $\mathbf{H}$ is the envelope of the magnetic component of the field. In cylindrical coordinates, the longitudinal, tangential, and radial components of the vector, $\mathbf{S}$, can be written as $\mathbf{S}_z$, $\mathbf{S}_\phi$, and $\mathbf{S}_r$, respectively. For guided modes of fibres, the radial component, $\mathbf{S}_r = 0$, since the light field is confined in the fundamental mode of the fibre. Note that a very small input power into the fibre can produce

a substantial intensity at the tapering because of the reduction in surface area [54].

The saturation intensity, I_S, [55] can be calculated as

$$I_S = \frac{2\pi^2 \hbar c \gamma_0}{3\lambda_0^3}, \tag{2.3.3}$$

where $\hbar = h/2\pi$, γ_0 is the upper-level population decay rate of the atom, and λ_0 is the resonant transition wavelength. For ^{85}Rb, $\gamma_0 = 5.98$ MHz and by considering the D2 transition, one gets that, $I_S = 1.6$ mW/cm^2. The saturation intensity is, therefore, comparable to the intensity of the field around the fibre even when a very low power of the order of pW [54] is coupled into the fibre as a probe beam.

The propagation power, P_z, along the transverse plane of the fibre is determined as the integral of S_z, the longitudinal component of the Poynting vector, such that [56]

$$P_z = \int_0^{2\pi} d\varphi \int_0^{\infty} r S_z dr. \tag{2.3.4}$$

The flux of photons along, z-axis, n_z, is given by

$$n_z = \frac{P_z}{\hbar\omega}, \tag{2.3.5}$$

where $\hbar\omega = \mathbf{E}_z$ is the energy of photons in, z-direction.

Since the evanescent field, $\mathbf{E}$, around the fibre has a substantial longitudinal component, $\mathbf{E}_z$, the quantities P_z and n_z do not represent the total amount of energy and the number of photons incident into the atom per unit time. Instead, these quantities characterize only a part but not the whole field acting on the atom. However, the propagation power, P_z, is conserved along an adiabatically tapered fibre provided the loss of the field is negligible. Therefore, P_z can be measured experimentally at the end of such a fibre. To measure such a low light level of pW or less one needs to adopt a very sensitive detection scheme. In our experiments, we use avalanche photo

detectors (APDs) and, for signals lower than pW of power, we use APDs in Geiger mode. These act as single photon detectors (SPDs) and are discussed in detail in Chapter 4 .

As a quantitative analysis, we calculate the number of photons available for detection by taking an example. In other words, let us examine the number of atoms responsible for the photon signal that is to be detected using a photon counter. At this point we will get an idea of the important detection parameters for the future experiments. Let us assume that the light coupled into the fibre is on-resonance with the atomic cooling transition i.e. ($5^2S_{1/2}(F=3) \longrightarrow 5^2P_{3/2}(F=4)$ transition), with wavelength $\lambda = 780$ nm. For this transition, the natural linewidth is $2\gamma = 2\pi \times 5.98$ MHz and the saturation intensity is $I_S = 1.6$ mW/cm^2 [57]. When the cold atoms come near the evanescent field, the atoms absorb some of the resonant light and re-emit light at the same frequency. These scattered photons couples back into the fibre [48], and are subsequently detected.

Consider a cold atomic cloud of radius, $r = 1.5$ mm, with the number of atoms in the cloud given by, $N_{cloud} = 10^8$ atoms. The volume of the cloud, $V_{cloud} = 4.2 \times 10^{-9}$ m^3 is calculated by,

$$V_{cloud} = \frac{4}{3}\pi r^3 \tag{2.3.6}$$

For a tapered optical fibre of radius, $a = 0.5$ μm, from Fig. 2.1 one can see that the evanescent decay length, $\Lambda = 0.15$ μm. The volume of the evanescent field, V_{evan} is calculated as,

$$V_{evan} = \pi l(R_1^2 - R_2^2) \tag{2.3.7}$$

where $l = 2$ mm is the length of tapering, $R_1 = 0.65$ μm is the distance from the center of the fibre to the 1/e value of the evanescent field, and $R_2 = 0.5$ μm is the

distance from the center of the fibre to the surface. By using the above values one gets, $V_{evan} = 1.1 \times 10^{-16}$ m^3.

When the tapered fibre is inside the cold cloud, the number of atoms interacting, N_{int}, in the small volume of the evanescent field at any instant of time can be calculated as,

$$N_{int} = N_{cloud} \frac{V_{evan}}{V_{cloud}} \tag{2.3.8}$$

By substituting the values for V_{evan}, V_{cloud} and N_{cloud}, we get, $N_{int} = 2.6$ atoms. Therefore, the signal is very weak and one needs a photon counter to detect the photons emitted by atoms and it will be essential to average the results in order to obtain better signal to noise ratios. On contrary, an averaging of few thousand cycles in the signal can give better results. Therefore, in order to obtain a reasonable signal it will be important to increase the density of the MOT and decrease the radius of the fibre. By controlling these two parameters, one can get a better signal for detection.

2.4 Influence of the van-der-Waals Potential

The van der Waals force is a natural, attractive force that arises when atoms approach a surface and its influence must also be considered, in addition to the optical potential. Initially, the calculations by Balykin *et al.* [33] were replotted to determine at what distance from the fibre surface the van der Waals force is influential. The van der Waals potential energy, V_j, associated with the fibre surface-atom interaction can be written as

$$V_j = -\frac{C_{3j}}{r^3}, \tag{2.4.1}$$

where C_3 is the van der Waals coefficient for the atomic species under investigation, r is the distance from the fibre surface, and $j = e$ or g represents the excited or ground

internal states of the atom.

For the case of ^{133}Cs atoms the ground and excited state refer to the D2 line ($6S_{1/2}F = 3 \leftrightarrow 6P_{3/2}F' = 4$). By considering a Cs-atom near a semi-infinite silica medium [58] the parameters for the ground and excited state are $C_{3g} = 1.56$ kHzμm, and $C_{3e} = 3.09$ kHzμm. A plot of the van der Waals potential for a Cs atom as a function of distance from the the fibre surface is shown in Fig.2.2.

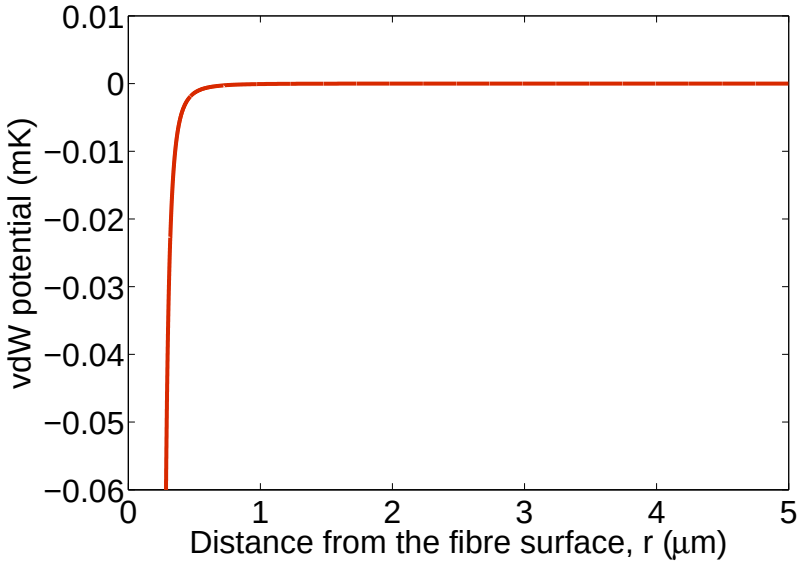

Figure 2.2: Plot of the van der Waals potential for a Cs atom as a function of the distance,r, from the fibre

2.5 Total Potentials for ^{133}Cs and ^{85}Rb Atoms

A schematic diagram of an atom moving around an optical fibre is shown in Fig. 2.3. The optical potential, U, of an atom is cylindrically symmetric around the fibre. This means that U depends on the radial distance r from the atom to the fibre axis z, but not on the two other cylindrical coordinates, ϕ and z. The component, L_z, of

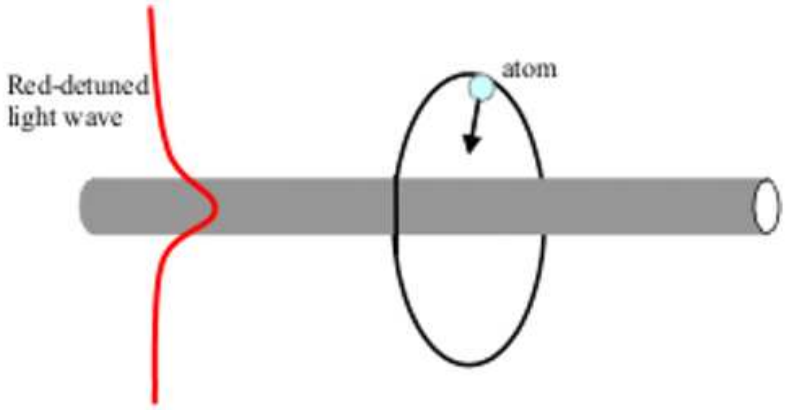

Figure 2.3: Schematic representation of an atom being trapped using a red-detuned light field propagating through an optical fibre.

angular momentum of the atom is conserved due to this symmetry. According to the eigenstate problem, [33], one can consider $L_z = \hbar m$, where m is an integer, called the rotational quantum number. The centrifugal potential, U_{cf} of an atom is given by

$$U_{cf} = (\hbar)^2(m^2 - 1/4)/2Mr^2 \tag{2.5.1}$$

where $\hbar = h/2\pi$, M is the mass of the atom and r is the distance of an atom from the fibre surface. This term is repulsive due to the circular motion of the atom. The effective potential of an atom in its radial motion in one-dimension can be written as a combination of the centrifugal potential and the optical potential, i.e., $U_{eff} = U_{cf} + U$. If U_{eff} has a local minimum at a distance $r = r_m$ outside the fibre, there exist stable bound states for the atom. This may happen only if the optical potential, U, is attractive. In order to ensure this, the input light into the tapered fibre must be *red-detuned*, i.e., the input light is of less frequency compared to the cooling transition frequency. This generates an evanescent field around the tapered part of the fibre,

whose steep variation in the transverse plane leads to the gradient force on the atom.

The optical potential outside the fibre can be written as,

$$U = -GK_0^2(qr), \tag{2.5.2}$$

where K_0 represents the modified Bessel functions of the second kind, which depends on the distance from the fibre surface, r, and $q = 1/\Lambda$, where Λ is the evanescent decay length, determined by the fibre eigenvalue eqn. (2.2.1). G is the coupling constant, which gives the indication of coupling of atom with that of the evanescent field, given by

$$G = \frac{-\hbar\Omega^2}{\Delta K_0^2(qa)}, \tag{2.5.3}$$

where a is the radius of the tapered part of the fibre, Ω is the Rabi frequency, and Δ is the detuning of the laser with respect to the resonant transition of the atom. The

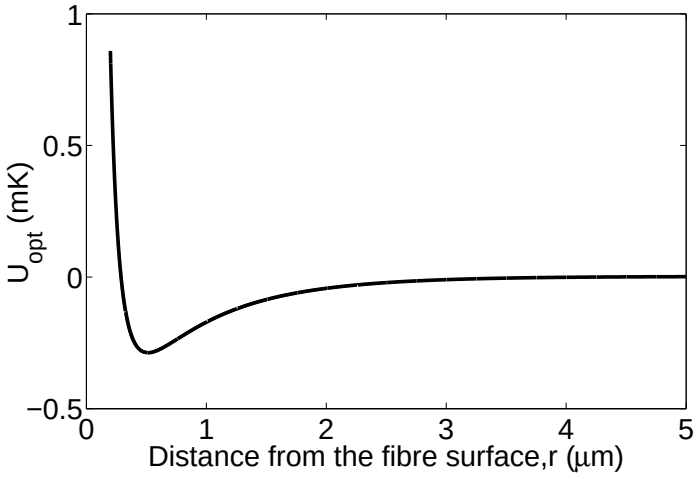

Figure 2.4: Effective potential for a ^{133}Cs atom outside the tapered fibre as a function of distance.

effective potential for the radial motion of an atom in the optical potential, U, can be given as,

$$U_{eff}(r) = \Theta_{rec}\left[\frac{m^2 - 1/4}{k^2 r^2} - gK_0^2(qr)\right], \tag{2.5.4}$$

where $\Theta_{rec} = (\hbar k)^2/2M$ is the recoil energy and $g = G/\Theta_{rec}$ is the normalized coupling parameter. Here $M = 2.2 \times 10^{-25}$kg is the mass of a ^{133}Cs atom and $k = 2\pi/\lambda$ is the wave number of the field. By considering the parameters $m = 230$, $\lambda = 1.3$ μm, $g = 5330$, $\Lambda = 2.42$ μm and $\Theta_{rec} = 888$ Hz [33] and substituting them into eqn. (2.5.4)the effective potential is obtained. A plot of the effective potential for the above parameters is shown in Fig. 2.4. The van der Waals potential is significant

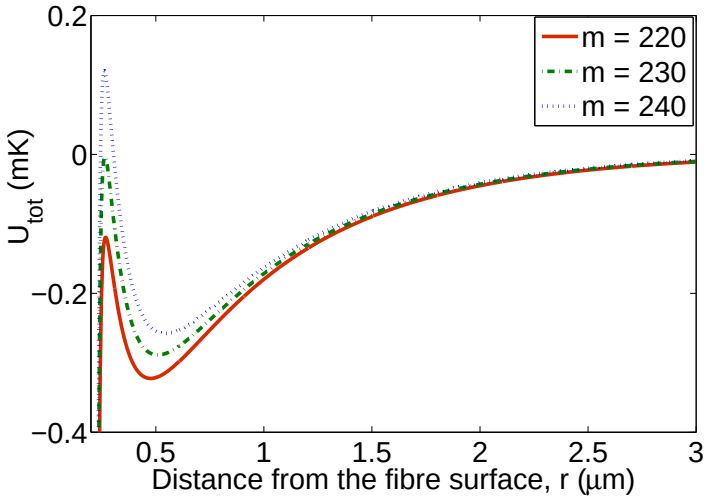

Figure 2.5: Total potential (centrifugal+optical+van der Waals) for ^{133}Cs atoms

when the atom is very close to the fibre surface. In order to see its influence on the total potential it is necessary to add the effective potential given in eqn. 2.5.4 and the van der Waals potential given in eqn. 2.2. The resulting total potential, U_{tot} is plotted in Fig. 2.5 as a function of the Cs atom distance from the fibre. Since the

surface roughness of the fibre itself could be of the order of nanometers, the van der Waals force has no appreciable effect on the free atoms in the vicinity of the optical potential. However, the atoms could adsorb on to the fibre surface and remain stuck to it by the van der Waals force. Since the overall trapping potential is in the micron range trapping of the atoms should be feasible if one finds a way to load the atoms adiabatically into the trapping potential well.

2.5.1 Energy levels in the trapping potentials for ^{133}Cs

It is now possible to reexamine the effective potential and to determine the energy levels within the potential for Cs atoms. In the following, we will consider the $m = 230$ level. The effective potential is given by eqn. (2.5.4). The distance from the fibre surface at which the minimum for the potential occurs, r_{min}, can be found by taking the derivative of eqn. 2.5.4 and by expanding it in the Taylor series to get

$$U_{tot} = U_0 + U_0' + \frac{U_0''}{2}(r - r_m)^2 + ... \tag{2.5.5}$$

The first two terms in the expansion refer to the original potential and the minimum of the potential, respectively. The third term in the expansion i.e., the second derivative of the effective potential, is, therefore, similar to the harmonic potential

$$V = \frac{1}{2}Kx^2, \tag{2.5.6}$$

where K is the spring constant and x is the distance from minimum of the potential. The ground state energy of the harmonic potential in eqn. 2.5.6 is given by,

$$E_n = (n + 1/2)\hbar\omega, \tag{2.5.7}$$

where n is an integer, and $\omega = \sqrt{\frac{K}{M}}$ is the angular frequency and M, the mass of a Cs atom. Comparing eqns. (2.5.5) and (2.5.6), we see that $K = \frac{U_0''}{2}$. With reference

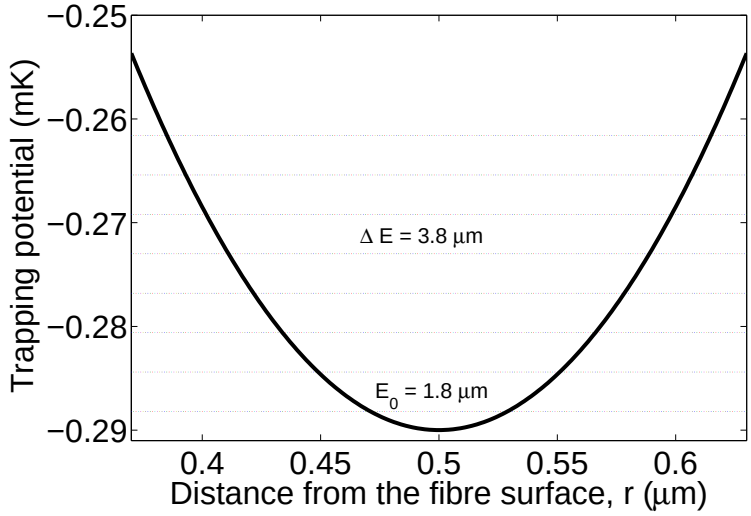

Figure 2.6: Energy levels in the effective potential for ^{133}Cs atoms with an orbital angular momentum of $m = 230$.

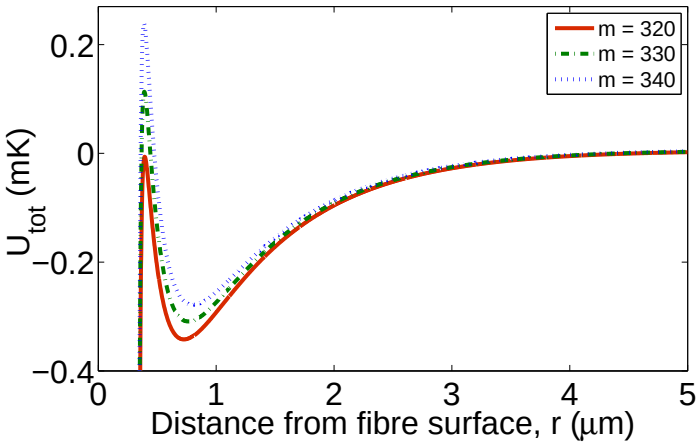

Figure 2.7: Total potential for ^{85}Rb atoms as a function of distance from fibre surface.

to Fig. 2.4 for the effective potential, and by substituting the values for eqn. (2.5.5), as, U = - $0.29 \times 10^{-3} + 7.6 \times 10^{-5} + \frac{4.3 \times 10^{-3}}{2}(r - 0.5)^2$, one can quantify the energy levels in the effective potential. Therefore, the ground state energy is $E_0 = 1.8$ μK, the first excited state is $E_1 = 5.6$ μK, the second excited level is $E_2 = 9.4$ μK and so on. The energy separation between two neighbouring levels is $\Delta E = 3.8$ μm, as shown in Fig. 2.6.

2.5.2 Energy levels in the trapping potentials for ^{85}Rb

The trapping potential and energy level estimation are also done for ^{85}Rb atoms. The same equations for the van der Waals potential (2.4.1) and effective potential (2.5.4) are also applicable for ^{85}Rb atoms. The calculations are performed assuming a fibre radius, $a = 0.3$ μm, input laser power, $P = 30$ mW, wavelength of the laser

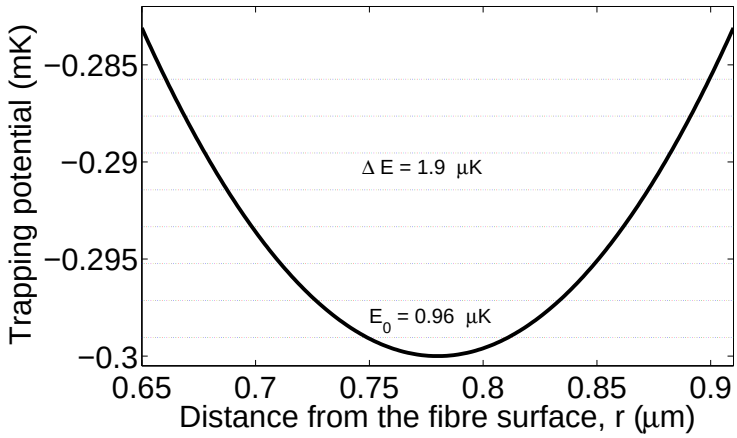

Figure 2.8: Energy levels in the total potential for ^{85}Rb atoms with an orbital angular momentum of $m = 330$.

$\lambda = 1.5$ μm, and the C_3 value for ^{85}Rb is calculated from [58, 59] as 3 kHz μm^3. The potential maximum is at $m = 310$ for the typical values above. A graph of total potential calculated from eqn. 2.5.4 for $m = 320$, 330 and 340 is shown in Fig. 2.7. To determine the optical potential $m = 330$ is considered. A trap depth of 0.3 mK is estimated. This is sufficient for trapping ^{85}Rb atoms with a temperature of 100 μK.

2.5.3 Trapping potentials for ^{133}Cs and ^{85}Rb for varying fibre parameters

By varying a number of experimentally accessible parameters such as the radius of the tapered fibre, the wavelength of the light coupled into the fibre and the input laser power, one can obtain trapping potentials for different orbital angular momenta, m. The minimum and maximum values of the orbital angular momentum for which a

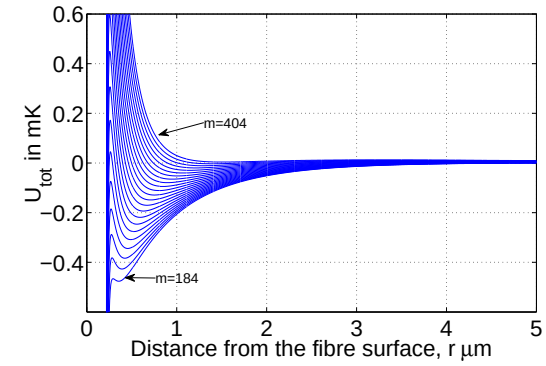

(a)

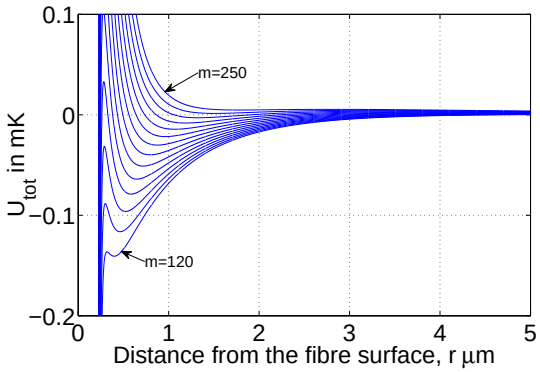

(b)

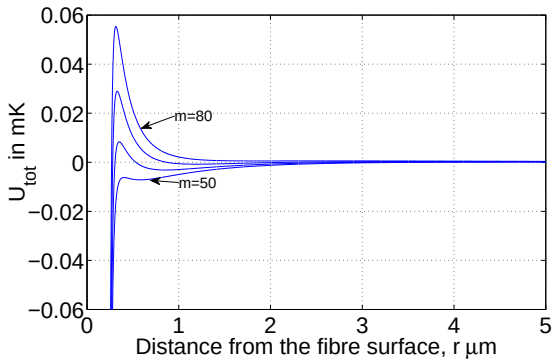

(c)

Figure 2.9: Total potential as a function of distance from the surface for a range of m values for ^{133}Cs, with $a = 0.2$ μm and $\lambda = 1.3$ μm. (a) for $P_L = 30$ mW, (b) for $P_L = 10$ mW, (c) for $P_L = 1$ mW.

Table 2.1: Caesium potential depths for varying input laser powers.

Fig. no.	$a[\mu m]$	P_L [mW]	λ_L [μm]	m_{min}	U_{min} [μK]	m_{max}	U_{max} [μK]
2.9(a)	0.2	30	1.3	184	10	404	6
2.9(b)	0.2	10	1.3	120	4.3	250	4.3
2.9(c)	0.2	1	1.3	50	1nK	80	3 pK

trapping potential exists are determined in the following section.

Caesium

Table 2.1 shows the minimum and maximum values of the orbital angular momentum for three different values of the input laser power, P_L= 1 mW, 10 mW and 30 mW, for which a trapping potential exists. The radius of the fibre, a, and the wavelength of the detuned laser, λ_L, are taken to be constant. The values of the corresponding trap depths are also determined by plotting the graph of effective potential (eqn. 2.5.4). Fig. 2.9 shows the total potential determined for a range of m values between the minimum and maximum m-values for the three different input powers 2.1. The dependence of the normalized coupling parameter, g, on the input laser power is shown in Fig. 2.10.

Rubidium

The potential depth associated with different m-values (orbital angular momentum quantum number) for ^{85}Rb is given in table 2.5.3 for different input laser powers, P_L= 30 mW, 10 mW, 1 mW, respectively. The radius of the fibre, a, and the wavelength

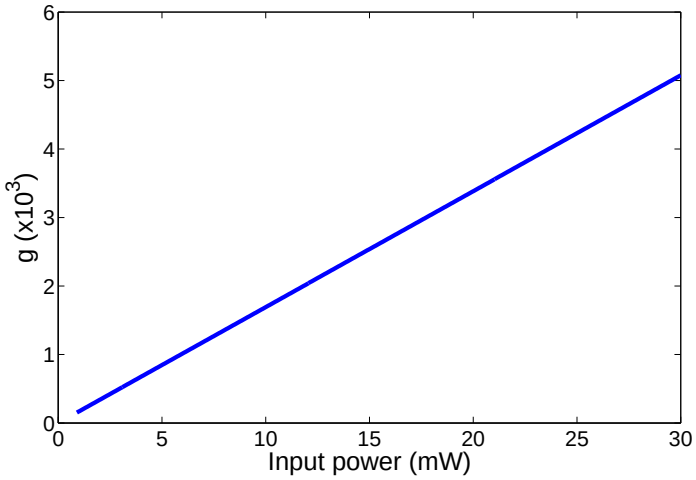

Figure 2.10: Dependence of the normalized coupling parameter, g, with the input intensity for ^{133}Cs atoms

of the detuned laser, λ_L are constant. The calculated recoil energy is $\Theta_{rec} = 970$ Hz (see Appendix A). The values of the corresponding trap depths are also determined by plotting the graph of effective potential (eqn. 2.5.4) Fig. 2.11 shows the total potential determined for a range of m values between the minimum and maximum m-values for the three different input powers (table 2.1). The dependence of the normalized coupling constant, g, with input laser power for Rb atom is shown in the

Table 2.2: Rubidium potential depths for varying parameters.

Fig. no.	$a[\mu$m]	P_L [mW]	λ_L [μm]	m_{min}	U_{min}	m_{max}	U_{max}
2.11(a)	0.5	30	1.55	380	12 μK	620	3 μK
2.11(b)	0.5	10	1.55	240	0.5 nK	390	0.01 nK
2.11(c)	0.5	1	1.55	90	0.5nK	120	12.6 pK

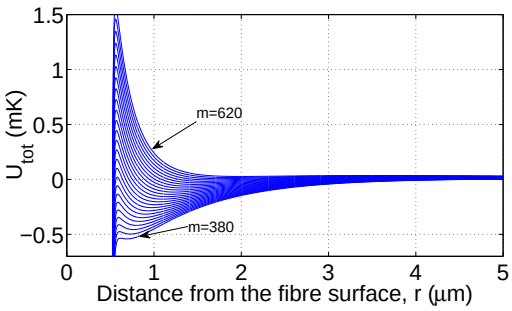

(a)

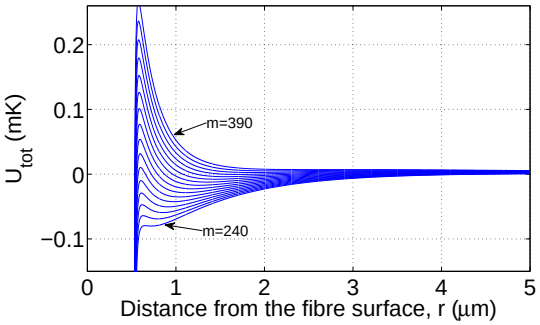

(b)

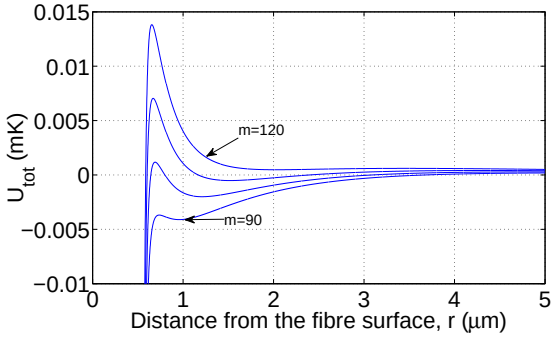

(c)

Figure 2.11: Total potential as a function of distance from the surface for a range of m values for ^{85}Rb, with $a = 0.5$ μm and $\lambda = 1.55$ μm. (a) for $P_L = 30$ mW, (b) for $P_L = 10$ mW, (c) for $P_L = 1$ mW.

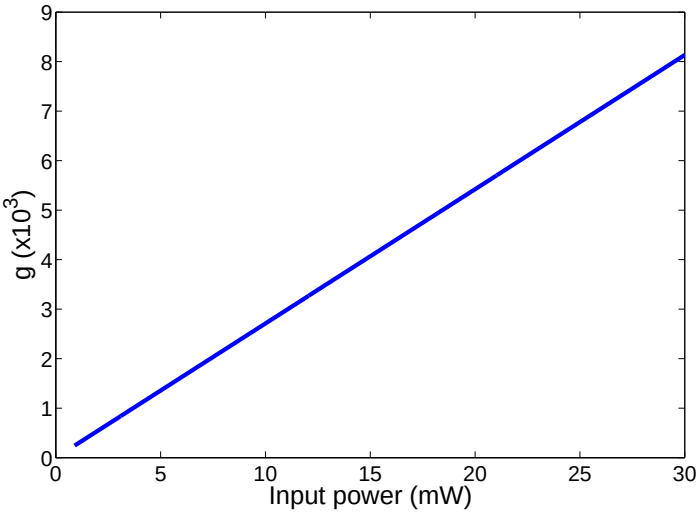

Figure 2.12: Dependence of the normalized coupling parameter, g, on the input power for ^{85}Rb atoms.

Fig. 2.12.

2.6 Conclusion

In this section, the parameters associated with the trapping of cold atoms using a tapered optical fibre were determined. The evanescent field extension outside a tapered optical fibre was calculated for different fibre diameters. An atom in an optical field was represented and the coupling of the atom with that of the electric field was calculated. This gives the indication of the output power, which can be detected using avalanche photodiodes (APDs). The details of using APDs are explained in chapter 4.

The influence of the van der Waals force on an atom near a tapered optical fibre was calculated. The effect due to the van der Waals force was determined in the

calculations of trapping potential for ^{133}Cs and ^{85}Rb atoms. Plots of total potentials as a function of the distance from the fibre surface for both the considered atomic samples were plotted. The trap depths were calculated, and this gave an indication of the possibility of trapping cold atoms in the traps around the tapered fibres. Trapping potentials for the parameters like, radius of the tapering, wavelength of the input light, and varying powers were plotted. This showed us the dependance of orbital angular momentum quantum number, m, on the input power.

The trap depth for the optical potential of ^{85}Rb atoms was calculated to be 0.3 mK. Therefore, typical cold atom samples of 100 μK can be trapped in the optical potential. However, since the trap depth is not very shallow it is not a straight forward task to trap these atoms. A trap loading scheme would therefore have to be devised in order to efficiently transfer atoms from the MOT into the fibre traps.

Chapter 3

Atom microtraps based on near-field Fresnel diffraction - Theory

3.1 Introduction

During recent years there has been a growing number of experimental studies on the development of, and applications for, neutral atom traps [60–65]. A new, and insufficiently studied approach to the development of miniature atom traps involves the optical near-fields formed by the diffraction of laser light on small, circular apertures in thin screens. This approach is of interest with a view to fabricating an array of atom microtraps and, accordingly, producing a large number of trapped atomic microensembles from a single initial atomic cloud or beam. Earlier work [66] has shown that an array of atom dipole traps can be produced by focusing a laser beam on an array of spherical microlenses. The work presented in this chapter relies on a more recent proposal [67], whereby microlenses, formed in thin screens, are used to focus

atomic beams.

Similar to other approaches employing laser fields, the operation of neutral atom, near-field microtraps is based on the use of dipole potentials and their corresponding dipole gradient forces. However, in contrast to other approaches, in which the gradient force is due to the non-uniform field distribution over the laser beam cross-section or over the wavelength of the laser light, in the near-field microtraps the gradient force is associated with the optical field non-uniformity over the *aperture* diameter. Consequently, atom microtraps can store atomic microclouds with characteristic dimensions equivalent to or less than the field wavelength. Such microclouds could be used for site-selective manipulation of atoms in the field of quantum information technologies [68, 69].

A quantitative analysis of near-field, atom microtraps with a characteristic size of apertures exceeding the optical wavelength is discussed here. Near-field Fresnel diffraction occurs when the diffraction pattern changes as a function of its distance from the aperture, due to the short distances over which the light field propagates. Such diffraction is characterized by a Fresnel number, $N_F \geq 1$. Analysis of the field distribution in the vicinity of a small, circular aperture in a thin screen is shown. Also, the dipole potential of the atom in the diffracted field is calculated. The analysis of Fresnel microtraps shows that, at a moderate intensity of the light field of about 10 Wcm^{-2}, the traps are able to store atoms with a kinetic energy of about 100 μK during time intervals of around one second.

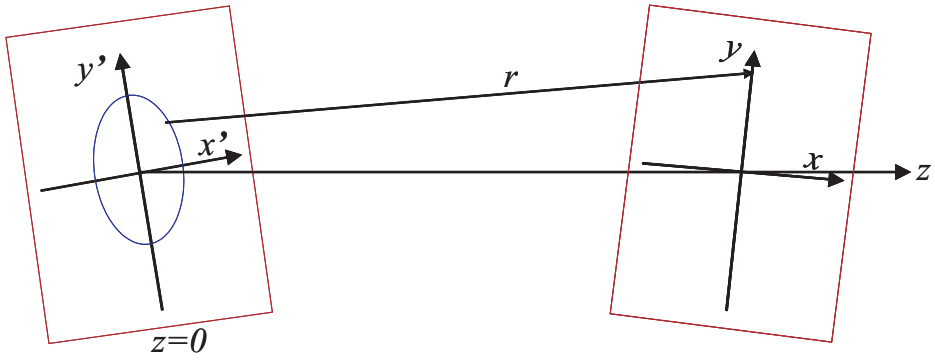

Figure 3.1: Geometry for circular aperture diffraction. The aperture plane and image plane are shown.

3.2 Fresnel Diffraction

In general, the Fresnel diffraction occurs because, each point on the wavefront is a source of secondary disturbance, and the secondary wavelets from different points mutually interfere. Fresnel diffraction occurs when a light-wave passes through an aperture and diffracts in the near field. This causes the diffraction pattern to differ in size and shape, relative to the observation distance from the aperture. A schematic of the geometry for circular aperture diffraction is shown in Fig. 3.1. When the distance is increased, the outgoing diffracted waves become planar and Fraunhofer diffraction occurs.

By red-detuning laser light incident on the aperture from an atomic resonance transition, one can make an attractive potential for the atoms and this trapping technique is discussed in the following.

3.3 Trapping Potential

The Fresnel atom microtraps are schematically shown in Fig. 3.2. A single microtrap can be analysed by considering the diffraction of a travelling light wave of arbitrary polarisation on a circular aperture

$$\mathbf{E}_1 = \mathbf{e}E_0 \cos(kz - \omega t), \tag{3.3.1}$$

where $\mathbf{e}$ is a unit polarisation vector, E_0 is the amplitude and $k = \omega/c$ is the wave vector. For the case when the size of the aperture exceeds or is equivalent to the wavelength of the optical field, the electric field behind the aperture can be represented in the scalar approximation as

$$\mathbf{E}_2 = \mathbf{e}E = \mathbf{e}\mathrm{Re}(\mathcal{E}\mathrm{e}^{-i\omega t}), \tag{3.3.2}$$

where $\mathcal{E} = \mathcal{E}(\mathbf{r})$ is the complex field amplitude. The diffracted field can be evaluated by applying the Rayleigh-Sommerfeld diffraction formula [70]

$$\mathcal{E}(x, y, z) = \frac{E_0}{2\pi} \int\int \frac{\exp(ikr)}{r} \left(\frac{z}{r}\right) \left(\frac{1}{r} - ik\right) dx'dy', \tag{3.3.3}$$

where the distance between the point (x, y, z) in the observation plane and the point $(x', y', 0)$ in the aperture plane is $r = [z^2 + (x - x')^2 + (y - y')^2]^{1/2}$, and the integral (3.3.3) is considered to be taken over the aperture region.

The evaluation of the Rayleigh-Sommerfeld integral can be simplified by taking into account the axial symmetry of the diffracted field. By introducing cylindrical coordinates ρ', ϕ' in the aperture plane and cylindrical coordinates ρ, ϕ in the observation plane, one can rewrite the diffracted electric field as

$$\mathcal{E}(\rho, z) = \frac{E_0}{2\pi} \int_0^a \int_0^{2\pi} \frac{\exp(ikr)}{r} \frac{z}{r} \left(\frac{1}{r} - ik\right) d\varphi\rho' d\rho', \tag{3.3.4}$$

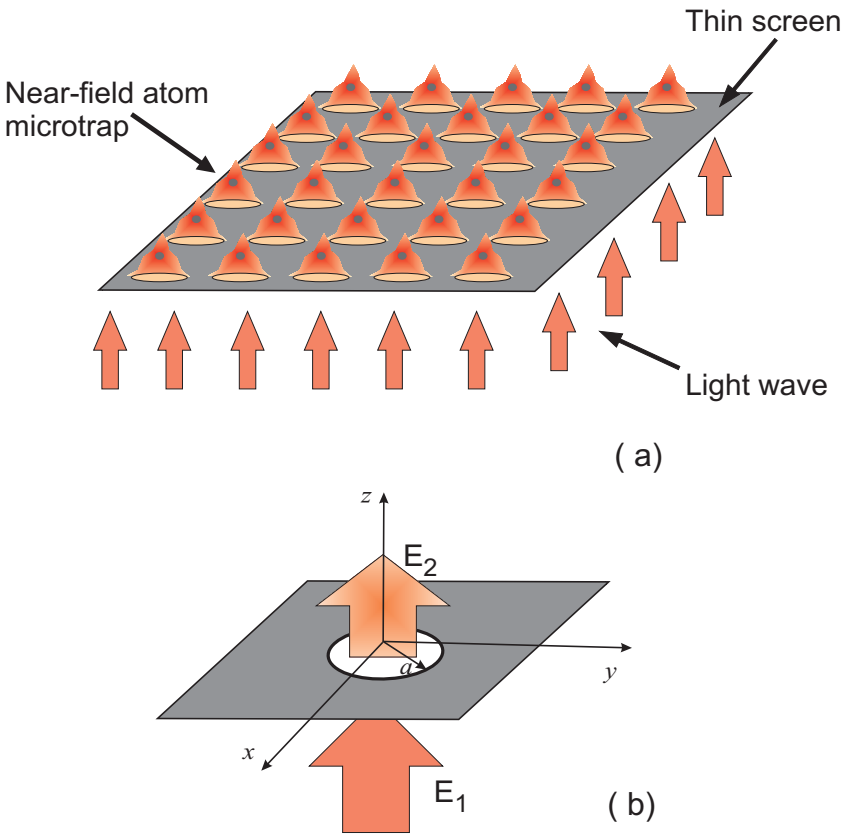

Figure 3.2: (a) An array of atom microtraps produced by near-field optical diffraction; (b) Schematic of a single microtrap consisting of a circular aperture of radius, a. E_1 represents the incoming light field and E_2 is the diffracted near-field.

where now $r = \left[z^2 + \rho^2 + \rho'^2 - 2\rho\rho'\cos\varphi\right]^{1/2}$, and $\varphi = \phi' - \phi$ is the relative angular coordinate.

For a red-detuned light field, the potential of a single microtrap is defined by the usual equation [23],

$$U = -\hbar\frac{\Omega^2}{|\delta|}, \tag{3.3.5}$$

where $\Omega = dE/2\hbar$ is the Rabi frequency, and $\delta = \omega - \omega_0$ is the detuning of the light field with respect to the atomic transition frequency, ω_0. Accordingly, for the diffracted field represented by Eqs. (3.3.2) - (3.3.4), the potential of the atom in the microtrap can be written as

$$U = -U_0\frac{|\mathcal{E}|^2}{E_0^2}, \tag{3.3.6}$$

where

$$U_0 = \frac{3}{8}\frac{\gamma}{|\delta|}\frac{E_0^2}{k^3}. \tag{3.3.7}$$

U_0 is a characteristic value of the potential and γ is half the spontaneous decay rate. Now, consider the case when the radius of the aperture only slightly exceeds the optical wavelength. In this case the Fresnel number, N_F, is expected to be approximately equal to one, i.e.

$$N_F = \frac{a^2}{\lambda z_m} \approx 1, \tag{3.3.8}$$

where z_m is a characteristic distance from the aperture to the maximum of the electric field intensity. Accordingly, the electric field intensity is expected to have a single diffraction maximum and the atom potential will have a single minimum. An example of a single-minimum atom potential is shown in Fig. 3.3 for different values of the vertical coordinate, z.

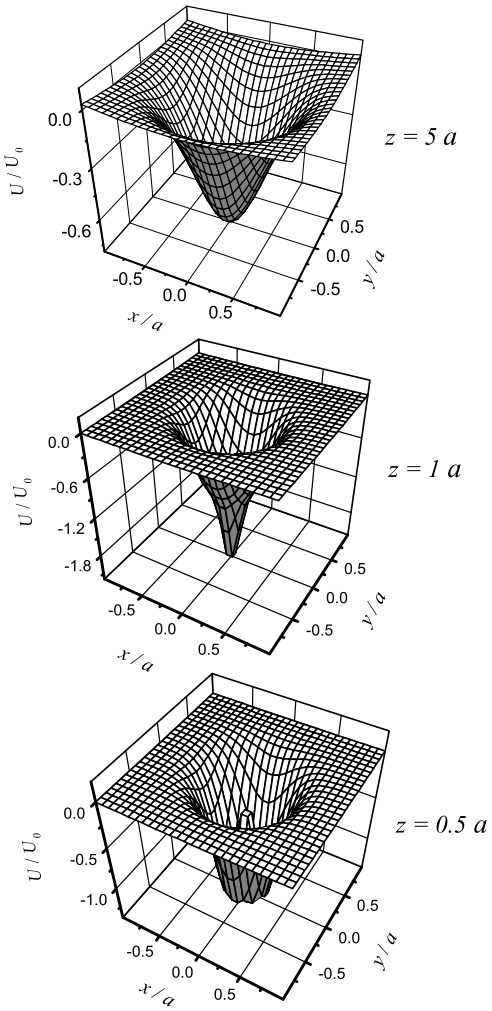

Figure 3.3: Atom potential in a Fresnel atom microtrap as a function of transverse coordinates for radius $a = 1.5\lambda$ ($ka = 9.4$), at distances from the aperture $z = 0.5a$, $z = 1a$, and $z = 5a$. (See Appendix C for mathematica coding of the above plot).

Alongside the integral-representation of the diffracted field used above, and the corresponding potential of the atom in the diffracted field, one can also find an analytical representation of the atom potential near the symmetry axis of the microtrap. This can be done by decomposing the integrand in Eq. (3.3.4) into a series of small displacements $\rho \ll a$ [67, 71]. By making use of the result of refs. [67, 71], to second order in ρ, one can represent the near-axis atom potential as parabolic in the transverse direction,

$$U(\rho, z) = -U_0 \left\{ 1 + \frac{z^2}{R_a^2} - \frac{2z}{R_a} \cos k(R_a - z) \right. \\ \left. - \frac{k^2 a^2 z \rho^2}{2R_a^3} \left[\left(1 - \frac{3}{k^2 R_a^2} \right) \left(\frac{z}{R_a} - \cos k(R_a - z) \right) + \frac{3}{kR_a} \sin k(R_a - z) \right] \right\}, \tag{3.3.9}$$

where $R_a = \sqrt{a^2 + z^2}$. The potential represented in (3.3.9), when considered as a function of the vertical coordinate, z, has a minimum at a value of $z = z_m$ defined by the transcendental equation

$$\cos\left[k(R_a - z) - \chi\right] = \frac{a^2 z}{(a^2 + z^2)^{3/2}} \frac{1}{(A^2 + B^2)^{1/2}}, \tag{3.3.10}$$

where $\tan\chi = B/A$, with $A = a^2/(a^2 + z^2)$ and $B = kz\,(1 - z/R_a)$.

The dependence of the near-axis value of the potential, $U = U(0, z)$, on the vertical coordinate, z, is shown in Fig. 3.4 for the same relative value of the aperture size as in Fig. 3.3. Also, the 3-dimensional graph of the potential on z-axis is shown in Fig. 3.5. The near-axis potential has a minimum at a vertical coordinate $z_m = 1.47a = 2.2\ \lambda$. In accordance, the Fresnel number, $N_F \simeq 1$ at this value of z_m, and the atom potential has a single minimum.

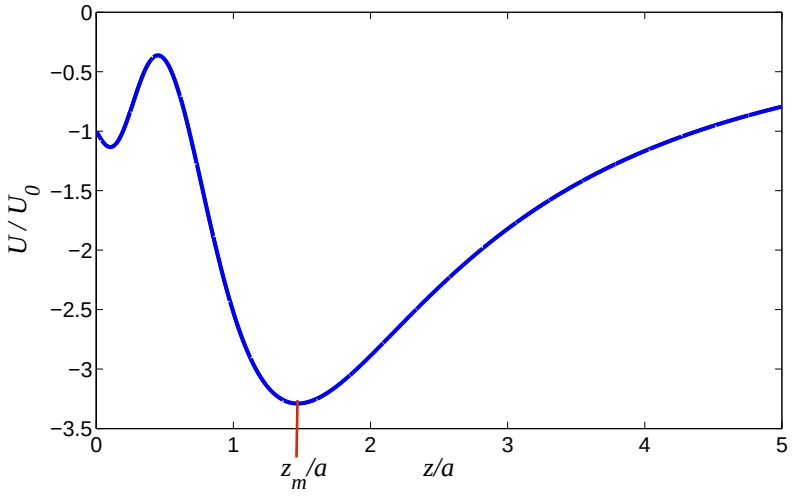

Figure 3.4: Atom potential near the axis of the Fresnel atom microtrap as a function of the vertical coordinate, z, for $a = 1.5\lambda$.

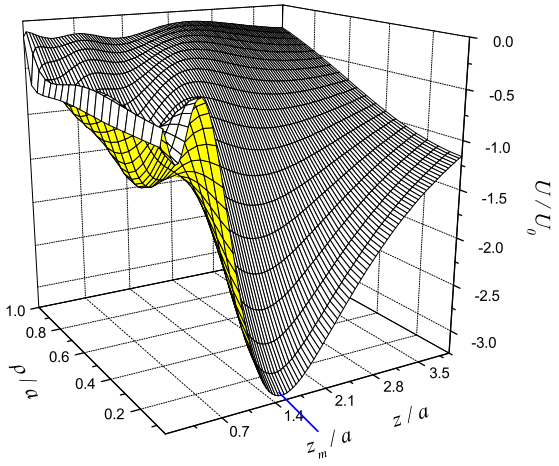

Figure 3.5: A 3D graph of the atom potential near the axis of the Fresnel atom microtrap as a function of the vertical coordinate z, for $a = 1.5\lambda$. (See Appendix B for a mathematica program to generate the values for above graph).

3.4 Parameters of Near-Field Microtraps

Parameters of the Fresnel atom microtrap are evaluated by considering ^{85}Rb atoms which interact with a far-detuned light field at the dipole transition $5^2S_{1/2}(F = 3) \longrightarrow 5^2P_{3/2}(F = 4)$ with wavelength $\lambda = 780$ nm. For this transition, the natural linewidth is $2\gamma = 2\pi \times 5.98$ MHz and the saturation intensity is $I_S = 1.6$ mW/cm^2 [57].

By considering the radius of the microtraps as above, i.e. $a = 1.5\lambda = 1.2$ μm, then the minimum of the trap potential is located at z_m. Choosing as an example, a laser intensity $I = 10$ W/cm^2 and a large negative detuning $\delta =$ -$10^4\gamma$, one can evaluate the depth of the potential well in the positive transverse direction as $U_\rho = 0.15$ mK and in the vertical direction as $U_z = 0.13$ mK.

By considering the trapping potential as harmonic, one can calculate the spring-constant, β, of the trap in ρ- and z-directions. At first, the characteristic value of the potential, U_0, can be calculated using the eqn. 3.3.7, and by substituting $E_0^2 = 8\pi$ I/c, one can write

$$U_0 = \frac{3\pi}{c}\frac{\gamma}{\mid \delta \mid}\frac{I}{k^3}, \tag{3.4.1}$$

where $k = 2\pi/\lambda$; with $\lambda = 0.78$ μm, $\delta = -10^4\gamma$, $I = 10$ W/cm^2 and $c = 3 \times 10^8$ ms^{-1}, in the above eqn. 3.4.1, one gets, $U_0 = 6 \times 10^{-28}$ J $= 3.75 \times 10^{-9}$ eV $= 45$ μK [1]. The values of the potential depths along transverse, U_ρ and vertical, U_z directions can be determined from the Fig. 3.5, and are dimensionless, because of the second derivative of the potential function (eqn. 3.3.9). Then, the spring-constant along the transverse direction, $\beta_\rho = U_\rho \times U_0 = 3.3 \times 45$ μK $= 6.76 \times 10^{-15}$ kgs^{-2}, and in vertical direction as, $\beta_z = U_z \times U_0 = 2.93 \times 45$ μK $= 2.07 \times 10^{-15}$ kgs^{-2}.

Using the values of the spring-constants, the trap oscillation frequencies along the positive transverse and vertical directions are calculated by the formula

$$\nu = \frac{1}{2\pi}\sqrt{\frac{\beta}{M}}, \tag{3.4.2}$$

as $\nu_\rho = 34$ kHz and $\nu_z = 19$ kHz, respectively.

The energy levels near the bottom of the trapping potential can be estimated as

$$E = h\nu_\rho\left(n_\rho + \tfrac{1}{2}\right) + h\nu_z\left(n_z + \tfrac{1}{2}\right). \tag{3.4.3}$$

The number of quantized energy levels in the microtrap potential can be estimated to be about 50, with a lowest energy, $E_0 = 1.3$ μK, and an energy separation, $\Delta E = 2.6$ μK. Characteristic oscillation amplitudes of the atom in the ground state, $\bar{\rho} = \sqrt{\hbar/M\omega_\rho}$ and $\bar{z} = \sqrt{\hbar/M\omega_z}$, where $M = 1.45 \times 10^{-25}$kg is the mass of the atom,

[1] 1 eV $= 1.2 \times 10^4$ K

are evaluated as $\bar{\rho} = 60$ nm and $\bar{z} = 80$ nm, respectively.

The lifetime of the Fresnal atom microtrap can be evaluated by taking into account the diffusion broadening of atomic velocities due to photon recoil fluctuations. For this process, the velocity diffusion coefficient, $D = \gamma v_r^2 (I/I_S)(\gamma/\delta)^2$, where $v_r = \hbar k/M = 5.8$ mms^{-1} is the recoil velocity, I is the light field intensity, and I_S is the saturation intensity. Assuming that the kinetic energy of an atom escaping from the trap is approximately equal to the potential well depth, $U_d = Mv^2/2$, and the atomic velocity is defined by the diffusion broadening, $v^2 \approx D\tau$, one can evaluate the trap lifetime, τ, as

$$\tau = \frac{2U_d\gamma^{-1}}{Mv_r^2}\left(\frac{I_s}{I}\right)\left(\frac{\delta}{\gamma}\right)^2. \tag{3.4.4}$$

Substituting the above chosen parameters for ^{85}Rb atoms in the eqn. 3.4, a trap lifetime of $\tau \simeq 0.6$ s has been achieved. Table 3.1 shows the comparison between rubidium and cesium atoms for the same input intensity of 10 Wcm^{-2} and detuning, $\delta = -10^4\gamma$. The lifetime can be increased by increasing the input laser power, which in turn increases the trap depth. With such trap lifetimes one can perform atom optics experiments by blending micro-fabrication technology with cold atoms [66]. An important point to note here is that an individual microtrap uses only about 0.5 μW in the above considered case of radius $a = 1.2$ μm.

3.5 Conclusion

A novel trapping scheme has been proposed on a system of neutral atom microtraps, based on a series of circular apertures in a thin screen. Laser light incident on the screen, produces an array of potential minima for atoms in the near-field. The above analysis shows that these near-field atom microtraps can store cold atoms for times

Table I

Atom	U_d [mK]	ν_ρ [kHz]	ν_z [kHz]	$\bar{\rho}$ [nm]	$\bar{z}$ [nm]	τ [s]
^{85}Rb	0.13	34	19	60	80	0.6
^{133}Cs	0.17	29	14	51	73	1

Table 3.1: Parameters of near-field Fresnel diffraction trap for ^{85}Rb and ^{133}Cs atoms with the input laser power of 10 mW/cm^2 and detuning, $\delta = -10^4\gamma$ for an aperture radius, $a = 1.5\lambda$.

up to seconds. The potential well depth of the microtraps is mainly determined by the intensity of the incident laser field and the detuning. By varying these two parameters one can achieve robust control over the trap parameters. A numerical analysis for ^{85}Rb atoms shows that a trap depth of 0.13 mK can be achieved, with storage times up to 0.6 seconds at an incident laser intensity of 10 Wcm^{-2}. The trap oscillation frequencies in the transverse and vertical directions are also calculated, and estimated that there are ≈ 50 energy levels near the bottom of the trapping potential, with $E_0 = 1.3$ μK and $\Delta E = 2.6$ μK. By considering the radius of the circular aperture, $a = 1.5\lambda$, it is shown that the Fresnel number ~ 1, indicating that we are in the near-field regime. An increase in the radius will result in higher order diffraction occurring, thereby increasing the Fresnel number and, hence, producing a greater number of microtraps. However, the trap depth will diminish as we move away from the center of the aperture.

The basis for future research will be to study the above discussed atom microtraps in more detail by taking into account the dipole-dipole interaction between the atoms, and the finite values of the atomic de Broglie wavelength.

Chapter 4

Detection schemes for matter-light interactions - Experiments

4.1 Interactions between Cold Atoms and Light

The main aim of the experiments carried out in our laboratory is to investigate light-matter interactions using laser-cooled rubidium atoms and the evanescent light field of a tapered optical fibre(c.f. Chapter 2 for the theoretical considerations). A magneto-optical trap [72] is used to provide the source of cold atoms. Average thermal temperatures of ~ 100 μK, and approximately 10^7 atoms, are routinely achived. As detailed in Chapter 1, a MOT provides three dimensional cooling and trapping of the atoms in a 3-beam retro-reflection MOT design. The laser beams are circularly polarised, with opposite polarisation for each pair of retro-reflected beams. The trapping potential is provided by a pair of Helmholtz coils in anti-Helmholtz configuration, leading to a magnetic field gradient of 13.5 Gcm^{-2}. SAES Rb getters are used to provide the rubidium within the UHV system. The experiment is conducted in ultra-high vacuum (UHV) to reduce collisions between particles- that would result

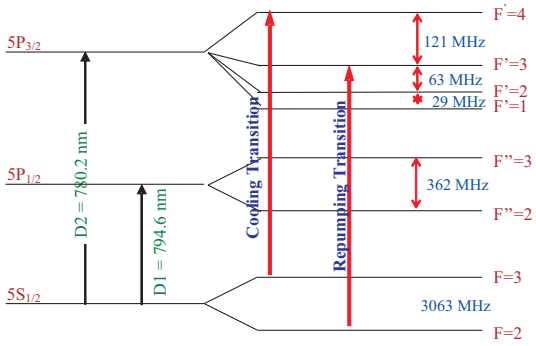

Figure 4.1: Energy-level diagram of the ^{85}Rb isotope.

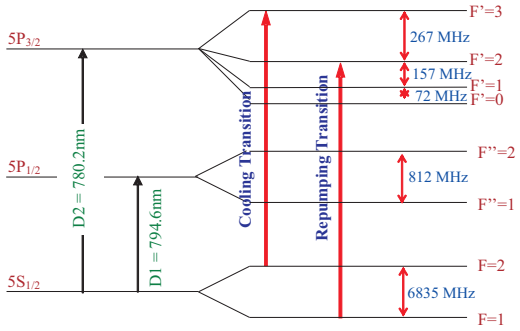

Figure 4.2: Energy-level diagram of the ^{87}Rb isotope.

in heating of the rubidium atoms. The typical pressure within the vacuum chamber is ≈1x10^{-9} mbar. Among the two stable isotopes of Rb; ^{85}Rb and ^{87}Rb energy-level diagrams are shown in Fig.4.2. The cooling beams assist the transition of atoms from the $F = 3$ ground state $S_{1/2}$ to the $F^{'} = 4$ upper state $P_{3/2}$. Approximately, one in 1000 atoms undergoes the transition to the $F = 2$ ground state, following the selection rules, $\Delta m_F = 0, \pm 1$, and is, therefore, lost to the cooling laser. Therefore, another laser called the re-pumper is used to pump the atoms from the $F = 2$ to the $F^{'} = 3$ level.

A tapered optical fibre of radius < 0.5 μm is incorporated vertically into the vacuum chamber, while ensuring that it is centered in the cloud of cold atoms. The

two ends (both input and output) of the fibre pass through a machined teflon ferrule in order to ensure that the vacuum is tight [49], without damaging the fibre. The advantage of using a tapered, commercial single-mode fibre (SMF) as compared to a fibre pulled from bulk material is that the fibre can be easily spliced to standard fibre optic components at the input and output, thereby ensuring ease of integration into the experimental setup.

In order to study light-matter interactions, two crucial techniques were required: light coupling into single-mode fibres SMF and low light level detectors. Laser light, on resonance with the cooling transition of Rb around 780 nm, must be coupled into the fibre in order to generate the evanescent field at the tapered region. By scanning the frequency of the coupled light using an acousto-optical modulator (AOM), a resonance absorbtion dip is expected when atoms absorb the on-resonance evanescent light at the tapered region. Theoretical estimates show that the number of atoms interacting with the light field is very low, typically 5 atoms/second [49], due to the short extension of the evanescent field into the region around the fibre and the atomic cloud density. Hence, very sensitive light detectors are needed in order to detect this small change in transmitted signal through the fibre.

This chapter contains details on these two crucial aspects: (i) how to efficiently couple the probe light into a tapered single mode fibre and (ii) how to choose appropriately sensitive detection schemes, including avalanche photodiodes and single photon detectors for absorption measurements.

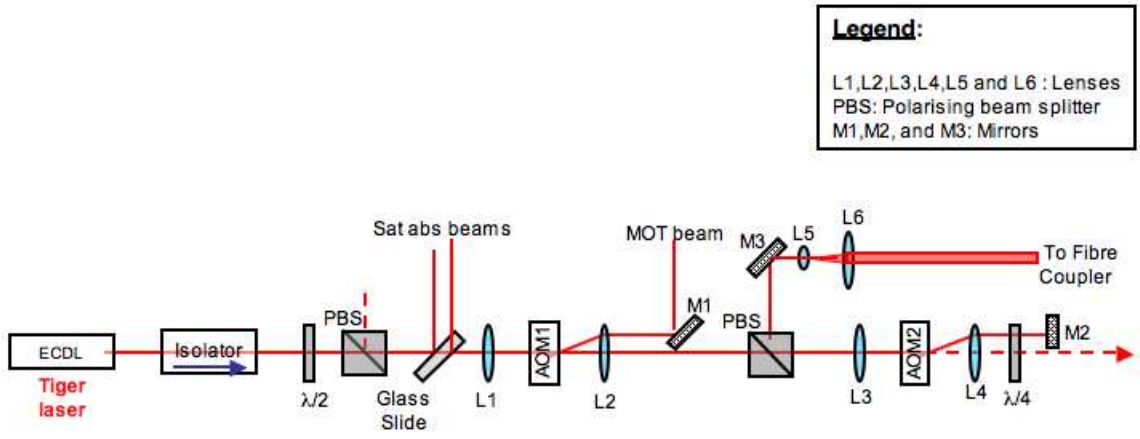

Figure 4.3: Schematic of the optical setup showing the beam for coupling into the fibre, which leads into the vacuum chamber.

4.2 Coupling Probe Light into SMF

The tapered optical fibre is very delicate once placed inside the UHV system and can easily break if too much light (> 1 mW) is coupled into it, due to heating at the taper region. The probe beam used for the taper experiments corresponds to the 1^{st} order diffracted beam from the main laser cooling beam after AOM2 (c.f. Fig. 4.3). For the on-resonance interaction of the cold atoms with the evanescent field, the probe laser must be tuned to the same transition as the MOT beams. This is achieved by AOM2 in a double-pass configuration as shown in Fig. 4.3. In order to ensure that the probe power was sufficiently low, the beam was passed through a Thorlabs collimator (F810FC-780) with a fibre connector at the output end. This coupler has a numerical aperture, NA= 0.25 and focal length, f = 35.90 mm. The output of the coupler can be connected to the fibre via an FC connector. Initially, the output from the collimator was connected to an optical spectrum analyser (OSA), to determine the probe power. Using a series of attenuators (neutral density filters) up

to ND3 (10^{-3}) the power was reduced to < 1 mW. Thereafter, the output from the collimator was removed from the OSA and directly connected to the FC connector spliced to the tapered fibre. The input power into the tapered fibre was varied and measured using Thorlabs power meter (PM100), and the transmitted power through the tapered fibre was measured using the OSA, shown in Fig.4.4. It is clear from the graph that there is a linear dependence between the input and the output power.

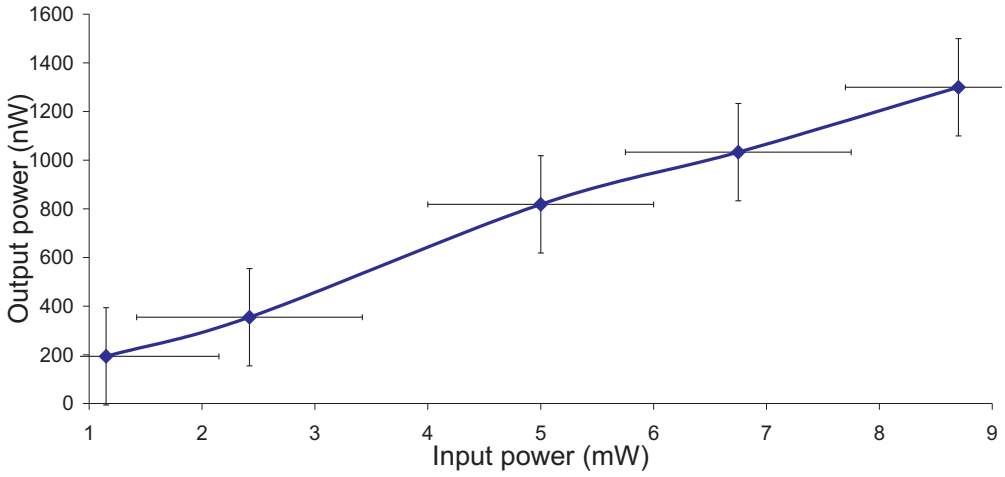

Figure 4.4: Plot of transmitted power out of the taper versus input power into the taper.

4.3 Low Light Level Detectors

4.3.1 Introduction to avalanche photodiode (APD)

An APD is, basically, a p-n diode with a high gain. It consists of two regions: (i) an absorption region, where the input light on to the APD is absorbed, and (ii) a multiplication region, in which a high electric field is exhibited to provide internal photo current gain impact ionisation. The schematic of a p-n diode APD is shown

in Fig.4.5. Most APDs are made from silicon and are useful for wavelengths from

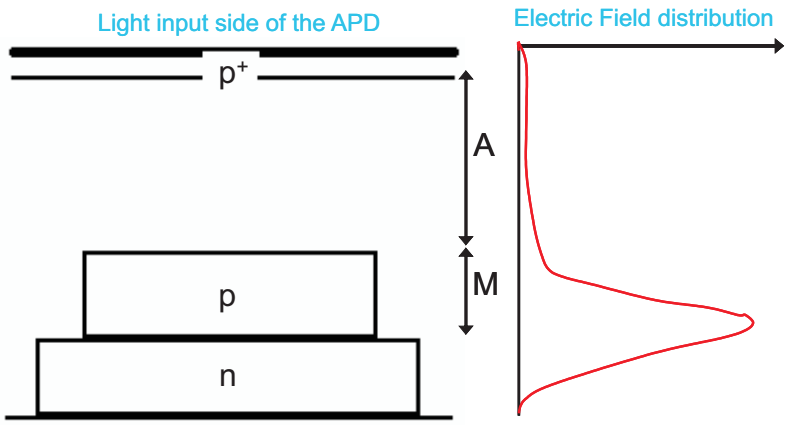

Figure 4.5: A reach-through structure of APD is shown. 'M' is the multiplication region, where the electric field is maximum, so as to trigger impact ionisation and provide photocurrent gain.

450 nm - 1 μm, thereby making them suitable for experiments involving laser-cooled Rb atoms, which absorb light at around 780 nm. In an APD, when light is incident on the diode, photo-generated electron-hole pairs are created in the depletion region. These electron-hole pairs are accelerated to their saturation velocity by an electric field present in the depletion region, as shown in Fig. 4.5. If a charge carrier gains sufficient kinetic energy, it may, on collision with the atoms in the crystal, release additional carriers by impact ionisation. Each additional carrier produced by impact ionisation is then accelerated by the electric field and may also undergo impact ionisation, thereby producing multiple carriers from the original photogenerated carriers. This process leads to carrier multiplication and is known as *avalanche* multiplication.

4.3.2 The Tyndall National Institute APD

The initial efforts on low light level detection concerned a device fabricated within Tyndall National Institute[1]. A simple circuit (Fig. 4.6) was used to bias the APD in reverse bias condition. In order to test the operation of an APD one relies on the principle that when no light is incident on the APD, the resistance of the diode is infinite. In contrast, if light falls on the APD when it is set at maximum gain, the resistance of the diode approaches zero and, therefore, a high current will be measured through the load resistance, R. Initial steps to test the APD involved modulating the

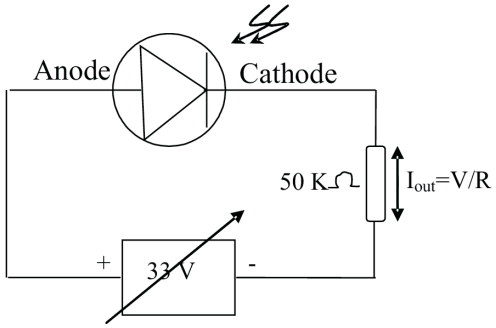

Figure 4.6: Reverse bias operation of the APD

light incident on the APD using a Thorlabs optical chopper (MC1000A) at 15 Hz (Fig. 4.7). The output voltage was measured by connecting an oscilloscope across the load resistance, which in turn gives an indication of the output current from the APD. This experiment was done for varying bias voltages. The choice of 15 Hz chopping frequency is because the modulated signal was clearly distinguishable at this frequency. Fig. 4.8 shows the voltages recorded across the load for bias voltages of 28 V, and 31.9 V. The power incident on the diode is 13 mW, using a He-Ne laser

[1]The device was obtained from Dr. Alan Morrison, Dept. of Electronics and Electrical Engineering, University College Cork

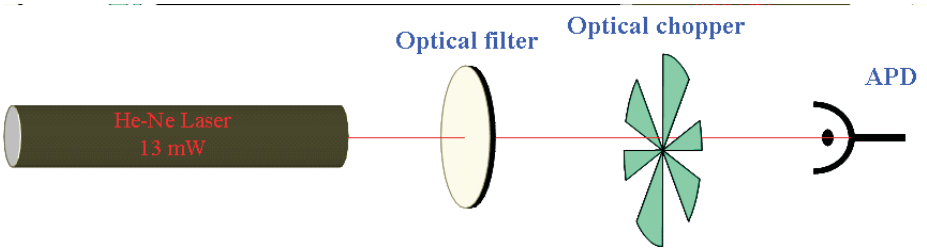

Figure 4.7: Schematic experimental set-up. The optical signal beam is measured using the avalanche photodiode.

source for all tests. Notice that there is no significant change in the output voltages at the bias voltage up to 28 V (Fig. 4.8a). 31.9 V was an optimum bias voltage for which a good signal was obtained (Fig. 4.8b). By zooming on to the graph for a bias voltage of 31.9 V, we clearly observe a large output voltage of 6.22 V, as shown in Fig. 4.9.

The next tasks required were to (i) measure the optimum bias voltage for the APD, (ii) suppress noise using a lowpass filter, and (iii) to amplify the signal.

4.3.3 Determining the optimum bias voltage for the APD

(i) Experimental conditions

An APD of diameter 100 μm^2 was used in order to have a maximum area of sensitivity for the incident light. The large size also faciliated the alignment of the light onto the diode. A 633 nm, 13 mW He-Ne laser was used. The incident light intensity was reduced by using a neutral density filter (NDF) of 3, thereby reducing the input light by three orders of magnitude. Therefore, the light impinging on the APD was 13 μW. As before, the frequency of the optical chopper set to 15 Hz. In order to decrease the external noise, it was essential to perform the test measurements in the

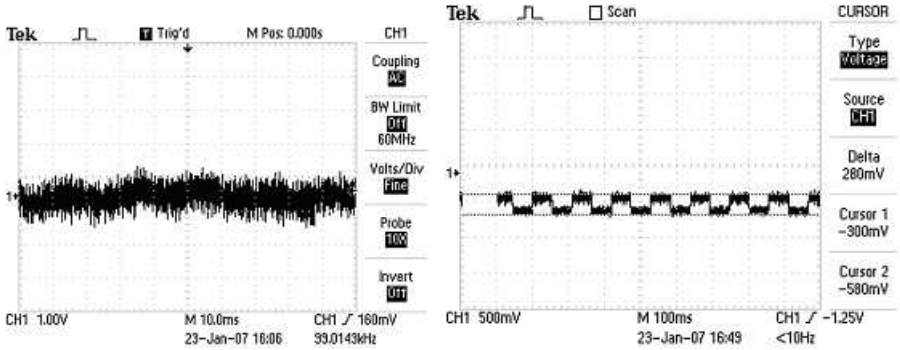

(a) (b)

Figure 4.8: (a) A bias voltage of 28 V was used and the input beam power, P = 13 mW. (b) A bias voltage of 31.9 V was used and the input beam power, P = 13 mW. This was also the optimum bias voltage at which a maximum signal output for the chosen APD of 100 μm^2 was obtained.

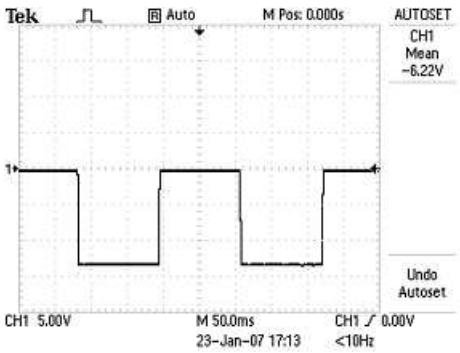

Figure 4.9: A signal obtained from the APD output for the following parameters is shown. Bias voltage = 31.9 V, Chopping frequency = 15 Hz, and input beam power = 13 mW.

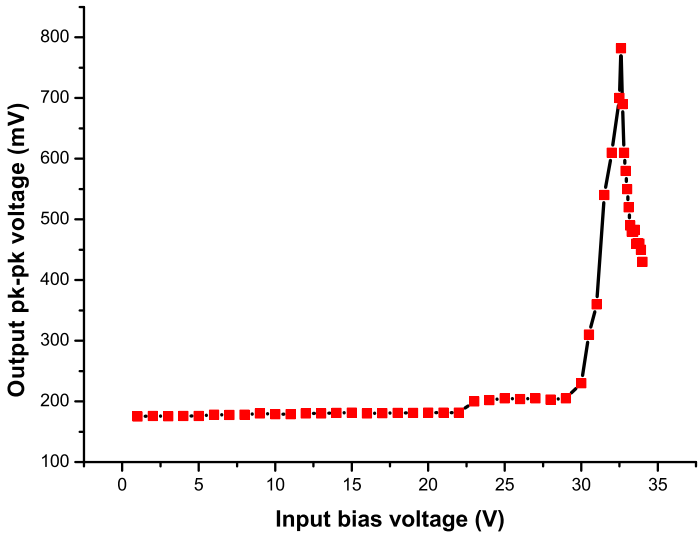

Figure 4.10: Peak-to-peak output voltage across the load as a function of the bias voltage. The incident power of the light is constant.

dark. However, there was still reasonably large noise present because of the circuit itself. By plotting the output peak-to-peak voltage across the load as a function of bias voltage, one can determine the optimum bias voltage. Fig. 4.10 shows the data obtained and one can readily determine that the optimum bias voltage is -32.6 V.

(ii) Multiplication factor of the APD

The multiplication factor of an APD is a measure of the number of electrons (or holes) created inside the APD due to one photon impinging on the detector. At the optimum bias-voltage of -32.6 V, the maximum output voltage is 782 mV for a load resistance of 50 kΩ. The corresponding current flow across the load resistor is 15.6 μA. The input beam power was measured to be $P = 13$ μW (after the NDF of factor 3). The incident

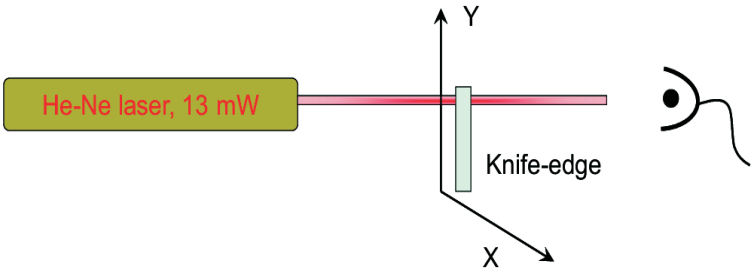

Figure 4.11: A schematic of technique to measure the beam diameter is shown. The knife edge is movable in the X-Y plane. The power is measured by moving the knife in small steps.

energy, E corresponding to a power of 13 μW is 13 μJ. The energy of a single 633 nm photon is given by $E = h\nu = 3.14 \times 10^{-19}$ J. Therefore, the number of photons per second incident on the APD is, $n = E/E_\nu = 4 \times 10^{13}$. One can determine the current, I_{photon}, due to a single photon as, I_{photon} = (1photon)(15.2$\times 10^{-6}$A) / (6.36$\times 10^{13}$photons) = 2.4$\times 10^{-19}$ A. In order to determine how much of the He-Ne light is actually falling on the detector sensor area, one needs to know the beam diameter of the He-Ne laser. A standard method to measure the beam diameter is explained below.

(iii) Determination of the beam size of the He-Ne laser

A basic technique to measure the beam diameter of a laser involves blocking the beam in small steps using a knife-edge and measuring the power of the beam, as illustrated in Fig. 4.11. A plot of knife-edge position versus laser power gives a cumulative distribution function as shown in Fig. 4.12. The derivative of this function gives a plot of the intensity distribution of the beam. A full-width half maximum (FWHM) measure of this profile yields the diameter of the beam (c.f. Fig.4.13). From Fig. 4.13, one can infer that, at FWHM, the diameter of the laser beam is 400 μm.

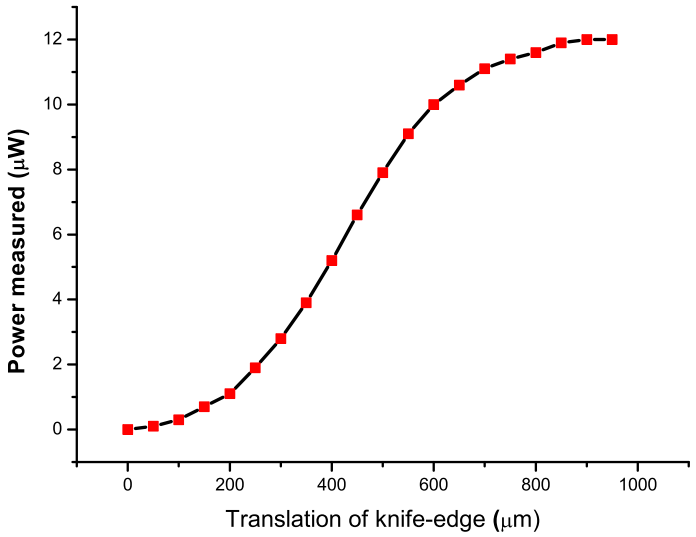

Figure 4.12: Cumulative distribution function of the power of the He-Ne laser.

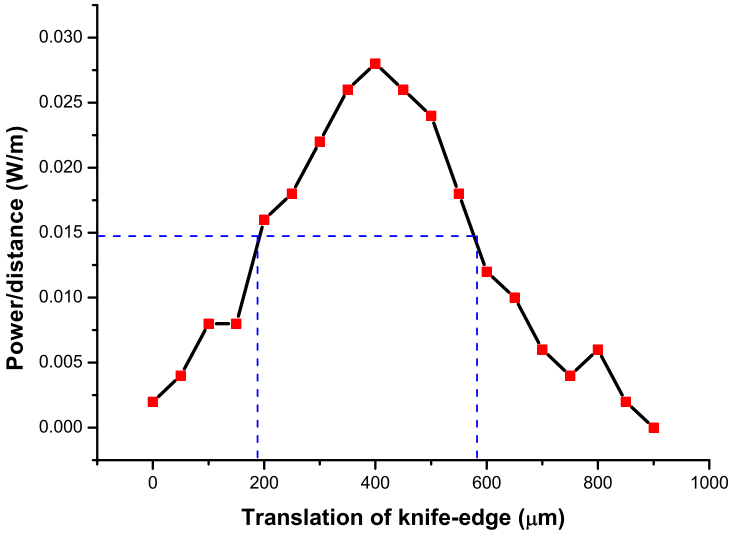

Figure 4.13: Profile of the He-Ne laser, showing the FWHM points.

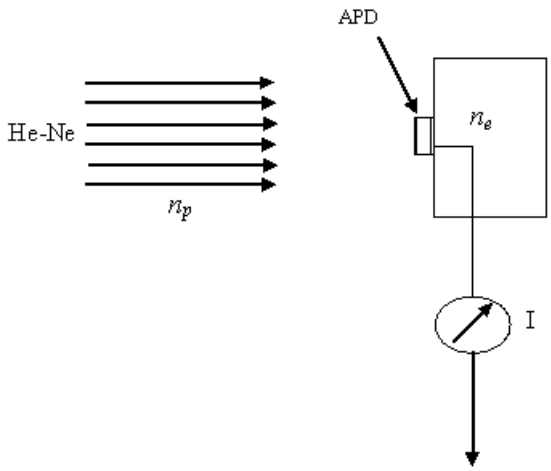

Figure 4.14: Pictorial representation of the incident number of photons, n_p and number of electrons created, n_e.

Considering the beam to be symmetric (i.e. the aspect ratio is 1), one can calculate the number of photons in the beam.

If we assume a Gaussian beam profile, the area of the beam, $A_{beam} = \pi r^2 = 0.125$ mm^2. Also, the maximum input power falling on to the APD is 13 μW. The number of photons per second, N, associated with a power of 13 μW is equal to $(13 \times 10^{-6}$ W$)/(3.14 \times 10^{-19}$ J$) = 4.1 \times 10^{13}$ photons/sec. The number of photons per second impinging on the APD of area, $A_{APD} = 100$ μm^2 can be calculated as,

$$n_p = \frac{A_{APD} \times N}{A_{beam}} = 3.3 \times 10^{10}. \tag{4.3.1}$$

The number of electrons created by absorption of these photons is:

$$n_e = \frac{I_{out}}{e} \tag{4.3.2}$$

where $I_{out} = 0.2 \times 10^{-6}$ A is the current output and $e = 1.6 \times 10^{-19}$ C is the charge of electron. By using the above values in eqn.4.3.2, we find that $n_e = 1.3 \times 10^{12}$ electrons/s. Therefore, the multiplication factor can be written as $n_e/n_p = 39.6$. In

other words, for each photon incident on the APD, it produces ≈ 40 electrons by the process of impact ionisation.

(iv) APD testing with a passive low-pass filter

To reduce the noise in the output signal, a low-pass filter was used in the circuit as shown in Fig. 4.15. A low-pass filter consists of a resistor and a capacitor, and can also be called an R-C filter. This type of filter is basically used to smoothen the output signal. The cut-off frequency of the filter is determined by the values of resistance and capacitance and is given by

$$f_c = \frac{1}{2\pi RC}. \tag{4.3.3}$$

For a resistance, $R = 10$ kΩ and a capacitance, $C = 0.1$ μf the cut-off frequency is 159 Hz.

If one compares the bias circuit incorporating the low-pass filter (Fig. 4.16) to that with no filter (Fig. 4.10), one can infer that, (a) the signal quality is improved and the noise is reduced, and (b) there is no 'kink' around 24 V when the low-pass filter is used, but rather a slow increase after 24 V. The frequencies below 159 Hz are allowed to pass through the resistor and the ones above this value are bypassed to the ground through the capacitor.

(v) APD testing with an active low-pass filter

Our aim was to use the APD to measure very low light level signals. To achieve this task, one needs an APD with a very high sensitivity, so that it can respond to a low light signal. One also needs a good circuit with adequate amplification to multiply the low light levels. An active low-pass filter consists of an opamp (operational amplifier),

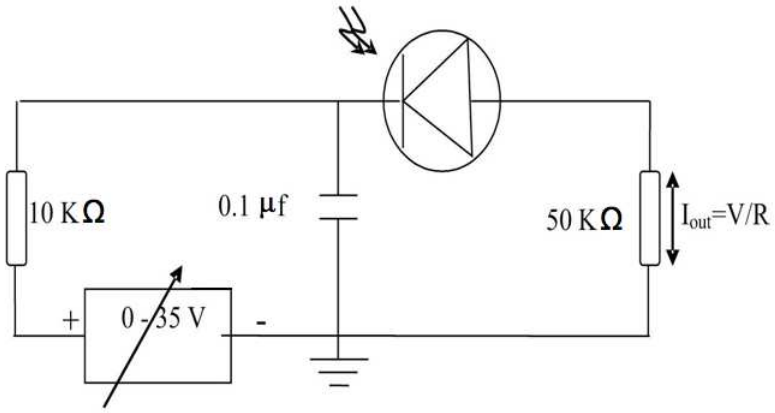

Figure 4.15: Biasing circuit with a passive-low-pass filter.

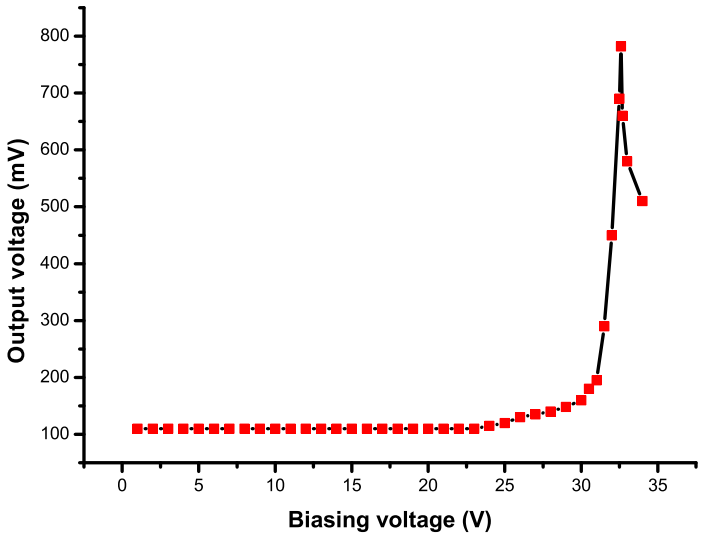

Figure 4.16: APD response with a passive low-pass filter.

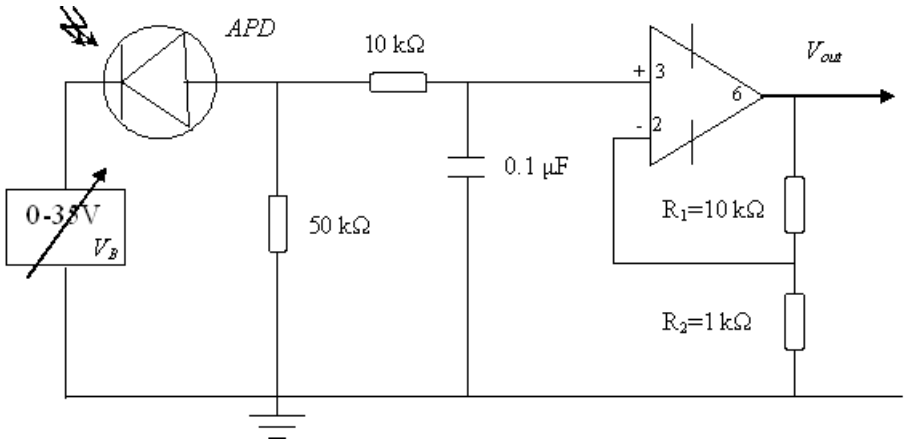

Figure 4.17: Active low-pass filter with gain for the APD.

and, in this case, a standard LM741 was used for the amplification. A low-pass filter with this amplifier circuit acts as an active low-pass filter, shown in Fig.4.17. In order to increase the output signal, i. e., to increase the sensitivity of the APD. The above circuit is designed to include a gain circuit. The incident beam power, P= 12 μW. The cut-off frequency given by, $f_c = 159$ Hz. Gain, $A = R_1/R_2 + 1 = 11$. As one can see in Fig. 4.18, the signal is amplified to the Volts range from the milli-volts range that was observed using the passive low pass filter (c.f. Fig. 4.16).

We also tested to determine the lowest power that could be detected by the APD. Three optical filters with a combined attenuation of 10^{-9} were used and a bias voltage of -32.6 V was applied. Under these experimental conditions the peak-to-peak voltage, V_{out}, was equal to 400 mV. Fig. 4.19 shows V_{out} for a laser power of 13 pW incident on the APD. Hence, the minimum number of photons that this APD can detect with an active low-pass filter is ≈ 3.1 photons at 633 nm. The lowest detection of 13 pW was achieved during the testing. Later, the circuit was put into the box to make a module and a micro-glass-slide was affixed at the input window of the APD to safeguard the

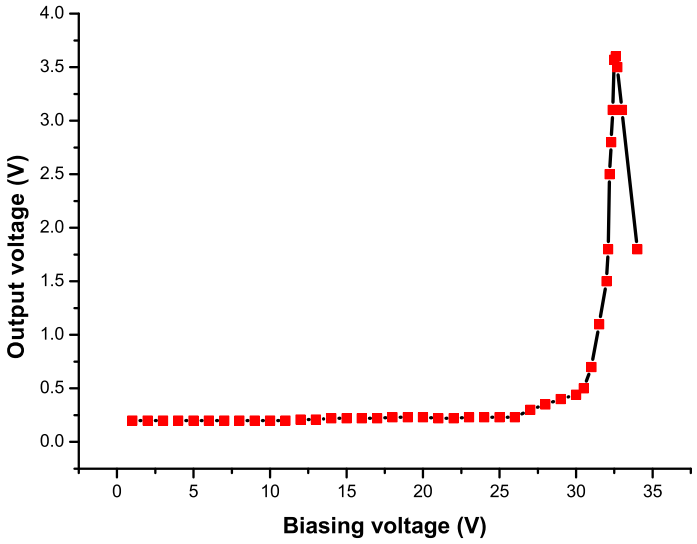

Figure 4.18: APD response with amplification after a low-pass filter.

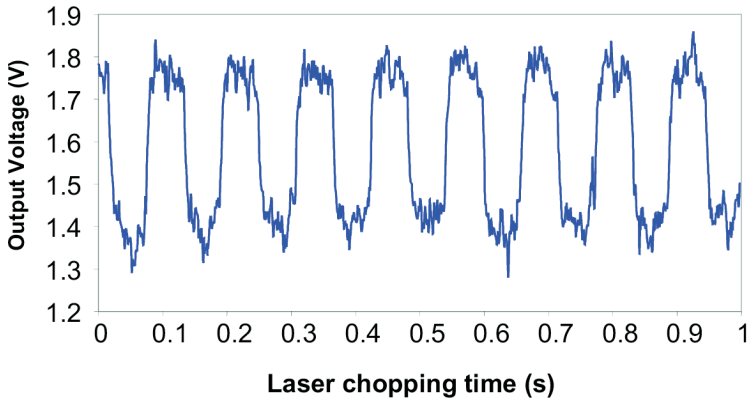

Figure 4.19: Temporal evolution of the output voltage of the APD for an input optical power of 13 pW and with a reverse biasing voltage of 32.6 V.

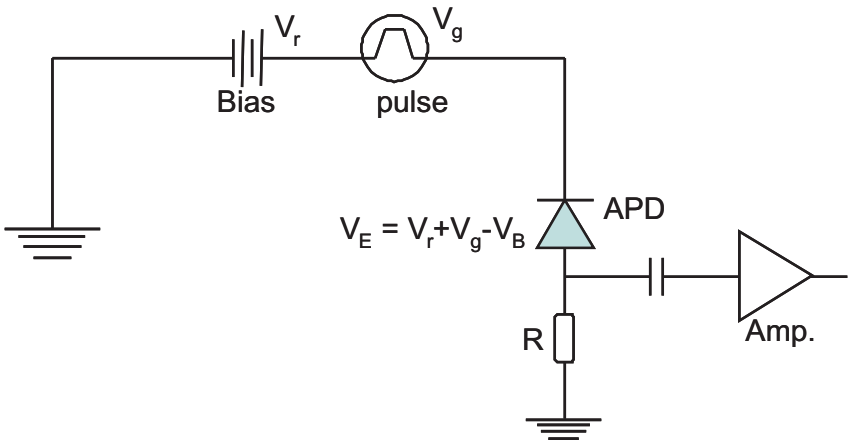

Figure 4.20: Geiger mode operation circuit. V_r is the reverse bias voltage, V_g is amplitude of the gate-pulse, V_B is breakdown voltage of the APD, and V_E is excess voltage above V_B from the gate-pulse. Amp. is the amplifier circuit for the signal output from the APD.

bonding. Due to this, the minimum detection level was reduced to the range of nW.

4.3.4 Single photon detectors

(i) Geiger mode operation

The bias voltage at which there is a sudden increase (or avalanche) in the voltage drop across the load resistance is called the breakdown voltage, V_{BR}. In the Geiger mode operation, an APD is biased above its breakdown voltage ($V_R > V_{BR}$) and it will conduct a large current. The bias circuit is shown in Fig. 4.20, and the corresponding pulse voltage given is shown in Fig. 4.21 below.

4.3.5 EG&G PerkinElmer detector

When the input laser beam coupled into the fibre (inside the vacuum chamber) is around the same cooling transition of ^{85}Rb, ($5S_{1/2} \rightarrow 5P_{3/2}$), it is viewed to satisfy the

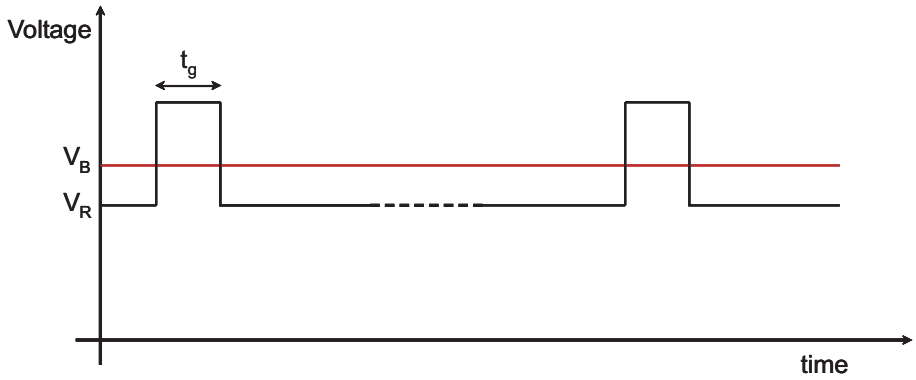

Figure 4.21: Schematic of voltage and time parameters. Here, t_g is the width of the gate-pulse or detection window.

on-resonance condition. The on-resonance experiment involves a very small number of atoms interacting with the evanescent field around the fibre, thereby yielding very low signals for detection. Because of this, we need to use high sensitivity detectors such as photon counting modules to see any changes in the light signal. We chose to use a PerkinElmer photon counting module (PCDM) sensitive to light at 780 nm and with a saturation limit of 10^7. Before using the detector, it was important to ensure that the light levels would not saturate the detector, thereby causing damage to the PCDM.

The number of photons, n, is calculated as

$$n = \frac{E_0}{E_p} \tag{4.3.4}$$

where E_0 is the energy of the light (laser in our case) and E_p is the energy due to one photon at that wavelength. Considering $\lambda = 780$ nm, we can determine E_p using

$$E_p = h\nu = \frac{hc}{\lambda} \tag{4.3.5}$$

Hence, we determine that $E_p = 2.55 \times 10^{-19}$ Joules. To calculate E_0, one considers

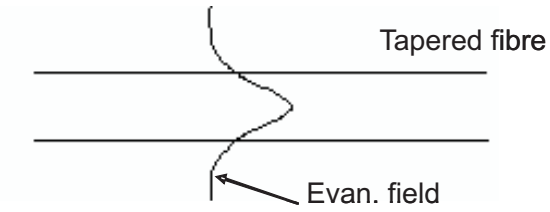

Figure 4.22: Schematic of the evanescent field outside a tapered optical fibre.

the saturation intensity, I_S, of rubidium using the formula

$$I_S = \frac{hc\pi\Gamma}{3\lambda^3} \tag{4.3.6}$$

and we have already shown that, $I_S = 1.6$ mW/cm^2 for rudibium atoms, [23] or 16 pW/μm^2, in the small volume of the evanescent field around the tapered part of the fibre. Therefore, the input probe beam power should be less than $P_0 = 15.5$ pW, in order not to saturate the atoms. The equivalent energy per second is $E_0 = P_0 \times$time$= 15.5 \times 10^{-12}$ J. Hence, the number of photons to be detected is 6×10^7.

(i) The number of photons absorbed in the reaction

The photon scattering rate formula is given by,

$$R = \frac{(I_0/I_S)\pi\Gamma}{1 + I_0/I_S + 4\left(\Delta/\Gamma\right)^2} \tag{4.3.7}$$

where I_S is the saturation intensity, I_0 is the intensity of the probe beam, Δ is the detuning and Γ is the natural line-width of the excited state. In the on-resonance case for rubidium atoms, $\Delta = 0$ and $\Gamma = 6$ MHz.

To calculate I_0, consider the evanescent field outside a tapered optical fibre as shown in Fig. 4.22. Consider an atom at a distance of 1/e from the surface of the fibre. At this distance, the value of the saturation intensity drops to 36% of its initial value. Therefore, $I_0 = I_S \times 0.36$. By substituting these values into eqn. 4.3.7, one

gets $R = 4.98 \times 10^6$ s^{-1}. Therefore, the power loss is, $P_L = R \times E_p = 1.27 \times 10^{-12}$ W/atom. This is the power drop in the laser coupled into the fibre for one atom interacting with the evanescent field. By considering the volume of the evanescent field around the tapered optical fibre, V_{evan} (c.f. eqn. 2.3.7), and substituting $l = 2$ mm, the length of the tapering, $R_1 = 0.65$ μm, the radial distance from the centre of the fibre to the 1/e distance of the evanescent field, and $R_2 = 0.5$ μm, is the radius of the tapering, one gets, $V_{evan} = 1.1 \times 10^{-15}$ m^3. The number of atoms, N_{atoms}, in the cold atomic cloud volume, $V_{atom} = 4/3\pi r^3 = 4.2 \times 10^{-9}$ m^3 is considered to be 10^7. By these values, one can estimate that at any instant of time there will be < 5 atoms interacting with the evanescent field (c.f. eqn. 2.3.8). Typically, the drop in power because of the interaction of five atoms would be ≈ 6.35 pW. Therefore, the number of photons absorbed can be calculated as,

$$n_a = \frac{E_0 \times 6.35 \times 10^{-12}}{E_p} = 2.4 \times 10^7 \text{photons} \tag{4.3.8}$$

Hence, for $n_0 > n_a$, we can expect an absorption of 39.5% of the input intensity.

(ii) Testing single photon counting module (SPCM) EG&G (PerkinElmer)

The SPCM used was by EG&G PerkinElmer, model no. SPCM CD2882. The saturation limit is 10^7 counts/s, with a dark count of 350 counts/s. We used a gated photon counter, model SR400 by Stanford Research Systems (SRS). The SPCM output is fed into the input of the SRS photon counter using a BNC connection.

A specific procedure was adopted in order to measure the photon count. First, the 5 V biasing input was connected to the SPCM. Next, the output of the SPCM was connected to the SR400 using a BNC, and the SR400 was switched on. Only at this stage was the 5 V supply for the SPCM switched on and this enabled us to

measure the dark count rate.

After this measurement, one end of the tapered fibre was connected to the input of the SPCM for measuring the background count rate. Next, the repump laser was switched on and the count was recorded. Finally, the cooling laser and the Rb getters were switched on and the count recorded. An important point to note here is that, there should not be any sudden increase in the counts/s. i.e., not more than 10^7 counts/s. If that happens, turn off the power supply, else block the laser beams.

During the testing of the SPCM, the mounted tapered fibre inside the vacuum chamber broke because of high laser input intensity. This was not ideal and indicated that no more than 1 mW of power should be coupled into the tapered fibre. There were two sections of fibre within the chamber, one long and one short. The detector dark count was $\sim$ 350 counts/s. Using the long section, the background counts due to stray light in the room was $\sim$ 550 counts/s. When the repump light was switched on this increased to 10 kcounts/s. When the repump + cooling beams were on this increased to 37 kcounts/second, with 4.36 Amps in the Rb getters. However, there was no observable difference between the count-rate for the MOT present and the MOT not present. We accounted for a drop in the photon counts when getters were on: this could be due to the absorption of beams by the rubidium and then emitting in random directions.

(iii) GPIB interface with PC and photon counter(SR400)

A LabVIEW program was used to acquire the data from the SR400 photon counter interface and some details are shown in Figs. 4.23, 4.24 and 4.25.

The interfacing is established using a GPIB cable and the program is capable of giving real time changes to the photon counting signal. The data points seen on the

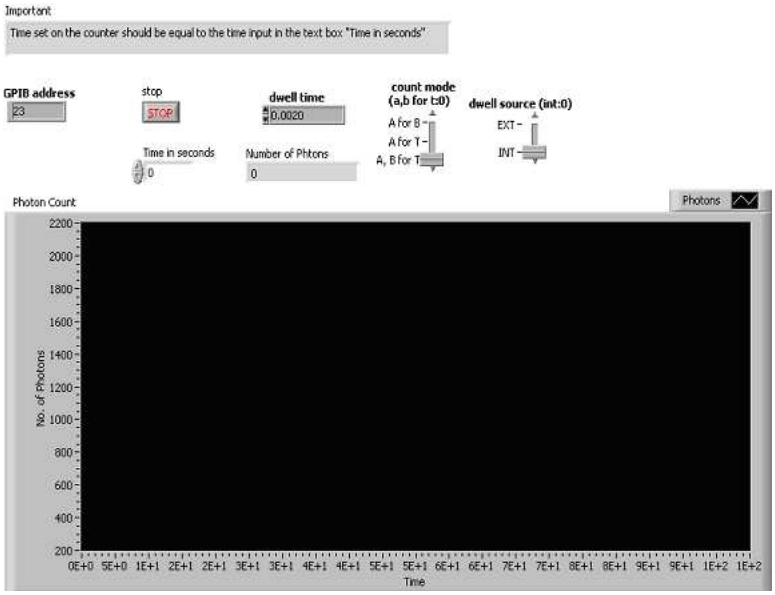

Figure 4.23: Front panel of the LabVIEW program to measure the photon counts from the EG&G detector

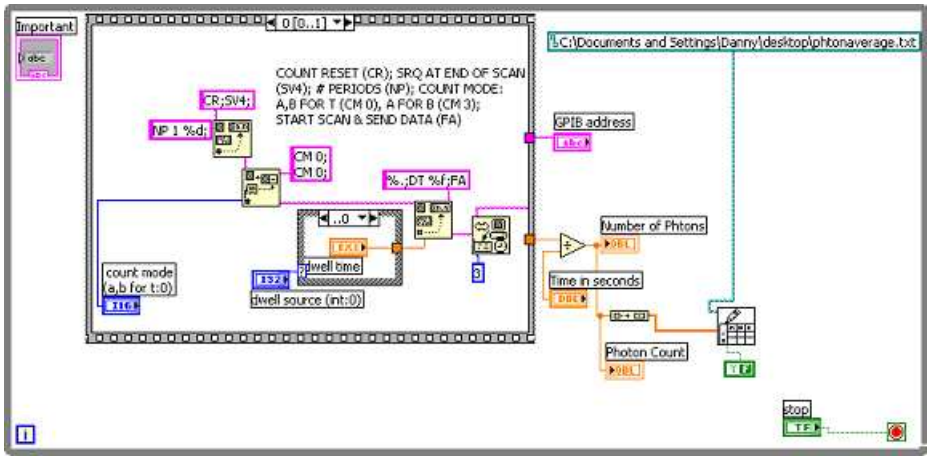

Figure 4.24: Block Diagram 1 showing the first sequence in the program where the data is scanned.

screen can be stored in as a .dat file. The data can be taken per second changes in the photon counts or also one can input the number of averages needed, to get an average signal. A front panel (c.f. Fig. 4.23) is provided for the user and allows one the user

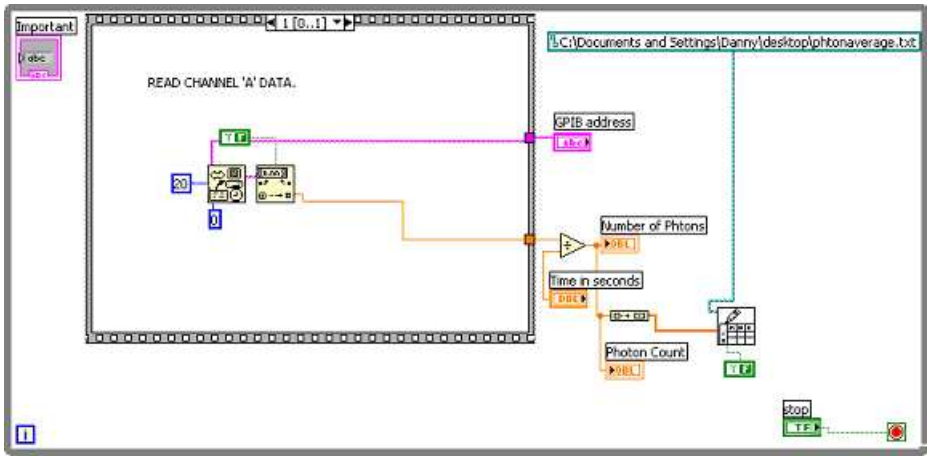

Figure 4.25: Block Diagram 2 showing the second sequence, where the data is read from the counter.

interactive area, through which an input can be given while running the program and also the output is displayed on the screen. The programming part of the LabVIEW is called as block diagram window, shown in Figs. 4.24 and 4.25.

4.3.6 Sensl pcstime2 detector

(i) Using the Sensl detector at the output end of the tapered optical fibre

A PCSTime photon counting module by SensL was also tested. SensL detectors are good candidates with a very low background count and noise and we tested the feasibility of incorporating the PCSTime detector into our experimental setup. The PCSTime has a quantum efficiency of 18% at 780 nm (Fig. 4.26), the wavelength of choice for Rb atoms. The specifications for the detector are given in the footnote. [2]

[2]Product Code: PCSTime20020X01F0, serial Number: 00000EC5A4EF, module Number: 7208, sensor Serial Number: Ch0: CSI 06-38-015 and Ch1: CSI 06-38-017. Here, Ch0 and Ch1 are the two sensors (APDs) in PCSTime detector.

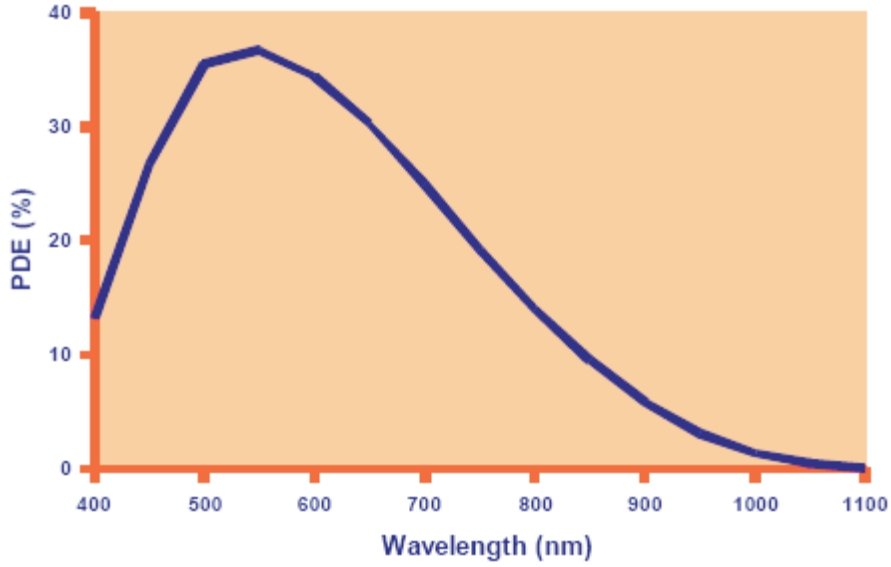

Figure 4.26: Photon detection efficiency vs. wavelength.

(ii) Calibration and measurement using pcstime module

According to the specification chart from the SensL, the temperature of the APD was set to -20^o C, the reference voltage was set as 200 mV, and the bias Voltage over breakdown, V_{br} was set as 5.1 V. The module was wrapped inside black cloth to make ensure no stray light falls on the detectors and all the lights in laboratory were switched off. Based on the initial tests, the conclusions drawn were that the data acquisition software provided with the detector crashed frequently. This resulted in frequent restarting of the software package. Another important aspect was that the module heats up in only a few minutes and the dark count increases appreciably during this time. The photon detection efficiency at near-IR wavelength is $< 8\%$, and there is a contribution to the photon counts in spectrum range when the detector heats up.

Because the PCSTime module is not designed for fibre coupling, it was difficult

to efficiently couple light onto the detector. To do this, it was essential to collimate the laser beam (< pW power) using a Thorlabs collimator (F810FC-780). The input beam to the fibre is taken from the first-order of the AOM2 as shown in Fig. 4.3 in the double-pass configuration. This beam is detuned to the cooling transition, and can be modulated to get the Rb absorption profile. The optical fibre into which the light is coupled is spliced onto the fibre which runs into the vacuum chamber. The output of the tapered fibre is spliced to a pigtail fibre that is connected to a GRIN lens (Oz Optics). This assists greatly in collimating the laser onto the PCSTime.

The collimated light falls onto the 20 μm SensL detector. The background light is blocked using black fabric, but even then the background count rate was 12 photons/s. An important point to be noted here is that there is a significant loss in the input coupling as there is no direct fibre coupling in the setup. This is also a major drawback of the PCSTime detector.

When a detectable number of photons fall on the detector, a few tests were made. At first the SensL counter response to the fluctuations was seen. We see the photon counts in the Figs. 4.27and 4.28 because, AOM1 (which shifts the frequency to the first order as the MOT beam) was not 'On', hence a greater number of photons was coupled into the fibre. Fig. 4.27 shows the photon counts as a function of time. The input light was irregularly modulated just before coupling to the fibre in order to see the counter's response. To check the sensitivity of the detector, the input light was chopped during a very short interval of time ($\sim$ ms). A sharp peak in Fig. 4.28 shows the quick response of the detector. As one can see, the sensitivity is in the microsecond range, which is good for our experimental conditions. In the Fig. 4.29, an important thing to be noted is that the MOT AOM (AOM1) is switched 'on' and

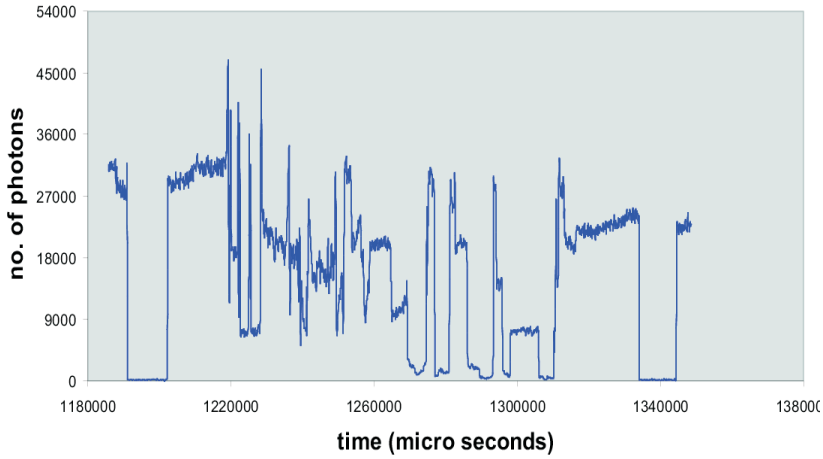

Figure 4.27: The SensL counter response to the input light

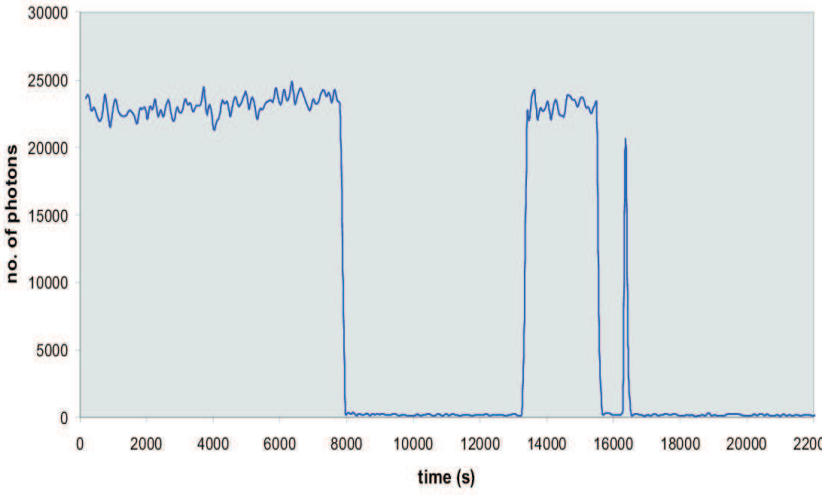

Figure 4.28: The sensitivity of the SensL detector

thus the number of counts has decreased to 8000 photons. The MOT beams were blocked for a short time and then unblocked in order to see if there was any change in the light coupled into the fibre. No significant change in the count rate was noticed. This gives the indication that no significant number of photons is being coupled into

the guided modes of the fibre.

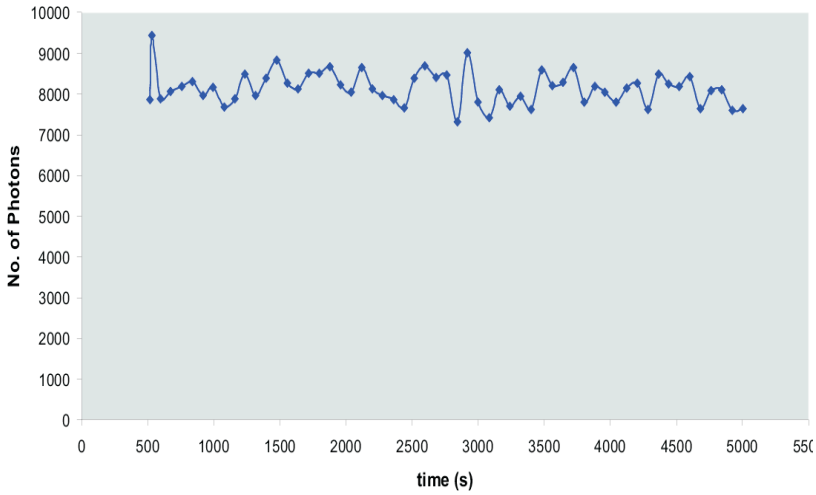

Figure 4.29: Measure of the number of photons as a function of time when the MOT beams are on and the tapered fibre is in the vacuum chamber.

4.4 Conclusion

To study the interactions between cold atoms and light it is important to have very sensitive light detection schemes. With this purpose in mind, a number of detectors were tested including a local APD, a PerkinElmer photon counter and a SensL PCSTime detector.

In order the cold atomic cloud to interact with the evanescent light, the evanescent wavelength should be also of the cooling transition. In order to achieve this, AOM2 was used, after which the beam is coupled into the fibre, which runs into the vacuum chamber. The output end is used for detection purpose.

Principle of APD was explained in brief. Since the dimensions of the APDs are in μm range, it is not easy to make the connections in order to work with it. In

order to facilitate this task, the APD is bonded using a gold wire bonding to a lead, to which one can easily connect the external circuit. This made working with these APDs a lot easier and clearly better packaging of these devices is crucial if they are to be easily integrated into realistic experiments. Tyndall has facilities for different bonding techniques/wires, of which the contacts are given in the footnote below. [3]

Geiger mode operation was explained. A single photon detector from EG&G PerkinElmer was tested. A LabVIEW program for the data acquisition from the PerkinElmer detector was shown. Measured counts using an SRS photon counter were also given.

According to the measurements done using the SensL PCSTime detector, no significant light was coupled into the guided modes of the fibre. This could be because the diameter of the tapered fibre was too large at about 1 μm. In order to overcome this problem, we would need to improve the fibre fabrication techniques to produce thinner fibres. Another reason for not seeing any coupled photons could be due to the input facet of the SensL detector. Therefore, better fibre coupling is very essential to get a good coupling efficiency.

[3](i). Gold bonding: Dan O'Connell, CFF, 1st Floor, Phase 1, Room no.1.05. (ii). Aluminium bonding: John Barton, MAI. Also, one can contact his student, Paul Tassie. (iii). Frank Stam, Senior Staff Researcher, Tyndall National Institute, Cork.

Chapter 5

Fabrication of Silica Disk Microcavities

5.1 Introduction

Over the past decade, strong interactions between light and matter at the single-photon level have enabled a wide set of scientific advances in quantum optics and quantum information science [9, 73–76]. Experiments with single atoms coupled to high-finesse Fabry-Pèrot cavities have been at the forefront of this area [77]. As a result of extreme technical challenges involved in improving the reflectivity of mirror coatings for these resonators, there has been increased interest in the development of alternative microcavity systems, which would enable such basic phenomena to be investigated.

Micron-sized, circular geometry cavities are characterised by their small mode volumes, high Q-factors reaching values of $>10^8$ [78] and small dimensions. The mode volume is the volume of the microdisk, in which the electromagnetic field is quantised and the Q-factor determines the confinement of the coupled light in the microcavity.

They offer potential as novel components for experiments ranging from the very applied, such as the realization of all-optical networks [79], to the fundamental, such as quantum optics experiments [80].

One class of circular microcavity is the planar dielectric microdisk which is of particular appeal due to its size reproducibility and surface finish since microfabrication techniques are used in its production. This translates directly into high Q-factor devices - viewed as the most important feature of these cavities.

A microcavity fabrication project (NAP112)was funded through Tyndall National Institute's National Access Programme. The initial aims of this project were (i) the fabrication of microdisks using Tyndall's facilities and (ii) to optimise the shape and smoothness of the fabricated microdisks. All images, results and discussions in this chapter derive from the NAP112 project.

Our interest in the fabrication of planar microdisks is to perform experiments in the framework of cavity quantum electrodynamics (QED). Such cavities could probe the interactions between single atoms and photons in lithographically fabricated microresonators, and may pave the way towards a wide range of applications such as the implementation of quantum networks and scalable quantum logic with photons [73].

5.2 Fabrication Details

The initial goal was the fabrication of planar microdisk resonators using the facilities in Tyndall through the National Access Programme. The focus was on the shape, size and finish of the structures. Etching of the sample in order to undercut the disk and to form a support pedestal was a vital consideration. The Q-factor of the disk

depends on the shape and smoothness, therefore the main aim was to concentrate on the surface smoothness of the disks. The general design approach consisted of an array of 100 μm diameter circular silicon dioxide disks was to be fabricated. The design of the microcavity disk consisted of a silicon dioxide circular disk of 2 μm thickness, on a mono-crystalline silicon pedestal.

5.2.1 Fabrication process flow

P-type silicon (100) wafer was used as a base substrate to fabricate the silicon dioxide. Silicon dioxide, also known as silica. Silica is found in abundance in nature in the form of quartz and sand. Its chemical symbol is SiO_2. The step-by-step process of the fabrication procedure for the planar silica disks is given below.

Step 1: Fabrication of SiO_2 disks

Initially, a 2 μm layer of (amorphous) SiO_2 was grown on a Si wafer using a Thermco 9000 furnace.Next, photoresist was spun on the SiO_2 layer and it was exposed using mask-1-disks. The mask used depended on the design configuration and will be further discussed in the following section. Megaposit SPR 220 positive resist was spun on and pre-baked with use of a Screen DNS Resist Develop Track. Fig. 5.1 is a schematic of the oxide growth on the Si substrate.

Step 2: Exposure and removal of the photoresist

The resist was exposed using mask-1-'Oxide Deposition' on an Electronics Visions Mask Aligner 420. It was subsequently developed with Microposit MF 26A, and any undeveloped resist was rinsed off. The oxide layer was then wet-etched using buffered

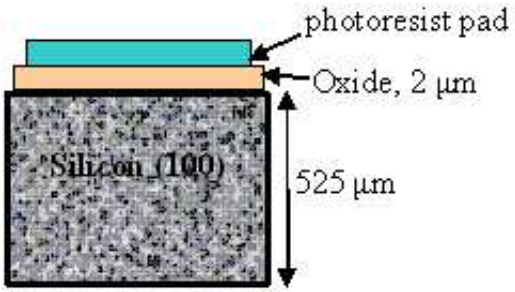

Figure 5.1: Schematic of the front elevation of SiO_2 grown on a Si substrate. The photoresist pad is also shown.

HF acid. An outline of this process is shown schematically in Fig. 5.2, in which the diagrams show only a single microdisk.

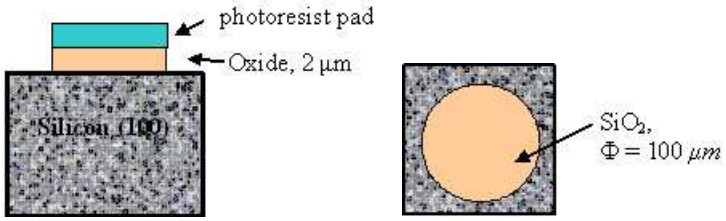

(a) (b)

Figure 5.2: (a) Front elevation of a sample after the wet-etching process; (b) Top view of sample after removing the photoresist pad. The SiO_2 disk is 100 μm diameter.

Step 3: Making the Si pedestals

The device was undercut to create Si pedestals using both dry- and wet-etch techniques. Both methods were tried to get the desired shape and dimensions as indicated in the schematic diagram below (c.f. Fig. 5.3. The SiO_2 was plasma etched with the use of a Trikon Omega 201 M0RI Etch System. Using the oxide as a hardmask, the trenches were etched 50 μm deep using two different isotropic etch methods: (i) A

plasma etch method using an STS ASE ICP etch tool with SF6 as a reactive gas and (ii) a vapour etch system using a XeF2 etch system by MEMSStar.

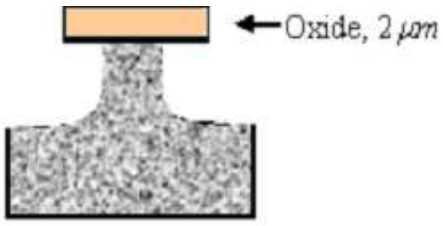

Figure 5.3: SiO_2 disk on a silicon pedestal after etching process.

5.2.2 Comparison of fabrication techniques

As this was the first time Tyndall made planar microdisks, there was a degree of uncertainty about which etching technique to use, wet-etching or dry-etching. In order to be sure before proceeding to the next step, the NAP112 project included a study on the results of both etching techniques. The scanning electron microscope (SEM) images of wet and dry etched disks are shown below in Figs. 5.4 and 5.5. When light is coupled into a microdisk, the light field propagation modes (known as whispering gallery modes or WGMs) are confined to the equator of the disk and lie near the disk's surface. By comparing the SEM images, one can see that the WGMs that would be excited in the wet-etched disk could consist of many resonant frequencies, due to the irregular size of the cavity. Such a feature would be of little use and, therefore, the dry-etching technique was selected in order to fabricate evenly sized planar silica disks.

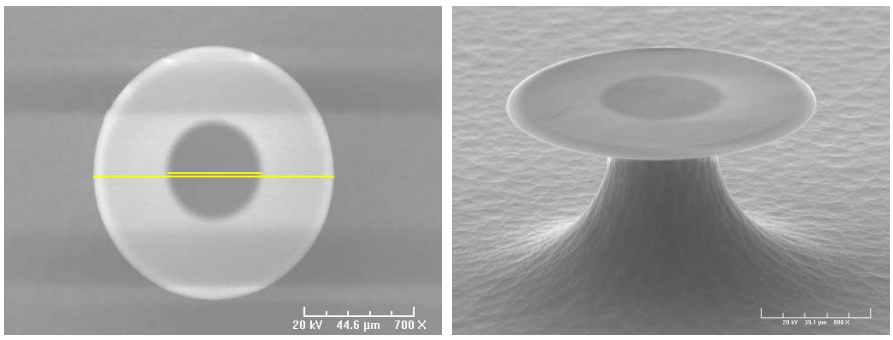

(a) (b)

Figure 5.4: SEM images of wet-etched disks: (a) Top view showing a near-ideal disk and(b) side view showing the disk and the pedestal.

5.3 Wafer Configuration of Microdisks

A number of different configurations of microdisks were fabricated so that they could be used for a variety of experiments. This included single disks of fixed diameter, disk arrays with constant separation between the individual disks, and disk arrays with varying distances between the disks. Each of the configurations will be discussed in the following.

5.3.1 Configuration I: Single disks

Configuration I consists of single microdisks of 100 μm diameter with a distance of 5 mm between each disk. This gap is required for coupling light into individual devices using a tapered optical fibre. After every 5 mm of gap scribe lanes were made. These are helpful for cutting the substrate to facilitate working with an individual disk. An important point to note about the under etching used to make the pedestals is that there is no uniformity of the under etch. This is because the access of the HF gas to

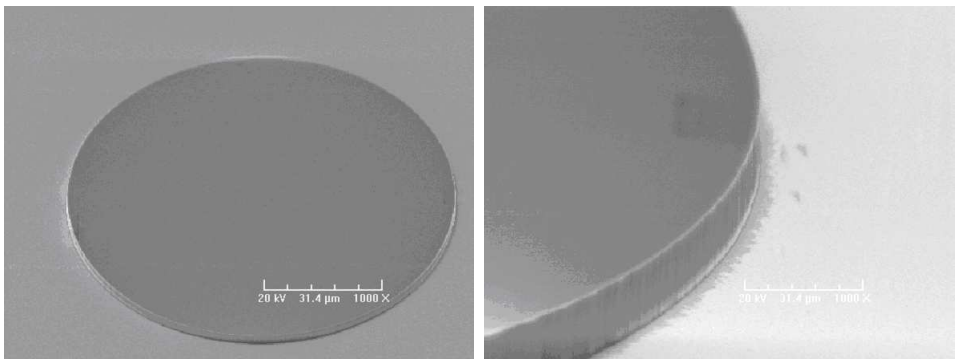

(a) (b)

Figure 5.5: SEM images of dry etched disks: (a) Top view showing the dry-etched disk and (b) zoomed view showing the edge roughness of a dry-etched disk.

the disks in the middle part of the wafer is less than when compared to that of the disks at the side of the wafer. Since the aim is to couple light into the disks at their thinnest point, the irregularity of the pedestal should not be a crucial issue.

Scanning Electron Microscope Imaging

The SEM images of single disks with an under-etched pedestal of 50 μm are shown in Fig. 5.7 below. As mentioned earlier, the main aim of the project was to concentrate on improving the smoothness and surface finish of the disks, since this is a key requirement to achieving a good Q-factor. In order to achieve this, xenon fluoride (XeF-2) etching was tried.

Comparison of Etching Processes

In order to perform the dry isotropic etching by XeF_2, a wafer with a sample of disks was sent to the company, MEMSStar (UK). A comparison between the Tyndall-etched disks with MEMSStar-etched disks is made. Note that SEM imaging was used for all

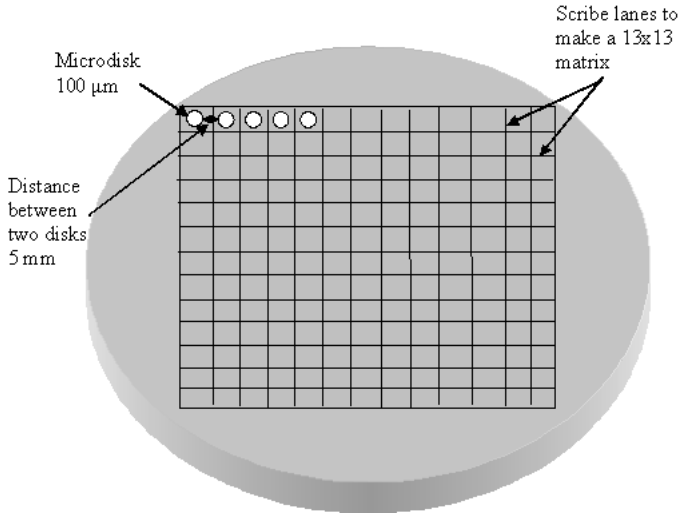

Figure 5.6: Schematic diagram illustrating the layout for the wafer configuration with single microdisks

the disks. As one can see from the rim images of the MEMStar-etched disks, shown in Figs. 5.8(a) and 5.9(a), the photoresist cap on the oxide of the xenon fluoride, XeF_2 pillars was not taken off. However, for the SEM images, this is not really necessary, since only the rim and shape of the pillar is being considered, not the top of the disk. In comparison, the photoresist for the plasma etch must be removed (c.f. Fig. 5.7), since the plasma etch can also etch the resist and particles from the resist can subsequently redeposit on the SiO_2 surface, creating a very dirty looking etch. Fig. 5.8 is the first XeF_2 etch in which the loading effect is very visible. This is a pedestal on which SiO_2 disk rests. At this disk, there is a low underetch. Other pillars at the outer part of the Si-wafer have been etched more. The loading effect is even visible near the pillars. There is more etching under the pillars than in the field and this is opposite to the effect obtained using the plasma etches. The etch is very smooth. Fig. 5.9 was the second etch, which was performed at a lower pressure. This is the

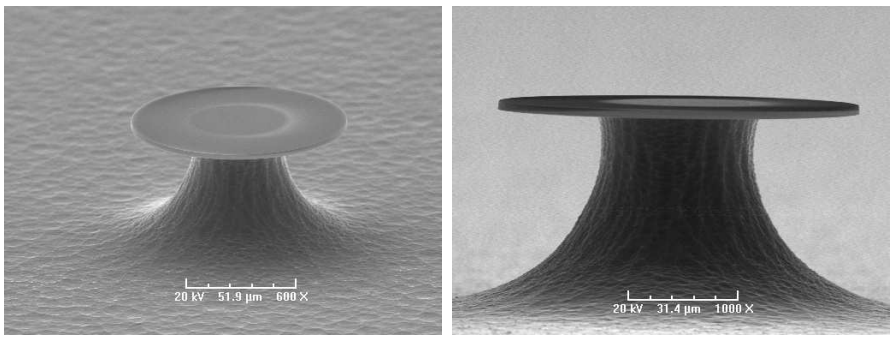

(a) (b)

Figure 5.7: SEM images of dry-etched disks. The images show disks of 2 μm thickness and an underetched pedestal of 50 μm.

most isotropic etch obtained, yet with the roughest SiO_2 surface. Plasma-etching was done for identical (test) wafers (c.f. Figs. 5.10 and 5.11). These pillars are very smooth; however, the etch rate downward is higher than the etch rate to the sides and it is less isotropic. This is as one would expect with a plasma etch since it is directional. Unfortunately, there is no visible difference in the surface roughness of the rims in Figs. 5.10(a) and 5.11(a).

5.3.2 Configuration II: Multiple disks with constant spacing

Fig. 5.12 shows the schematic of the configuration of multiple planar silica disks which were fabricated as part of the NAP112 project. The gap between neighbouring disks in each group is 5 μm and the scribe lanes were drawn at 5 mm distance. As explained earlier, these scribe lanes are useful in separating the disks inside each box and, thereby, facilitate easy coupling of pump light into the disks when using a tapered optical fibre. The SEM images of these disks are shown in Figs. 5.13 and 5.14. When working with these disks the idea is that a tapered optical fibre will pass

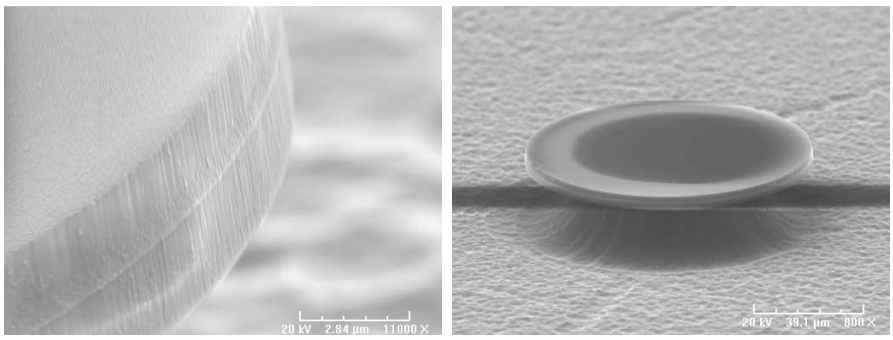

(a) (b)

Figure 5.8: SEM images of XeF_2 etched disks.

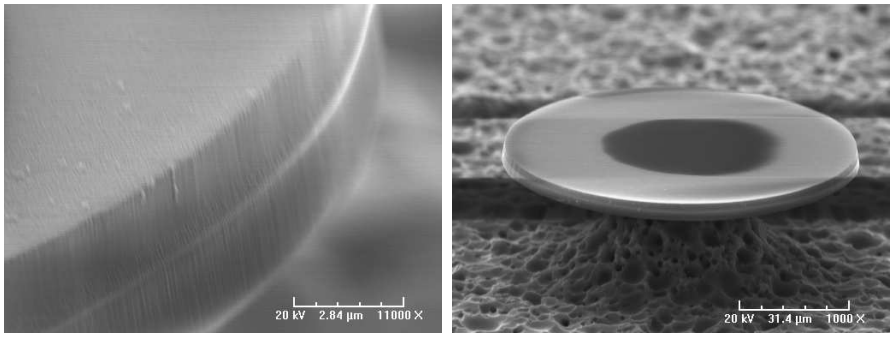

(a) (b)

Figure 5.9: SEM images of XeF_2 etched disks at lower pressure.

between neighboring disks, thereby coupling light into both disks simultaneously.

5.3.3 Configuration III: Multiple disks with varying distances

Configuration III contains four divisions on the substrate (c.f. Fig. 5.15). Division 1 comprises of two disk arrays (c.f. Fig.5.16(a)), each disk having a diameter of 100 μm and with a gap of 5 μm between neighbouring disks, whereas division 2 consists of three disks per array (c.f. Fig.5.16(a)) with the same gap between the neighbours. The disk arrangement in divisions 3 and 4 is shown in Fig. 5.17. As an example, the

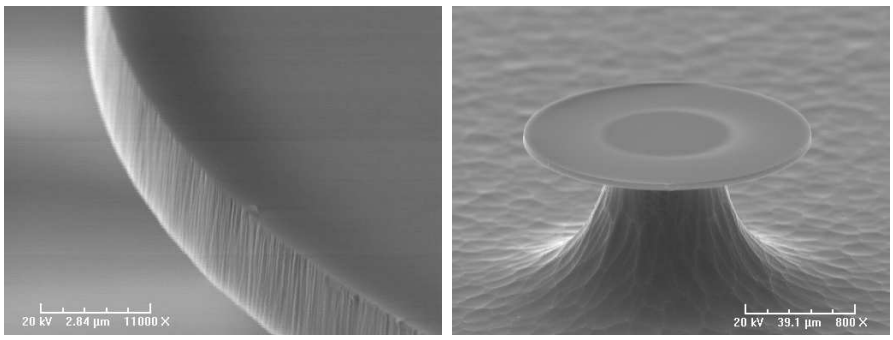

(a) (b)

Figure 5.10: SEM images of plasma-etched disks.

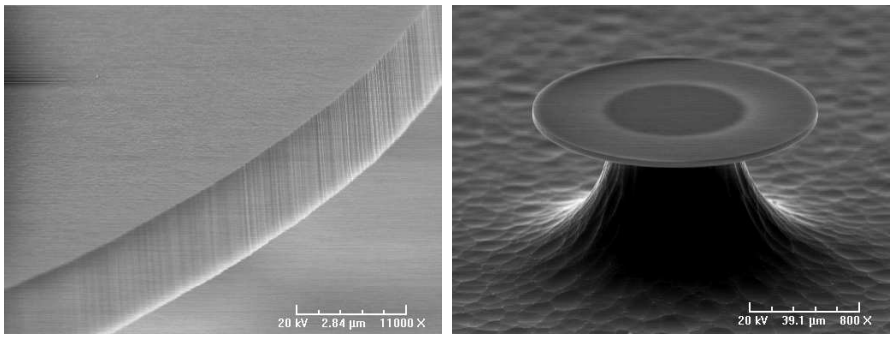

(a) (b)

Figure 5.11: SEM images of plasma-etched disks at lower pressure.

SEM images of the varying distances between the disks are shown in Fig. 5.18.

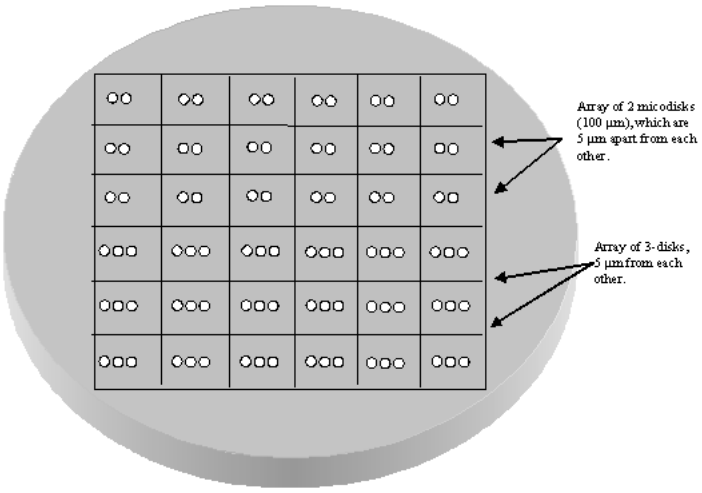

Figure 5.12: Configuration II: An array of multiple disks

5.4 Experimental Considerations

The Q-factor of the microdisks can be measured by coupling narrow linewidth laser light into a microdisk via the evanescent field of a tapered optical fibre as shown in Fig. 5.19. By analysing the width of the resulting optical resonances excited within the microcavity, an estimation of the Q-factor can be made. The laser linewidth should be of the order of few kHz and the wavelength must be tunable over a wide range, typically 5-10 nm, in order to observe cavity resonances. If the laser does not have a large tuning range, once can tune the cavity by heating it, thereby ensuring that the cavity mode is resonant with the laser wavelength. Unfortunately, the Q-factor of these devices was not measured as part of this project and, therefore, no comment can be made about their suitability for future experiments.

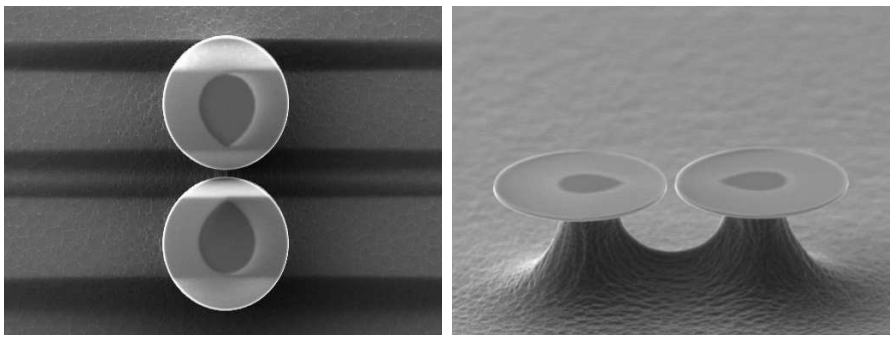

(a) (b)

Figure 5.13: Top and side SEM images of the two disk configuration for the Tyndall etched disks.

5.5 Future Prospects

Microcavity disks, with 100 μm diameter and of varying separation, have been fabricated using Tyndall National Institute's microfabrication facilities through the National Access Programme. SEM images of the disks are promising, since they appear to be smooth and relatively uniform. Of the two different etching methods used, dry-etching technique gives the more favourable results. The next step in this work will be to measure and, subsequently, improve the Q-factors of the microcavities. A very high Q-factor is crucial for any experiments in the domain of quantum electrodynamics, where strong coupling between an atom and the cavity mode is required. In addition, microtoroids may be more favourable than microdisks since they provide stronger confinement of the whispering gallery modes in the cavity, leading to a higher Q-factor in general. For this, a CO2 laser would be used. By heating the centre of the SiO_2 disk, one achieves a smooth surface, as explained in the ref. [82]. This is called selective reflow process. These toroidal microdisks exhibit an increase

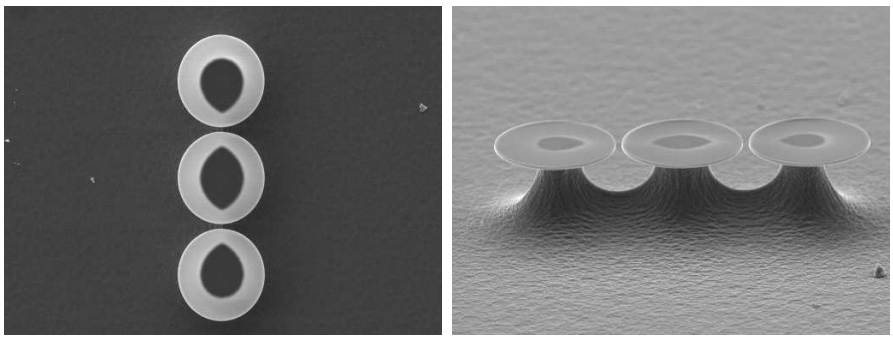

(a) (b)

Figure 5.14: Top and side SEM images of the three disk configuration for the Tyndall etched disks.

in Q-factor by four orders of magnitude. Another step to increase the Q-factor is by doping techniques. For example, using erbium as a dopant with SiO_2, higher Q-values of $> 10^8$ is achievable.

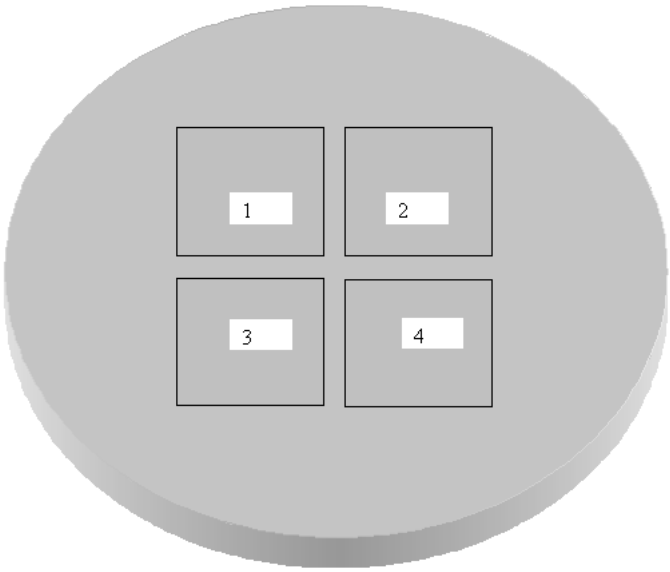

Figure 5.15: Schematic of configuration III: Multiple disks with varying distances.

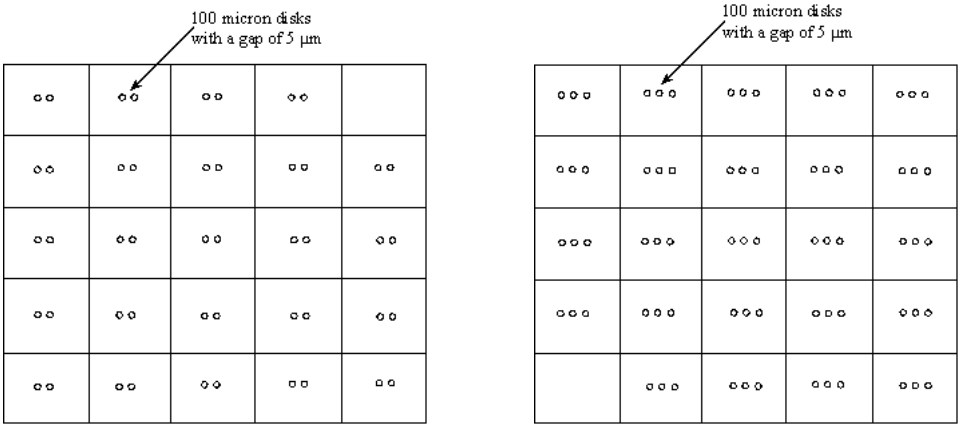

(a) (b)

Figure 5.16: The disk arrangement for (a) division 1 and (b) division 2 in Fig. 5.15.

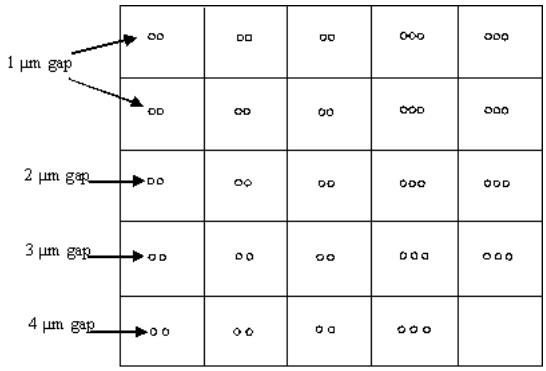

Figure 5.17: The disk arrangement for divisions 3 and 4 in Fig. 5.15.

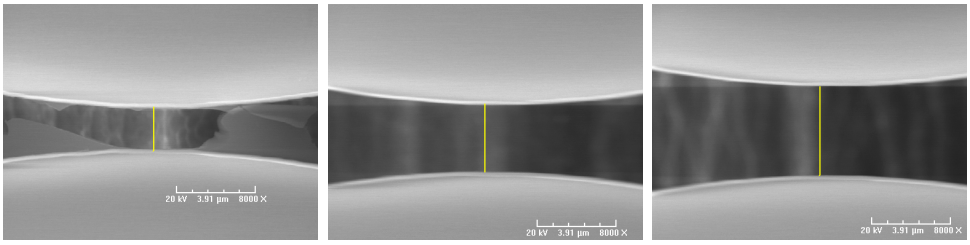

(a) (b) (c)

Figure 5.18: SEM images of configuration III showing the varying distances between the disks: (a) 2 μm gap, (b) 3 μm gap and (c) 4 μm gap.

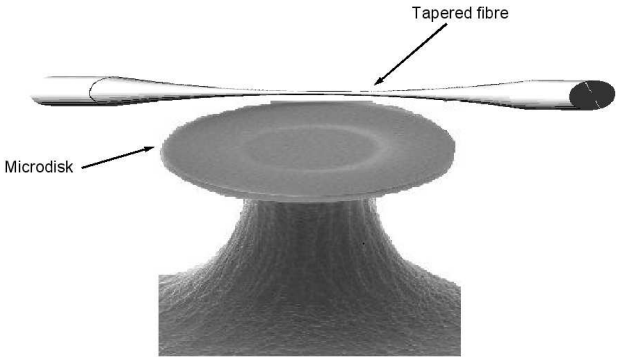

Figure 5.19: Schematic of the photon coupling scheme from a tapered optical fibre into a microdisk.

Conclusions

There are many different trapping mechanisms to manipulate cold, neutral atoms. This thesis explains two important schemes by which one can trap and manipulate cold atoms with applications in quantum technologies. Also, the experimental advancements towards the study of the interaction of light with cold atoms has been discussed. These experiments concentrated on the determination of suitable detectors for cold atoms + photon interaction experiments, where it is essential to have a good detection mechanisim. To get information of atom interactions with the evanescent field, photon detectors are employed. In the future, these experiments will lead to atom+surface effect measurements such as Casimir-Polder and van der Waals force measurements. This thesis also gave an introduction to the use of microtechnology to fabricate microdisks, which could be implemented in the field of cold atoms to perform cavity QED experiments and quantum information processing by using the concept of entanglement.

A brief history on developments towards the achievement of *cold atoms* was reviewed. Cold atoms are typically in the range of temperatures one million times colder than that of the room temperature. The principle behind Doppler cooling, which has a dependance on detuning of the laser frequency was explained. Taking rubidium (^{85}Rb) as an atom for cooling, typical values of attainable Doppler temperature were

shown, which is $\sim 150\ \mu$K. The technique of *optical molasses* to achieve a 3D-optical molasses was explained briefly. After achieving this step it is the addition of a zero magnetic field region that is responsible for trapping the atoms in the confined region of space. This is called the magneto-optical trap (MOT).

A theoretical discussion on trapping cold atoms using a tapered optical fibre was given in Chapter 2. The evanescent field around a tapered optical fibre was calculated for different thicknesses of fibre tapering. It is worthwhile to note that the tapering is in the submicron range. The evanescent field extension around the tapered fibre varies inversely with the thickness of the tapering. A natural consequence of the existence of the van der Waals force on the atom in the close proximity of the fibre surface was discussed. Finally, it was shown that by using these tapered optical fibres, it is possible to create a trapping potential using red-detuned light in the fibre. A disadvantage of this method, that is worth noting here, is that the depth of the traps strongly depends on the input laser power. However, recent measurements show that it should be feasible to transmit up to 500 mW into tapered fibres in UHV without meltdown occuring. An alternative scenario would be to modulate the input laser power into the optical fibre, thereby reducing the effective intensity on the tapered part per second.

Chapter 3 is another theoretical discussion, which is based on a novel technique of trapping cold atoms by a diffracted field of a red-detuned laser. Here, near-field Fresnel diffraction in circular apertures was considered to create the trapping potentials. The circular apertures considered are of a size exceeding the optical wavelength. The field distribution in the vicinity of these circular apertures in a thin screen was analysed at different distances. This gave an idea of the trapping distance for the cold

atoms from the surface. As these distances are in the order of microns, the influence of the van der Waals force and Casimir Polder forces are negligible, and hence have been neglected in the calculations. Also, the parameters for rubidium and caesium cold atoms in the trapping potentials were calculated and discussed. This method of trapping cold atoms has an advantage to perform site selective manipulation, and in quantum information processing.

After the theoretical chapters, Chapter 4 focussed on experimental work. Mainly the possibility to use the detectors in cold atoms experiments was considered. These experiments were performed in the view of light-matter interactions. A technique of coupling light into single mode fibres (SMFs) is an essential and important task, yet it is a time consuming and tedious one. Therefore, a coupling mechanism that was adopted for efficient coupling into SMFs was discussed in this chapter. An APD, which was fabricated in Tyndall National Institute was characterised. Basic circuits to bias the APD, and to nullify the noise output were explained. A brief overview of single photon detectors was also given. Advancement in these solid state devices has become an important back bone in the field of detector technology. The idea behind the need for single photon detectors has been made clear. This is due to the fact that when cold atoms interact with the evanescent field from a tapered optical fibre, there are very few number of photons involved in the interaction.

In the last Chapter, the fabrication of WGM microcavities was discussed. Comparison of dry- and wet- etching fabrication techniques by taking SEM images was done. This comparision helped to choose the right kind of etching technique to get a smooth surface for microdisks. Also, SEM images of different configurations of these microdisks were discussed. An experimental idea to measure the Q-factor of these

disks was explained. Strong coupling between individual atoms and the WGM of microtoroids is possible. By this the interactions near the surface of the resonator are determined by observing transit events for single atoms falling through the evanescent field.

To summarise, we have learnt how atoms can be cooled using lasers, how to trap them, how to detect the low light levels of the atom interaction with the light and how to fabricte WGM disks, which can be used in cold atoms experiments.

A future prospect of the use of these disks would be in our cold atom setup. Also, improving the Q-factor of the disks would be crucial. By doping the disks with erbium they would be made active i.e. pumping with 980 nm laser would produce emissions at 1.5 μm. It is also possible to study strong coupling between photons stored in the microcavity with cold Rb atoms in a MOT. In principle, this could be done by coupling the photons into the cavity by using tapered optical fibre. These photons, in turn, can be coupled to the cold atoms for cavity QED studies. One may also be able to perform entanglement experiments, thereby paving the way to a better understanding of cavity + atom systems for quantum logic.

Bibliography

[1] M. H. Anderson, J. R. Ensher, M. R. Matthews, C. E. Wieman, and E. A. Cornell, *Science* **269**, 198 (1995).

[2] A. Peters, K. Y. Chung, B. C. Young, J. M. Hensley, and S. Chu, *Phil. Trans. R. Soc. Lond. A* **355**, 2223 (1997).

[3] W. Buell, B. Jaduszliwer, Frequency and Time Forum, 1999 and the IEEE International Frequency Control Symposium, 1999, *Proceedings of the 1999 Joint Meeting of the European Frequency andTime Forum and the IEEE International Frequency Control Symposium* **1**, 85 (1999).

[4] W. Williams and M. Saffman, *J. Opt. Soc. Am. B* **23**, 1161 (2006).

[5] J. J. García-Ripoll, P, Zoller, and J. I. Cirac, *J. Phys. B: At. Mol. Opt. Phys.* **38** 567 (2005).

[6] S. Chu, *Rev. of Mod. Phys.* **70**, 685 (1998).

[7] I. H. Deutsch, G. K. Brennen, and P. S. Jessen, *Special issue of special issue of Quant. Inf. Proc.* **15**, 3 (2004).

[8] S. Groth, P. Krueger, S. Wildermuth, R. Folman, T. Fernholz, J. Schmiedmayer, D. Mahalu and I. Bar-Joseph, *Appl. Phys. Lett.* **85**, 2980 (2004).

[9] S. J. Van Enk, H. J. Kimble, and H. Mabuchi, "Quantum Information Processing in Cavity-QED", Volume 3 , *Kluwer Academic Publishers Hingham*, MA, USA (2004).

[10] A. J. Miller, S. W. Nam, J. M. Martinis, and A. V. Sergienko, *Appl. Phys. Lett.* **83**, 791 (2003).

[11] M. Mitsunaga, T. Mukai, K. Watanabe, and T. Mukai, *J. Opt. Soc. Am. B*, **13**, 12 (1996).

[12] P. Thomann, M. Plimmer, G. Di Domenico, N. Castagna, J. Guena, G. Dudle and F. Fzesi, *Appl. Phys. B*, **84**, 659 (2006).

[13] T. Hänsch and A. Schawlow, *Opt. Commun.* **13**, 68 (1975).

[14] V. G. Minogin, and V. S. Letokhov, "Laser light pressure on atoms", *Moscow: Nauka*, 1986, translated into English, *New York: Gordon and Breach*, 1987.

[15] A. L. Migdall, J. V. Prodan, and W. D. Phillips, *Phys. Rev. Lett.* **54**, 2596 (1985)

[16] S. Chu, L. Hollberg, J. E. Bjorkholm, A. Cable and A. Ashkin, *Phys. Rev. Lett.* **55**, 48 (1985).

[17] A. Ashkin, *Phys. Rev. Lett.* **40**, 729 (1978).

[18] E. L. Raab, M. Prentiss, A. Cable, S. Chu, and D. E. Pritchard, *Phys. Rev. Lett.* **59**, 2631 (1987).

[19] P. Lett, R. Watts, C. Westbrook, W. Philips, P. Gould, and H. Metcalf, *Phys. Rev. Lett.* **61**, 169 (1988).

[20] J. Dalibard and C. Cohen-Tannoudji, *J. Opt. Soc. Am. B*, **6**, 2023 (1989).

[21] K. B. Davis, M.-O. Mewes, M. R. Andrews, N. J. van Druten, D. S. Durfee, D. M. Kurn, and W. Ketterle, *Phys. Rev. Lett.* **75**, 3969 (1995).

[22] C. C. Bradley, C. A. Sackett, J. J. Tollett, and R. G. Hulet, *Phys. Rev. Lett.* **75**, 1687 (1995).

[23] H. J. Metcalf and P. van der Straten, *Laser Cooling and Trapping*, Springer-Verlag, 1999.

[24] S. Stenholm, *Rev. Mod. Phys.* **58**, 699 (1986).

[25] A. Aspect, J. Dalibard, A. Heidmann, C. Salomon, and C. Cohen-Tannoudji, *Phys. Rev. Lett.* **57**, 1688 (1986).

[26] C. Monroe, W. Swann, H. Robinson and C. Weimann, *Phys. Rev. Lett.* **65**, 1571 (1990).

[27] M. Prentiss, A. Cable, J. Bjorkholm, S. Chu, E. Raab and D. Pritchard, *Opt. Lett.* **13**, 452 (1998).

[28] E. Riis, D. Weiss, K. Moler and S. Chu, *Phys. Rev. Lett.* **64**, 1658 (1990).

[29] J. Nellessen, J. Werner, and W. Ertmer, *Opt. Commun.* **78**, 300 (1990).

[30] J. Denschlang, D. Cassettari, and J. Schmiedmayer, *Phys. Rev. Lett.* **82**, 2014 (1999).

[31] M. J. Renn, D. Montgomery, O. Vdovin, D. Z. Anderson, C. E. Wieman, and E. A. Cornell, *Phys. Rev. Lett.* **75**, 3253 (1995).

[32] F. LeKien, V. I. Balykin, and K. Hakuta, *Phys. Rev. A* **70**, 063403 (2004).

[33] V. I Balykin, K. Hakuta, F. Le Kien, J. Q. Liang, and M. Morinaga, *Phys. Rev. A* **70**, 011401(R) (2004).

[34] J. Ward, D. OShea, B. Shortt, M. Morrissey, K. Deasy and S. Nic Chormaic, *Rev. Sci.Instrum.* **77**, 083105 (2006).

[35] L. Tong, R. R. Gattass, J. B. Ashcom, S. He, J. Lou, M. Shen, I. Maxwell, and E. Mazur, *Nature* **426**, 816 (2003).

[36] J. M. Ward, D. G. O'Shea, B. J. Shortt, M. J. Morrissey, K. Deasy and S. Nic Chormaic, *Rev. Sci. Instrum.* **77**, 083105 (2006).

[37] R. J. Cook and R. K. Hill, *Opt. Comm.* **43**, 258 (1982).

[38] H. Perrin, Y. Colombe, B. Mercier, V. Lorent and C. Henkel, *Journal of Physics: Conference Series* **19**, 151 (2005).

[39] S. Feron, J. Reinhardt, M. Ducloy, O. Gorceix, S. Nic Chormaic, Ch. Miniatura, J. Robert, J. Baudon, and V. Lorent, Phys. Rev. A **49**, 4733 (1994).

[40] V. I. Balykin, V. S. Letokhov, Yu. B. Ovchinnikov, and A. I. Sidorov, *Phys. Rev. Lett.* **60**, 2137 (1988).

[41] J. P. Dowling and J. Gea-Banacloche, *Adv. At. Mol. Opt. Phys.* **37**, 1 (1996).

[42] E. A. Hinds and I. G. Hughes, *J. Phys. D: Appl. Phys.* **32**, 119 (1999).

[43] H. Ito, T. Nakata, K. Sakaki, and M. Ohtsu, *Phys. Rev. Lett.* **76**, 4500 (1996).

[44] H. Ito, K. Sakaki, M. Ohtsu, and W. Jhe, *App. Phys. Lett.* **70**, 2496 (1997).

[45] M. J. Renn, D. Montgomery, O. Vdovin, D. Z. Anderson, C. E. Wieman, and E. A. Cornell, *Phys. Rev. Lett.* **75**, 18 (1995).

[46] J. C. Knight, G. Cheung, F. Jacques, and T. A. Birks, *Opt. Lett.* **22**, 1129 (1997).

[47] A. H. Barnett, "Dissipation in Deforming Chaotic Billiards", *Ph.D. thesis - Chapter8*, Harvard University, 2000.

[48] F. Le Kien, S. D. Gupta, V. I. Balykin, and K. Hakuta, *Phys. Rev. A* **72**, 063815 (2005).

[49] K. P. Nayak, P. N. Melentiev, M. Morinaga, F. Le Kien, V. I. Balykin, and K. Hakuta, *Opt. Express* **15**, 5431 (2007).

[50] F. Le Kien and K. Hakuta, *Phys. Rev. A* **77**, 033826 (2008).

[51] P. Domokos, P. Horak, and H. Ritsch, *Phys. Rev. A* **65**, 033832 (2002).

[52] F. Le Kien, J. Q. Liang, K. Hakuta, and V. I. Balykin, *Opt. Commun.* **242**, 445 (2004).

[53] F. Le Kien, S. Dutta Gupta, V. I. Balykin, and K. Hakuta, *Phys. Rev. A* **72**, 032509 (2005).

[54] F. Le Kien, V. I. Balykin, and K. Hakuta, *Phys. Rev. A* **73**, 013819 (2006).

[55] P. W. Milonni and J. H. Eberly, *Lasers*, Wiley-Interscience, New York, 1988.

[56] F. Le Kien, V. I. Balykin, and K. Hakuta, *Phys. Rev. A* **73**, 053823 (2006).

[57] U. D. Rapol, A. Wasan, and V. Natarajan, *Europhys. Lett.* **61**, 53 (2003).

[58] W. R. Johnson, V. A. Dzuba, and U. I. Safranova, *Phys. Rev. A* **69**, 022508 (2004).

[59] M. Chevrollier, D. Bloch, G. Rahmat, and M. Ducloy, *Opt. Lett.* **16**, 1879 (1991).

[60] V. I. Balykin, V. S. Letokhov, and V. G. Minogin, *Phys. Scr.* **22**, 119 (1988).

[61] V. I. Balykin and V. S. Letokhov, *JETP* **67**, 78 (1988).

[62] W. Hänsel, P. Hommelhoff, T. W. Hänsch and J. Reichel, *Nature* **413**, 498 (2001).

[63] K. D. Nelson, Xiao Li, and D. S. Weiss, *Nat. Phys.* **645**, 556 (2007).

[64] S. K. Sekatskii, B. Riedo, and G. Dietler, *Opt. Comm.* **195**, 197 (2001).

[65] J. L. Cohen, B. Dubetsky, and P. R. Berman, *Phys. Rev. A* **60**, 4886 (1999).

[66] G. Birkl, F. B. J. Buchkremer, R. Dumke, and W. Ertmer, *Opt. Commun.* **191**, 67 (2001).

[67] V. I. Balykin and V. G. Minogin, *Phys. Rev. A* **77**, 013601 (2008).

[68] J. I. Cirac and P. Zoller, *Phys. Rev. Lett.* **74**, 4091 (1995).

[69] F. Schmidt-Kaler, H. Häffner, M. Riebe, S. Gulde, G. P. T. Lancaster, T. Deuschle, C. Becher, C. F. Roos, J. Eschner, and R. Blatt, *Nature* **422**, 408 (2003).

[70] R. L. Lucke, *Eur. J. Phys.* **27**, 193 (2006).

[71] V. I. Balykin and V. G. Minogin, *JETP* **105**, 479 (2007).

[72] S. Nic Chormaic, A. Yarovitskiy, B. Shortt, K. Deasy and M. Morrissey, *Proc. SPIE* **5826**, 83, Opto-Ireland (2005).

[73] T. Aoki, B. Dayan, E. Wilcut, W. P. Bowen, A. S. Parkins, T. J. Kippenberg, K. J. Vahala and H. J. Kimble, *Nature* **443**, 671 (2006).

[74] M. Aspelmeyer, *Nature Photonics* **1**, 94 (2007).

[75] S. Nußmann, M. Hijlkema, B. Weber, F. Rohde, G. Rempe and A. Kuhn, *Phys. Rev. Lett.* **95**, 173602 (2005).

[76] M. Hijlkema, B. Weber, H. Specht, S. C. Webster, A. Kuhn and G. Rempe, *Nature Phys.* **3**, 253 (2007).

[77] T. Wilk, S. C. Webster, H. P. Specht, G. Rempe and A. Kuhn, *Phys. Rev. Lett.* **98**, 063601 (2007).

[78] S. M. Spillane, T. J. Kippenberg, K. J. Vahala, K. W. Goh, E. Wilcut, and H. J. Kimble, *Phys. Rev. A* **71**, 013817 (2005).

[79] L. Noirie, *The Optical Fiber Communication Conference and Exposition (OFC)* **2**, 615 (2003).

[80] K. J. Vahala, *Nature* **424**, 839 (2003).

[81] M. H. Zadeh and K. J. Vahala, *Opt. Express.* **15**, 166 (2007).

[82] D. K. Armani, T. J. Kippenberg, S. M. Spillane, and K. J. Vahala, *Nature* **421**, 925 (2003).

APPENDIX A

Matlab programs for Chapter 2: Fibre trapping of cold atoms

This matlab program is used to calculate/plot the total potential for the atom (c. f. Fig.2.5), which clearly depends on the detuning of the laser light and the input beam intensity.

```
% van der Waals potential calculations :
   clc;
clear all;
r = 0.2 : 1 e - 3 : 5; C = 0.78 e3;
V = - (C. / (r - 0.2). ^3);
theta_rec = 888; W = (V. / theta_rec);

% Optical Potential Calculations : lambda = 1.3; k = (2 * pi). / lambda;
g = 5330; % g is the normalised coupling constant
a = 0.2; LAMBDA = 2.42;
q = 1. / LAMBDA;

for m = 230; % m is an integer called orbital angular momentum
U1 = (((m. ^2 - 0.25). / (k^2. * r. ^2)) - (g. * besselk (0, q. * r). ^2));

U_tot1 = W + U1;

plot (r, (U_tot1. * 888. * 4.8 e - 11). / 1 e - 3); xlim ([0.2, 3]);
ylim ([-0.4, 0.2]); hold on; grid on;
xlabel (' distance from the fibre surface, r \mum '); ylabel (' U_t _o _t in mK ');
end
```

Another program, which can plot the potential for m-values is written below. An example graph, which can be plotted using the below code can be seen in Fig. 2.11.

```
% van der Waals potential calculations
clc;
clear all;
r = 0.3 : 1 e - 3 : 5;
C = 3 e3;
V = - (C. / (r - 0.3). ^3);
theta_rec = 970;
W = (V. / theta_rec);

% Optical Potential Calculations
lambda = 1.55;
k = (2 * pi). / lambda;
g = 8135;
a = 0.3;
LAMBDA = 2.88;
q = 1. / LAMBDA;

% Total potential for a range of m - values #
for
m = 260 : 10 : 500;
U1 = (((m. ^2 - 0.25). / (k^2. * r. ^2)) - (g. * besselk (0, q. * r). ^2));

U_tot1 = W + U1;

plot (r, (U_tot1. * 970. * 4.8 e - 11). / 1 e - 3);
xlim ([0, 5]); ylim ([-0.4, 0.27]); hold on; % grid on;
end
xlabel (' distance from fibre surface, r (\mum) '); ylabel (' U_t _o _t, (mK) ');
```

To find the recoil angle for Rubidium (^{85}Rb).

```
% To find Theta_rec %%%%%%%%

h = 6.6 e - 34;
lambda = 1.55 e - 6;
Mass = 1.4 e - 25;

Theta_rec = ((h. / lambda). ^2). / (2. * Mass);
% To convert into Kelvin scale
theta = Theta_rec. / (1.6 e - 19. * 4.1 e - 15)
```

APPENDIX B

Mathematica programs for chapter3: Diffraction traps for cold atoms

This program is used to plot the 3D-surface-plot of the trapping potential created by the diffracted field. Later, saved files were loaded in origin and plotted to get the graphs as shown in Fig. 3.3.

```
b = 2 Pi a;
r[ρ_, z_, ξ_, φ_] := Sqrt[z^2 + ρ^2 + ξ^2 - 2 ρ ξ Cos[φ]];
integrandreal[a_, ρ_, z_, ξ_, φ_] := z ξ / r[ρ, z, ξ, φ]^2
    (1 / r[ρ, z, ξ, φ] Cos[2 Pi a r[ρ, z, ξ, φ]] - 2 Pi a Sin[2 Pi a r[ρ, z, ξ, φ]]);
integrandimaginary[a_, ρ_, z_, ξ_, φ_] := z ξ / r[ρ, z, ξ, φ]^2
    (1 / r[ρ, z, ξ, φ] Sin[2 Pi a r[ρ, z, ξ, φ]] + 2 Pi a Cos[2 Pi a r[ρ, z, ξ, φ]]) ;
efieldreal[a_, ρ_, z_] := 1 / (2 Pi) NIntegrate[integrandreal[a, ρ, z, ξ, φ],
    {ξ, 0, 1}, {φ, 0, 2 Pi}, Method → Automatic, MinRecursion → 5];
efieldimaginary[a_, ρ_, z_] := 1 / (2 Pi) NIntegrate[integrandimaginary[a, ρ, z, ξ, φ],
    {ξ, 0, 1}, {φ, 0, 2 Pi}, Method → Automatic, MinRecursion → 5];
w[a_, ρ_, z_] := -efieldreal[a, ρ, z]^2 - efieldimaginary[a, ρ, z]^2;

(Table[w[1.5, ρ, 0.5], {ρ, -1.3, 1.3, .01}];
 wtranslista = Table[w[1.5, ρ, 0.5], {ρ, -1.3, 1.3, .01}];
ListPlot[wtranslista, PlotRange → All])

rholist = Table[ρ, {ρ, -1.3, 1.3, .01}];
Export["c:\\wtranslista.dat", Transpose[{rholist, wtranslista}], "Table"]
```

```
(Table[w[1.5, ρ, 1], {ρ, -1.3, 1.3, .01}];
 wtranslistb = Table[w[1.5, ρ, 1], {ρ, -1.3, 1.3, .01}];
ListPlot[wtranslistb, PlotRange → All])

rholist = Table[ρ, {ρ, -1.3, 1.3, .01}];
Export["c:\\wtranslistb.dat", Transpose[{rholist, wtranslistb}], "Table"]


(Table[w[1.5, ρ, 5], {ρ, -1.3, 1.3, .01}];
 wtranslistc = Table[w[1.5, ρ, 5], {ρ, -1.3, 1.3, .01}];
ListPlot[wtranslistc, PlotRange → All])

rholist = Table[ρ, {ρ, -1.3, 1.3, .01}];
Export["c:\\wtranslistc.dat", Transpose[{rholist, wtranslistc}], "Table"]
```

The program written below is to plot the 3D-surface-plot of the Fresnel number as explained in Fig. 3.5.

```
<< Graphics`SurfaceOfRevolution`
<< Graphics`Graphics3D`
Off[General::spell1]

b = 2 Pi a;
r[ρ_, z_, ξ_, φ_] := Sqrt[z^2 + ρ^2 + ξ^2 - 2 ρ ξ Cos[φ]];
integrandreal[a_, ρ_, z_, ξ_, φ_] := z ξ / r[ρ, z, ξ, φ]^2
    (1 / r[ρ, z, ξ, φ] Cos[2 Pi a r[ρ, z, ξ, φ]] - 2 Pi a Sin[2 Pi a r[ρ, z, ξ, φ]]);
integrandimaginary[a_, ρ_, z_, ξ_, φ_] := z ξ / r[ρ, z, ξ, φ]^2
    (1 / r[ρ, z, ξ, φ] Sin[2 Pi a r[ρ, z, ξ, φ]] + 2 Pi a Cos[2 Pi a r[ρ, z, ξ, φ]]) ;
efieldreal[a_, ρ_, z_] := 1 / (2 Pi) NIntegrate[integrandreal[a, ρ, z, ξ, φ],
    {ξ, 0, 1}, {φ, 0, 2 Pi}, Method → Automatic, MinRecursion → 5];
efieldimaginary[a_, ρ_, z_] := 1 / (2 Pi) NIntegrate[integrandimaginary[a, ρ, z, ξ, φ],
    {ξ, 0, 1}, {φ, 0, 2 Pi}, Method → Automatic, MinRecursion → 5];
w[a_, ρ_, z_] := -efieldreal[a, ρ, z]^2 - efieldimaginary[a, ρ, z]^2;

ρstep = 0.01;
ρstart = 0;
ρend = 2;
```

```
(Table[w[5, ρ, 0.5], {ρ, ρstart, ρend, ρstep}];
 Ua1 = Table[w[5, ρ, 0.5], {ρ, ρstart, ρend, ρstep}];
ListPlot[Ua1, PlotRange → All];)

(Table[w[1.5, ρ, 1], {ρ, ρstart, ρend, ρstep}];
 Ub1 = Table[w[1.5, ρ, 1], {ρ, ρstart, ρend, ρstep}];
 ListPlot[Ub1, PlotRange → All];)


(Table[w[1.5, ρ, 5], {ρ, ρstart, ρend, ρstep}];
 Uc1 = Table[w[1.5, ρ, 5], {ρ, ρstart, ρend, ρstep}];
 ListPlot[Uc1, PlotRange → All];)

Mk3D[U2D_] := {
    tmp1 = Table[{(i - 1)/Length[U2D], U2D[[i]]}, {i, 1, Length[U2D]}];
    polTable1 = Table[
      Table[{tmp1[[j, 1]], tmp1[[j, 2]], α}, {j, 1, Length[tmp1]}], {α, 0, 2 π, 0.1}];
    polTable1 = Flatten[polTable1, 1];
    CortTable1 = Table[{polTable1[[i, 1]] Cos[polTable1[[i, 3]]], polTable1[[i, 1]]
         Sin[polTable1[[i, 3]]], polTable1[[i, 2]]}, {i, 1, Length[polTable1]}] // N
   }[[1]];

Ua3D = Mk3D[Ua1];
Ub3D = Mk3D[Ub1];
Uc3D = Mk3D[Uc1];



scatterplot3d[Ua3D]

"c:\\Uc.dat"


ScatterPlot3D[Ua3D];


Export["c:\\Uc.dat", Uc3D];



tmp2 = Table[{i/Length[Ub], Ub[[i]]}, {i, 1, (Length[Ub] + 1)/2}];
polTable2 = Table[
   Table[{tmp2[[j, 1]], tmp2[[j, 2]], α}, {j, 1, Length[tmp2]}], {α, 0, 2 π, 0.1}];
polTable2 = Flatten[polTable2, 1];
CortTable2 = Table[{polTable2[[i, 1]] Cos[polTable2[[i, 3]]], polTable2[[i, 1]]
      Sin[polTable2[[i, 3]]], polTable2[[i, 2]]}, {i, 1, Length[polTable2]}] // N;

Export["c:\\fresnel_b.dat", CortTable2];


tmp3 = Table[{i/Length[U_c], U_c[[i]]}, {i, 1, (Length[U_c] + 1)/2}];
polTable3 = Table[
   Table[{tmp3[[j, 1]], tmp3[[j, 2]], α}, {j, 1, Length[tmp3]}], {α, 0, 2 π, 0.1}];
polTable3 = Flatten[polTable3, 1];
CortTable3 = Table[{polTable3[[i, 1]] Cos[polTable3[[i, 3]]], polTable3[[i, 1]]
      Sin[polTable3[[i, 3]]], polTable3[[i, 2]]}, {i, 1, Length[polTable3]}] // N;

Export["c:\\fresnel_c.dat", CortTable3];
```

APPENDIX C

This appendix shows a published paper in Phys. Rev. A., based on the results from Chapter 3. In order to show the paper in full size, it is intentionally started from next page.

Atom microtraps based on near-field Fresnel diffraction

Thejesh N. Bandi,[1,2] Vladimir G. Minogin,[1,2,3] and Síle Nic Chormaic[2,4,*]
[1]*Department of Applied Physics and Instrumentation, Cork Institute of Technology, Bishopstown, Cork, Ireland*
[2]*Photonics Centre, Tyndall National Institute, Prospect Row, Cork, Ireland*
[3]*Institute of Spectroscopy, Russian Academy of Sciences, 142190 Troitsk, Moscow Region, Russia*
[4]*Physics Department, University College Cork, Cork, Ireland*
(Received 20 March 2008; published 17 July 2008)

We propose and present a quantitative analysis of neutral atom microtraps based on optical near fields produced by the diffraction of a laser wave on small apertures in a thin screen. We show that near-field atom microtraps are capable of storing atoms in micron-sized regions, with estimated trap lifetimes of about 1 s, when using a moderate laser intensity of about 10 $\mathrm{W/cm^2}$. The depth of the proposed Fresnel atom microtraps is about 0.1 mK. An array of such atom microtraps could have applications to site-selective manipulation of cold atoms.

DOI: 10.1103/PhysRevA.78.013410 PACS number(s): 37.10.Gh, 42.50.−p, 42.25.Fx

I. INTRODUCTION

In recent years there has been a growing number of experimental and theoretical studies on the development of, and applications for, neutral atom traps [1–6]. A new and poorly studied approach to the development of miniature atom traps stems from the optical near fields formed by laser diffraction on small apertures in thin screens. Such an approach could lead to the fabrication of an array of atom microtraps and, accordingly, the production of a large number of trapped atomic microensembles from a single initial atomic cloud or beam. Earlier work [7] has shown that an array of atom dipole traps can be produced by focusing a laser beam on an array of spherical microlenses. The work presented here relies on a more recent proposal [8], whereby microlenses, formed in thin screens, can be used to focus atomic beams. We show that such a system can be modified to produce a microtrap array, using a moderate incident laser intensity of about 10 $\mathrm{W/cm^2}$.

Similar to other approaches employing laser fields, the operation of neutral-atom, near-field microtraps relies on dipole potentials and their corresponding dipole gradient forces. However, in other approaches the gradient force arises from the nonuniform field distribution over the laser beam cross section or over the wavelength of the laser light, whereas for near-field microtraps the gradient force stems from the optical field nonuniformity over the *aperture* diameter. Consequently, atom microtraps can store atomic microclouds with characteristic dimensions equivalent to or less than the field wavelength. Such microclouds could be used for site-selective manipulation of atoms in the field of quantum-information technologies [9–11].

In this paper, we propose and present a quantitative analysis of near-field Fresnel atom microtraps with a characteristic aperture size about or exceeding the optical wavelength. Such traps rely on the near-field diffraction pattern, characterized by a Fresnel number $N_F \geqslant 1$. We analyze the field distribution in the vicinity of a small, circular aperture in a thin screen and calculate the dipole potential of the atom in the diffracted near field. Our analysis of the Fresnel microtraps shows that, at a moderate intensity of the light field of about 10 $\mathrm{W/cm^2}$, the traps are able to store atoms with a kinetic energy of about 100 μK during time intervals of around 1 s.

II. TRAPPING POTENTIAL

An array of Fresnel atom microtraps is schematically shown in Fig. 1. The traps can be analyzed by considering the diffraction of a traveling light wave of arbitrary polarization on a circular aperture

$$\mathbf{E}_1 = \mathbf{e}E_0 \cos(kz - \omega t), \tag{1}$$

where $\mathbf{e}$ is a unit polarization vector, E_0 is the amplitude, and $k=\omega/c$ is the wave vector. When the size of the aperture exceeds or is equivalent to the wavelength of the optical field, the electric field behind the aperture can be represented in the scalar approximation as

$$\mathbf{E}_2 = \mathbf{e}E = \mathbf{e}\,\mathrm{Re}(\mathcal{E}e^{-i\omega t}), \tag{2}$$

where $\mathcal{E}=\mathcal{E}(\mathbf{r})$ is the complex field amplitude. The diffracted field can be evaluated by applying the Rayleigh-Sommerfeld diffraction formula [12,13]

$$\mathcal{E}(x,y,z) = \frac{E_0}{2\pi}\int\int \frac{\exp(ikr)}{r}\left(\frac{z}{r}\right)\left(\frac{1}{r} - ik\right)dx'dy', \tag{3}$$

where the distance between the point (x,y,z) in the observation plane and the point $(x',y',0)$ in the aperture plane is $r=[z^2+(x-x')^2+(y-y')^2]^{1/2}$, and the integral (3) is considered to be taken over the aperture region.

The evaluation of the Rayleigh-Sommerfeld integral can be simplified by taking into account the axial symmetry of the diffracted field. By introducing cylindrical coordinates ρ', ϕ' in the aperture plane and cylindrical coordinates ρ, ϕ in the observation plane one can rewrite the diffracted electric field as

*s.nicchormaic@ucc.ie

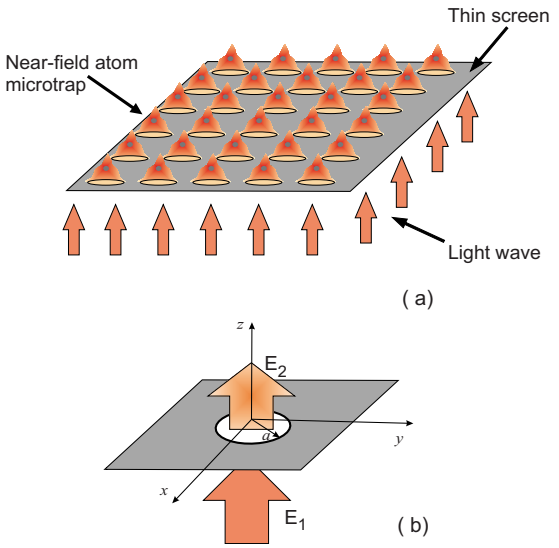

FIG. 1. (Color online) (a) An array of atom microtraps produced by diffracted optical near fields. (b) Schematic of a single microtrap formed by a circular aperture of radius a. E_1 represents the incoming light field and E_2 the diffracted near field.

$$\mathcal{E}(\rho,z) = \frac{E_0}{2\pi}\int_0^a \int_0^{2\pi} \frac{\exp(ikr)}{r}\left(\frac{z}{r}\right)\left(\frac{1}{r} - ik\right)d\varphi\rho' d\rho', \quad (4)$$

where now $r=[z^2+\rho^2+\rho'^2-2\rho\rho' \cos\varphi]^{1/2}$, $\varphi=\phi'-\phi$ is the relative angular coordinate, and a is the aperture radius.

For a red-detuned light field, the potential of a single microtrap is defined by the value of the light shift according to the usual equation [14]

$$U = -\hbar\frac{\Omega^2}{|\delta|}, \quad (5)$$

where $\Omega=dE/2\hbar$ is the Rabi frequency, d is the dipole matrix element, and $\delta=\omega-\omega_0$ is the detuning of the light field with respect to the atomic transition frequency ω_0. Accordingly, for the diffracted field represented by Eqs. (2)–(4), the potential of an atom in a single microtrap can be written as

$$U = -U_0\frac{|\mathcal{E}|^2}{E_0^2}, \quad (6)$$

where

$$U_0 = \frac{3}{8}\frac{\gamma}{|\delta|}\frac{E_0^2}{k^3} \quad (7)$$

is a characteristic value of the potential and γ is half the spontaneous decay rate. In what follows, we consider the case when the radius of the aperture, a, only slightly exceeds the optical wavelength λ. In this case the Fresnel number N_F is expected to be approximately equal to 1—i.e.,

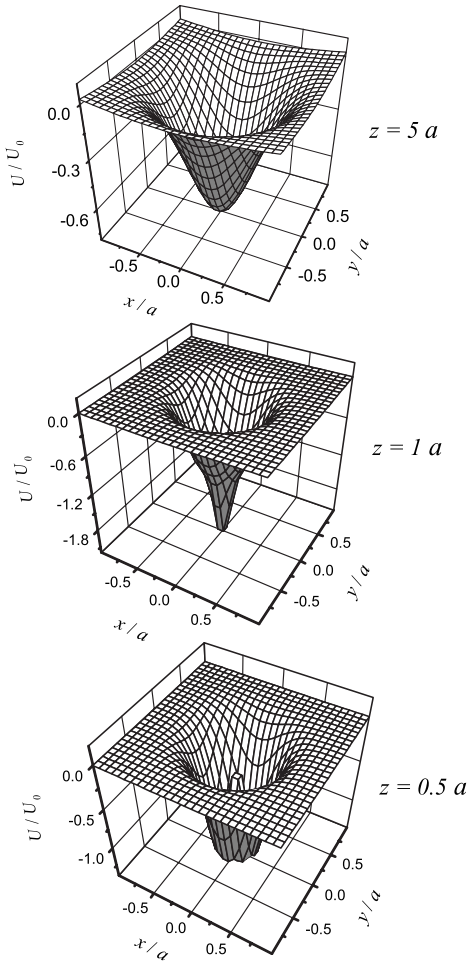

FIG. 2. Atom potential in a Fresnel atom microtrap as a function of transverse coordinates for radius $a=1.5\lambda$ ($ka=9.4$), at distances above the aperture $z=0.5a, 1a, 5a$.

$$N_F = \frac{a^2}{\lambda z_m} \approx 1, \quad (8)$$

where z_m is a characteristic vertical distance from the aperture to the maximum of the electric field intensity. Accordingly, the electric field intensity is expected to have a single diffraction maximum, and the atom potential will also have a single minimum. An example of the single-minimum atom potential is shown in Fig. 2 for different values of the vertical coordinate z.

Alongside the integral representation of the diffracted field and the corresponding potential of the atom, one can also find an analytical representation of the atom potential near the symmetry axis of the microtrap. This can be done by decomposing the integrand in Eq. (4) into a series in small radial displacements, $\rho \ll a$ [8,15]. Considering the second

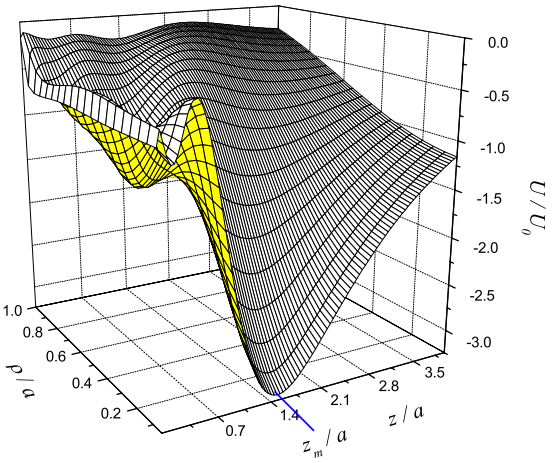

FIG. 3. (Color online) Atom potential of the Fresnel atom microtrap as a function of the coordinates z and ρ for $a=1.5\lambda$.

order in ρ, one can represent the near-axis atom potential as parabolic in the transverse direction,

$$U(\rho,z) = -U_0\left\{1+\frac{z^2}{R_a^2}-\frac{2z}{R_a}\cos k(R_a-z) - \frac{k^2a^2z\rho^2}{2R_a^3}\left[\left(1-\frac{3}{k^2R_a^2}\right)\left(\frac{z}{R_a}-\cos k(R_a-z)\right) + \frac{3}{kR_a}\sin k(R_a-z)\right]\right\}, \quad (9)$$

where $R_a=\sqrt{a^2+z^2}$. The potential represented in (9), when considered as a function of the vertical coordinate z, has a minimum at $z=z_m$, defined by the transcendental equation

$$\cos[k(R_a-z)-\chi] = \frac{a^2z}{(a^2+z^2)^{3/2}}\frac{1}{(A^2+B^2)^{1/2}}, \quad (10)$$

where $\tan\chi=B/A$, with $A=a^2/(a^2+z^2)$ and $B=kz(1-z/R_a)$.

The dependence of the potential $U=U(\rho,z)$ on the coordinates z and ρ is shown in Fig. 3 for the same aperture size as used in Fig. 2. The near-axis potential represented by Fig. 3 has a minimum at $z_m=1.47a=2.2\lambda$. In accordance with our expectations, the Fresnel number $N_F\simeq 1$ at this value of z_m and the atom potential has a well-defined minimum near the z axis.

III. PARAMETERS OF NEAR-FIELD MICROTRAPS

We evaluate parameters of the Fresnel atom microtraps for (i) ^{85}Rb atoms, which interact with a far-red-detuned light field at the dipole transition $5\,^2S_{1/2}(F=3)\rightarrow 5\,^2P_{3/2}(F=4)$ with wavelength $\lambda=780$ nm, and (ii) ^{133}Cs atoms interacting with the light field at dipole transition $6\,^2S_{1/2}(F=4)\rightarrow 6\,^2P_{3/2}(F=5)$ with wavelength $\lambda=852$ nm. For the dipole transition in ^{85}Rb, the natural linewidth is $2\gamma=2\pi\times 5.98$ MHz and the saturation intensity is $I_S=1.6$ mW/cm^2. For ^{133}Cs the corresponding values are $2\gamma=2\pi\times 5.18$ MHz and $I_S=1.1$ mW/cm^2 [14].

TABLE I. Parameters of a near-field Fresnel diffraction trap for ^{85}Rb and ^{133}Cs atoms with an input laser power of 10 W/cm^2 and detuning $\delta=-10^4\gamma$ for an aperture radius $a=1.5\lambda$.

Atom	U_d (mK)	ν_ρ (kHz)	ν_z (kHz)	$\bar{\rho}$ (nm)	$\bar{z}$ (nm)	τ (s)
^{85}Rb	0.13	34	19	60	80	0.6
^{133}Cs	0.17	29	14	51	73	1

We choose the radius of the microtraps to be $a=1.5\lambda$, with $a=1.2$ μm for ^{85}Rb atoms and $a=1.3$ μm for ^{133}Cs atoms. For these two cases the minimum of the trap potential is located at distances above the aperture, $z_m=1.76$ μm and 1.91 μm, respectively. Choosing a laser intensity $I=10$ W/cm^2 and a large negative detuning $\delta=-10^4\gamma$, we can evaluate the depth of the potential U_d as 0.13 mK for Rb and 0.17 mK for Cs, respectively. The energy levels near the bottom of the trapping potential,

$$E = h\nu_\rho\left(n_\rho+\frac{1}{2}\right)+h\nu_z\left(n_z+\frac{1}{2}\right), \quad (11)$$

can be evaluated by representing the potential (9) near the minimum as a harmonic potential,

$$U(\rho,z) = \frac{1}{2}M\omega_\rho^2\rho^2+\frac{1}{2}M\omega_z^2(z-z_m)^2, \quad (12)$$

where M is the atom mass. This procedure shows that at chosen parameters of the microtraps, typical oscillation frequencies are of the order of 10 kHz. Specific values of the transverse frequencies, $\nu_\rho=\omega_\rho/2\pi$, and longitudinal frequencies, $\nu_z=\omega_z/2\pi$, for ^{85}Rb and ^{133}Cs atoms are shown in Table I, together with values of the characteristic oscillation amplitudes in the ground state, $\bar{\rho}=\sqrt{\hbar/M\omega_\rho}$ and $\bar{z}=\sqrt{\hbar/M\omega_z}$. Note that the number of quantized energy levels in the microtrap potential is estimated to be about 50, with a typical energy separation of about $\Delta E=1$ μK.

It is worth noting that the optical potential of a Fresnel atom microtrap could generally be distorted by the Casimir-Polder potential due to the presence of the screen [16]. Since the considered optical potential is localized at distances z from the screen, where $z>\lambda/2\pi$, the contribution of the Casimir-Polder potential for the case of a perfect metal screen and in the absence of any opening can be evaluated as [16–18]

$$U_{\mathrm{CP}}(z) = -\frac{3\hbar\gamma}{8\pi}\left(\frac{\lambda}{2\pi z}\right)^4. \quad (13)$$

We estimate the value of the potential $U_{\mathrm{CP}}(z)$ at two important points: (i) at the position of the potential well minimum, $z_m=2.2\lambda$, and (ii) at the position of a local maximum of the optical potential, $z_M=0.7\lambda$. Near the bottom of the optical potential the Casimir-Polder potential is about 4×10^{-4} μK for both ^{85}Rb and ^{133}Cs atoms. At the position of the local maximum the Casimir-Polder potential is about 5×10^{-2} μK. Since the depth of the optical potential well is estimated to be about 100 μK, the above estimates show that

for the Fresnel atom microtraps considered here the Casimir-Polder potential can be neglected.

Similar to conventional far-off-resonance dipole traps, atoms can be lost from the Fresnel atom microtrap due to diffusive heating of the atoms and collisions with the background gas [19]. Assuming the rest gas pressure is chosen to be sufficiently low, we can evaluate the lifetime of the atoms in the Fresnel atom microtrap by considering the diffusion broadening of atomic velocities due to photon recoil fluctuations. For this process, the velocity diffusion coefficient has a standard evaluation as $D=\gamma v_r^2(I/I_S)(\gamma/\delta)^2$, where $v_r=\hbar k/M$ is the recoil velocity, I is the light field intensity, and I_S is the saturation intensity [19]. Assuming that the kinetic energy of an atom escaping from the trap is approximately equal to the potential well depth, $Mv^2/2=U_d$, and the atomic velocity is defined by the diffusion broadening, $v^2\approx D\tau$, we can evaluate the trap lifetime τ as

$$\tau=\gamma^{-1}\frac{2U_d}{Mv_r^2}\left(\frac{I_S}{I}\right)\left(\frac{\delta}{\gamma}\right)^2. \tag{14}$$

For the above chosen parameters, a trap lifetime of about 1 s can be achieved, as given in Table I. The lifetime can be increased by increasing the input laser power, which, in turn, increases the trap depth.

IV. CONCLUSION

We have proposed a system of neutral atom microtraps based on a series of circular apertures in a thin screen. Laser light incident on the screen produces an array of potential minima for atoms in the near field. Our analysis shows that these near-field atom microtraps can store cold atoms for times up to seconds. The potential well depth of the microtraps is mainly determined by the intensity of the incident laser field and the detuning. By varying these two parameters one can achieve robust control over the trap parameters. A numerical analysis for ^{85}Rb and ^{133}Cs atoms shows that a trap depth of 0.1 mK can be achieved, with storage times up to a second at an incident laser intensity of 10 W/cm^2. With such trap lifetimes one can perform atom optics experiments by blending microfabrication technology with cold atoms [7]. An important point to note is that each individual microtrap uses only about 0.5 μW in the above considered case, where the aperture radius $a=1.5\lambda$.

We also note that, in the present consideration, we have limited our analysis to the case of apertures that are well separated in the screen. For a periodic array of densely spaced microtraps, one may expect even further reduction to the required incoming laser power due to an enhancement of the diffracted field during light transmission through the microaperture array [20,21].

Finally, we note that the above-considered microtraps possess the same basic properties as for far-off-resonance dipole traps. Hence, the proposed traps are free of some perturbations that are significant in other types of atom traps. In particular, such processes as spin flips near surfaces [22], which redistribute trapped atoms over magnetic sublevels, cannot influence the lifetime of atoms in the proposed Fresnel atom microtraps. Another advantage of near-field microtraps is that they are capable of storing atoms at relatively large distances from the material screen which produces the diffracted light field. Accordingly, the internal and translational states of the atoms stored in the near-field microtraps are primarily defined by the dipole interaction with a far-detuned light field only. In particular, we have shown by numerical evaluation that the influence of the Casimir-Polder potential on the atomic states in a Fresnel atom microtrap can be neglected. The van der Waals energy shifts [23] can also be shown to have a small influence on the atomic states trapped in a Fresnel atom microtrap. It can also be noted that the presence of the opening in the screen can be considered as an advantage for loading the atoms into near-field microtraps, as such microtraps ease the application of standard loading techniques widely used for other types of dipole traps [14,19]. An alternative loading scheme using optical tweezers may be feasible [24], due to the dimensions being considered within the proposed trap geometry.

ACKNOWLEDGMENTS

This work was funded by Science Foundation Ireland under Grant Nos. 02/IN1/128 and No. 06/W.1/I866. Part of the work was supported by the Russian Foundation for Basic Research (Project No. 07-02-00748).

[1] V. I. Balykin, V. S. Letokhov, and V. G. Minogin, Phys. Scr. **22**, 119 (1988).
[2] V. I. Balykin and V. S. Letokhov, Sov. Phys. JETP **67**, 78 (1988).
[3] W. Hänsel, P. Hommelhoff, T. W. Hänsch, and J. Reichel, Nature (London) **413**, 498 (2001).
[4] K. D. Nelson, Xiao Li, and D. S. Weiss, New J. Phys. **3**, 556 (2007).
[5] S. K. Sekatskii, B. Riedo, and G. Dietler, Opt. Commun. **195**, 197 (2001).
[6] J. L. Cohen, B. Dubetsky, and P. R. Berman, Phys. Rev. A **60**, 4886 (1999).
[7] G. Birkl, F. B. J. Buchkremer, R. Dumke, and W. Ertmer, Opt. Commun. **191**, 67 (2001).
[8] V. I. Balykin and V. G. Minogin, Phys. Rev. A **77**, 013601 (2008).
[9] M. A. Nielsen and I. L. Chuang, *Quantum Computation and Quantum Information* (Cambridge University Press, Cambridge, England, 2000).
[10] J. I. Cirac and P. Zoller, Phys. Rev. Lett. **74**, 4091 (1995).
[11] F. Schmidt-Kaler, H. Häffner, M. Riebe, S. Gulde, G. P. T. Lancaster, T. Deuschle, C. Becher, C. F. Roos, J. Eschner, and R. Blatt, Nature (London) **422**, 408 (2003).
[12] J. A. Stratton, *Electromagnetic Theory* (McGraw-Hill, New

York, 1941).
[13] R. L. Lucke, Eur. J. Phys. **27**, 193 (2006).
[14] H. J. Metcalf and P. van der Straten, *Laser Cooling and Trapping* (Springer-Verlag, Berlin, 1999).
[15] V. I. Balykin and V. G. Minogin, JETP **105**, 479 (2007).
[16] H. B. G. Casimir and D. Polder, Phys. Rev. **73**, 360 (1948).
[17] D. Meschede, W. Jhe, and E. A. Hinds, Phys. Rev. A **41**, 1587 (1990).
[18] E. A. Hinds and V. Sandoghdar, Phys. Rev. A **43**, 398 (1991).
[19] V. I. Balykin, V. G. Minogin, and V. S. Letokhov, Rep. Prog. Phys. **63**, 1429 (2000).
[20] F. J. García de Abajo, R. Gómez-Medina, and J. J. Sáenz, Phys. Rev. E **72**, 016608 (2005).
[21] R. Gordon, Phys. Rev. A **76**, 053806 (2007).
[22] M. P. A. Jones, C. J. Vale, D. Sahagun, B. V. Hall, and E. A. Hinds, Phys. Rev. Lett. **91**, 080401 (2003).
[23] W. R. Johnson, V. A. Dzuba, U. I. Safronova, and M. S. Safronova, Phys. Rev. A **69**, 022508 (2004).
[24] J. Fortàgh and C. Zimmermann, Rev. Mod. Phys. **79**, 235 (2007).